GREEN HYDROGEN PRODUCTION BY PHOTOCATALYSIS

TANONGSAK SUKKASEM

A Thesis Submitted in Partial Fulfillment of the Requirements for the
Degree of Doctor of Philosophy in Mechanical and Process System Engineering
Suranaree University of Technology
Academic Year 2025

การผลิตไฮโดรเจนสีเขียวด้วยโฟโตคะตะไลซิส

นายทนงศักดิ์ สุขเกษม

วิทยานิพนธ์นี้เป็นส่วนหนึ่งของการศึกษาตามหลักสูตรปริญญาปรัชญาดุษฎีบัณฑิต
สาขาวิชาวิศวกรรมเครื่องกลและระบบกระบวนการ
มหาวิทยาลัยเทคโนโลยีสุรนารี
ปีการศึกษา 2568

GREEN HYDROGEN PRODUCTION BY PHOTOCATALYSIS

Suranaree University of Technology has approved this thesis submitted in partial fulfillment of the requirements for the Degree of Doctor of Philosophy.

Thesis Examining Committee

(Assoc. Prof. Dr. Supareak Praserthdam)
Chairperson

(Dr. Supunnee Junpirom)
Member (Thesis Advisor)

(Prof. Dr. Kritsana Sagarik)
Member (Thesis Co-Advisor)

(Assoc. Prof. Dr. Theeranun Siritanon)
Member (Thesis Co-Advisor)

(Assoc. Prof. Dr. Napat Triroj)
Member

(Assoc. Prof. Dr. Lek Wantha)
Member

(Assist. Prof. Dr. Keerati Suluksna)
Member

(Assoc. Prof. Dr. Yupaporn Ruksakulpiwat)
Acting Vice Rector for Academic Affairs
and Quality Assurance

(Assoc. Prof. Dr. Pornsiri Jongkol)
Dean of Institute of Engineering

ทนงศักดิ์ สุขเกษม : การผลิตไฮโดรเจนสีเขียวด้วยโฟโตคะตะไลซิส (GREEN HYDROGEN PRODUCTION BY PHOTOCATALYSIS)
อาจารย์ที่ปรึกษา : อ.ดร.สุพรรณี จันทร์ภิรมณ์, 111 หน้า

คำสำคัญ : การผลิตไฮโดรเจนสีเขียว; กลไกการแยกน้ำ; การเร่งปฏิกิริยาเชิงแสง; เครื่องปฏิกรณ์แบบแผง; การวิเคราะห์เชิงเทคนิค-เศรษฐศาสตร์; $(TiO_2)_2(H_2O)_2$; แบบจำลองคลัสเตอร์; DFT และ TD-DFT

ปัจจุบัน การแยกน้ำด้วยตัวเร่งปฏิกิริยาเชิงแสง (photocatalytic water splitting) ได้รับความสนใจอย่างกว้างขวางในฐานะวิธีการผลิตไฮโดรเจน (H_2) อย่างยั่งยืน อย่างไรก็ตาม งานวิจัยส่วนใหญ่ยังคงจำกัดการทดสอบภายใต้เครื่องปฏิกรณ์เชิงแสงแบบกะ (batch photoreactor) ซึ่งไม่สอดคล้องกับแนวทางการประยุกต์ใช้ในระดับอุตสาหกรรมที่มุ่งเน้นกระบวนการแบบต่อเนื่อง ดังนั้น วิทยานิพนธ์ฉบับนี้ จึงมุ่งออกแบบและพัฒนากระบวนการแยกน้ำด้วยตัวเร่งปฏิกิริยาเชิงแสงแบบต่อเนื่องในระดับห้องปฏิบัติการ โดยบูรณาการองค์ความรู้ด้านการออกแบบกระบวนการเชิงวิศวกรรมกระบวนการ การทดลอง การคำนวณเชิงทฤษฎี ตลอดจนการวิเคราะห์เชิงเทคนิค-เศรษฐศาสตร์และสิ่งแวดล้อม

การออกแบบกระบวนการระดับห้องปฏิบัติการมุ่งเน้นการสร้างเครื่องปฏิกรณ์เชิงแสงแบบแผงต่อเนื่อง (panel photoreactor) ร่วมกับการออกแบบหน่วยประกอบอื่น ได้แก่ หน่วยทำบริสุทธิ์ก๊าซ H_2 และระบบควบคุมอัตโนมัติ โดยคำนึงถึงมาตรฐานความปลอดภัย เนื่องจากการทดสอบหน่วยทำบริสุทธิ์ H_2 หากมีความเข้มข้นสูงอาจมีความเสี่ยง วิทยานิพนธ์ฉบับนี้จึงจำกัดขอบเขตการทดลองไว้ที่การทดสอบต้นแบบโดยไม่ป้อนก๊าซ H_2 (ทดสอบเฉพาะระบบ) สำหรับเครื่องปฏิกรณ์เชิงแสงแบบแผงต่อเนื่องถูกทดสอบการทำงานเชิงปฏิบัติจริงร่วมกับตัวเร่งปฏิกิริยา TiO_2 และ 2%Pt/TiO_2 ภายใต้แหล่งกำเนิดแสง UVA-LED LED และแสงแดดธรรมชาติ ทั้งในสภาวะที่มีและไม่มีสารเอื้อต่อปฏิกิริยา (เมทานอล) ผลการทดสอบพบว่า ภายใต้สภาวะที่ไม่มีเมทานอล อัตราการผลิต H_2 เท่ากับ 0.51 μmol g^{-1} min^{-1} (TiO_2 ภายใต้แสง UVA-LED ที่ 25 °C) ขณะที่ภายใต้สภาวะที่มีเมทานอล 10% v/v (2%Pt/TiO_2) พบอัตราการผลิตสูงสุดที่ 486.94 358.25 และ 333.82 μmol g^{-1} min^{-1} สำหรับแสง UVA-LED LED และแสงแดดธรรมชาติ ตามลำดับ เมื่อเปรียบเทียบกับเครื่องปฏิกรณ์เชิงแสงแบบกะ พบว่าเครื่องปฏิกรณ์เชิงแสงแบบแผงต่อเนื่องให้ประสิทธิภาพเหนือกว่า เนื่องจากเอื้อต่อการถ่ายเทมวลผลิตภัณฑ์ออกจากระบบ ลดการเกิดปฏิกิริยาย้อนกลับ และสะท้อนศักยภาพของกระบวนการในระดับอุตสาหกรรมในอนาคต

ในส่วนการคำนวณเชิงทฤษฎี ได้ประยุกต์ใช้เคมีควอนตัมเพื่ออธิบายกลไกการแยกน้ำทั้งในเส้นทาง 2 และ 4 อิเล็กตรอน โดยศึกษาครอบคลุมตั้งแต่เส้นทางปฏิกิริยา สมบัติเชิงอุณหพลศาสตร์

และจลนพลศาสตร์ โดยให้ความสำคัญกับอิทธิพลของการแปลงพลังงานแสงเป็นความร้อน และความยาวคลื่นของรังสีที่ฉาย ตัวแบบคลัสเตอร์ $[(TiO_2)_2(H_2O)_2]$ ถูกใช้ในการศึกษาการกระตุ้นด้วยแสงและการผ่อนคลายพลังงานแบบไม่แผ่รังสี นำไปสู่การแตกพันธะและการไอโซเมอไรเซชัน การคำนวณ DFT/B3LYP/TZVP สำหรับสถานะพื้น (S_0) และ TD-DFT/B3LYP/TZVP สำหรับสถานะกระตุ้น (S_1) ถูกนำมาใช้ในการสร้างพื้นผิวพลังงานศักย์ (PESs) ขณะที่ทฤษฎีสถานะทรานซิชัน (TST) ถูกประยุกต์เพื่อคำนวณสมบัติเชิงอุณหพลศาสตร์และจลนพลศาสตร์ของปฏิกิริยา ผลการคำนวณบ่งชี้ว่าการแตกตัวของโมเลกุล $2H_2O$ บนคลัสเตอร์ $(TiO_2)_2$ สามารถเกิดขึ้นด้วยพลังงานก่อกัมมันต์ต่ำหรือแทบไม่มีอุปสรรค ส่งผลให้เกิดผลิตภัณฑ์เส้นทาง 2 อิเล็กตรอน ได้แก่ H_2O_2 และ H_2 สำหรับเส้นทาง 4 อิเล็กตรอน ได้แก่ O_2 และ $2H_2$ ที่น่าสนใจคือ การกระตุ้นด้วยรังสีใกล้อินฟราเรดสามารถเหนี่ยวนำการเกิด H_2 โมเลกุลที่สองบน PES ของ S_1 โดยแทบไม่ต้องเอาชนะอุปสรรคพลังงาน ในขณะที่บน S_0 PES ยังคงมีอุปสรรคปานกลาง การวิเคราะห์เชิงอุณหพลศาสตร์แสดงให้เห็นว่าการถ่ายโอนพลังงานจากกระบวนการดีออกซิเจเนชันไปยังกระบวนการดีไฮโดรจีเนชัน สามารถขับเคลื่อนเส้นทางการผลิต H_2 ที่มีความเป็นไปได้สูงที่อุณหภูมิต่ำ ส่วนการวิเคราะห์เชิงจลนพลศาสตร์ชี้ให้เห็นขั้นตอนกำหนดอัตรา (rate-limiting step) ของกลไก

ท้ายที่สุด การวิเคราะห์เชิงเทคนิค-เศรษฐศาสตร์ และสิ่งแวดล้อม ให้ข้อมูลว่าต้นทุนการผลิต H_2 อยู่ที่ประมาณ 46 USD/kg H_2 พร้อมพลังงานสะสมต่อหน่วย 364 MJ/kg H_2 และการปล่อยก๊าซเรือนกระจก 5 kg CO_{2eq}/kg H_2 ภายใต้เงื่อนไขที่เหมาะสม (แหล่งกำเนิดแสง LED และตัวเร่งปฏิกิริยา 2%Pt/TiO_2) ซึ่งถือว่าค่าต้นทุนยังสูงเนื่องจากค่าไฟฟ้าและตัวเร่งปฏิกิริยาแพลทินัม (Pt) หากสามารถใช้พลังงานไฟฟ้าจากโซลาร์เซลล์ร่วมด้วยและพัฒนาตัวเร่งปฏิกิริยาทางเลือกที่มีต้นทุนต่ำลงได้จะสามารถเพิ่มความเป็นไปได้และศักยภาพการแข่งขันของกระบวนการในเชิงพาณิชย์ โดยภาพรวมด้านพลังงานและสิ่งแวดล้อมนั้นถือว่ามีศักยภาพสูงในการนำไปใช้จริง

สาขาวิชา วิศวกรรมเคมี
ปีการศึกษา 2568

ลายมือชื่อนักศึกษา .....
ลายมือชื่ออาจารย์ที่ปรึกษา .....
ลายมือชื่ออาจารย์ที่ปรึกษาร่วม .....
ลายมือชื่ออาจารย์ที่ปรึกษาร่วม .....

TANONGSAK SUKKASEM : GREEN HYDROGEN PRODUCTION BY PHOTOCATALYSIS.
THESIS ADVISOR : SUPUNNEE JUNPIROM, Ph.D., 111 PP.

Keywords : Green hydrogen production; water splitting mechanism; photocatalysis; panel photoreactor; techno-economic analysis; $(TiO_2)_2(H_2O)_2$; cluster model; DFT and TD-DFT

At present, photocatalytic water splitting has attracted widespread attention as a sustainable pathway for hydrogen (H_2) production. However, most studies remain limited to batch photoreactor systems, which are inconsistent with the industrial trend toward continuous processes. Therefore, this dissertation aims to design and develop a continuous photocatalytic water splitting process at the laboratory scale by integrating knowledge of process engineering design, experimental investigation, theoretical calculations, as well as techno-economic and environmental analysis.

The laboratory-scale process design focused on the development of a continuous panel photoreactor, together with auxiliary units such as an H_2 purification unit and an automated control system, while considering safety standards. Since testing the purification unit with high H_2 concentrations involves safety risks, this dissertation restricted the scope to prototype testing without the direct feed of concentrated H_2 (system-only operation). The panel photoreactor prototype was experimentally tested using TiO_2 and 2%Pt/TiO_2 photocatalysts under UVA-LED, LED, and natural sunlight irradiation, with and without methanol as a sacrificial agent. The results revealed that, under methanol-free conditions, the H_2 production rate was 0.51 μmol g^{-1} min^{-1} (TiO_2, UVA-LED, 25 °C). In contrast, with 10% v/v methanol (2%Pt/TiO_2), the maximum H_2 production rates were 486.94, 358.25, and 333.82 μmol g^{-1} min^{-1} under UVA-LED, LED, and natural sunlight, respectively. Compared to the conventional batch photoreactor, the continuous panel photoreactor demonstrated superior performance, as it facilitated efficient mass transfer of products, suppressed recombination, and highlighted the potential for industrial-scale applications in the future.

The theoretical study employed quantum chemical calculations to elucidate the reaction mechanisms of photocatalytic water splitting along both two-electron and four-electron pathways, covering reaction pathways, thermodynamic properties, and kinetics. Special attention was given to photo-to-thermal energy conversion and the influence of irradiation wavelength. A cluster model, $[(TiO_2)_2(H_2O)_2]$, was adopted to

investigate photoexcitation and non-radiative relaxation processes, leading to bond cleavage and isomerization. DFT/B3LYP/TZVP was applied for the ground state (S_0) and TD-DFT/B3LYP/TZVP for the excited state (S_1) to construct potential energy surfaces (PESs). Transition State Theory (TST) was further employed to evaluate thermodynamic and kinetic parameters. The results indicated that dissociation of $2H_2O$ on the $(TiO_2)_2$ cluster can proceed with low or negligible energy barriers, yielding two-electron products (H_2O_2 and H_2) and four-electron products (O_2 and $2H_2$). Remarkably, near-infrared excitation enabled the formation of a second H_2 molecule on the S_1 PES with almost no barrier, whereas the S_0 PES exhibited moderate barriers. Thermodynamic analysis showed that energy transfer from deoxygenation to dehydrogenation processes can drive a feasible low-temperature H_2 production pathway, while kinetic analysis identified the rate-limiting step of the mechanism.

Finally, techno-economic and environmental assessments revealed an estimated H_2 production cost of ~46 USD/kg H_2, with a cumulative energy demand of 364 MJ/kg H_2 and greenhouse gas emissions of 5 kg CO_{2eq}/kg H_2 under optimized operating conditions (LED irradiation and 2%Pt/TiO_2 catalyst). Although the production cost remains high, primarily due to electricity consumption and platinum catalyst expenses, the integration of solar-derived electricity and low-cost alternative catalysts could significantly enhance the feasibility and competitiveness of the process. Overall, the proposed system demonstrates promising energy and environmental performance, indicating strong potential for future practical applications.

School of Chemical Engineering
Academic Year 2025

Student's Signature Tanongsak Sukkasem
Advisor's Signature SUPUNNEE J.
Co-Advisor's Signature K. Sapaw
Co-Advisor's Signature Theeranun Siritanon

ACKNOWLEDGMENT

This dissertation could not have been completed without the kind support and guidance of many individuals to whom I am deeply grateful.

I would like to express my sincere gratitude to **Dr. Supunnee Junpirom**, my thesis advisor, for her continuous guidance, insightful advice, generous support, and kind encouragement throughout every stage of this research. Her constructive comments and suggestions greatly contributed to the quality and completeness of this dissertation.

I am deeply thankful to **Prof. Dr. Kritsana Sagarik**, my co-advisor, for his valuable guidance on quantum chemical calculations throughout my doctoral studies. I also wish to thank **Dr. Pannipa Panajapo** for her assistance and technical advice regarding computational methods.

My sincere appreciation is extended to **Assoc. Prof. Dr. Theeranun Siritanon**, my co-advisor, for her valuable suggestions on photocatalyst material preparation and for providing laboratory facilities and equipment for reaction testing using a batch photoreactor. I also gratefully acknowledge **Ms. Jeeranan Prachanat** for her technical assistance in the synthesis of photocatalyst materials.

I am also thankful to the thesis examination committee: **Assoc. Prof. Dr. Supareak Praserthdam**, **Assoc. Prof. Dr. Lek Wantha**, Assoc. Prof. **Dr. Napat Triroj**, and **Assist. Prof. Dr. Keerati Suluksna** for their time, valuable feedback, and constructive recommendations which helped improve the final version of this dissertation.

This work utilized high-performance computing facilities provided by the National e-Science Infrastructure Consortium (NECTEC), and the National Science and Technology Development Agency (NSTDA). The research was financially supported by (i) Suranaree University of Technology (SUT), (ii) Thailand Science Research and Innovation (TSRI), and (iii) National Science, Research and Innovation Fund (NSRF) [Grant No. 204235]. Additional computing resources were provided by the NSTDA

Supercomputer Center (ThaiSC). Funding was also received through the Program Management Unit for Human Resources & Institutional Development, Research and Innovation (PMU-B) under Grant No. B42G670035.

Special thanks go to **Mr. Kantinan Chunhapanyawech**, **Mr. Keerati Ninnanon**, **Mr. Akkarawin Rattanatagoondacha**, **Ms. Yanisa Pandam**, and **Ms. Suttisa Muntham** students and collaborators who participated in experimental studies on the photocatalytic water splitting system for H_2 production. I am also grateful to all individuals who have contributed to this research but are not mentioned here by name.

Tanongsak Sukkasem

TABLE OF CONTENTS

Page

TABLE OF CONTENTS (Continued)

Page

TABLE OF CONTENTS (Continued)

Page

LIST OF TABLES

Table **Page**

LIST OF FIGURES

Figure **Page**

LIST OF FIGURES (Continued)

Figure **Page**

LIST OF FIGURES (Continued)

Figure **Page**

LIST OF FIGURES (Continued)

Figure **Page**

LIST OF FIGURES (Continued)

Figure **Page**

CHAPTER I

INTRODUCTION

1.1 Introduction

Global energy demand is expected to more than double by 2050, requiring both a secure supply and reduced greenhouse gas (GHG) emissions (Ahmed et al., 2022; Aydin et al., 2022). Fossil fuels, supplying 80% of energy, contribute over 65% of GHG emissions and cause severe environmental threats (Chung et al., 2023). Meeting rising energy needs without harming the environment is a major challenge. Researchers are thus exploring clean energy sources, with solar energy and hydrogen (H_2) standing out (Liu et al., 2021). While solar energy is abundant, its intermittency demands efficient storage. Water splitting using sunlight to produce H_2 offers a promising solution (Han et al., 2016; Egeland-Eriksen et al., 2021).

For H_2 production to be sustainable, it must be clean, affordable, and reliable. Electrochemical water splitting offers a cleaner method for producing H_2, but it remains costly, with prices ranging from 5.78 to 7.00 USD/kg H_2, primarily due to high energy demands (Thibault et al., 2020; Ahmed et al., 2022). The use of rare metals like Pt, Au, Ru, and Ag as electrocatalysts further drives up costs and introduces price instability due to market factors (Vochozka et al., 2021; Rowland et al., 2021; Nováková et al., 2022; Bartoš et al., 2022). Additionally, the cost of H_2 production through electrolysis depends on the energy source, such as renewable power (solar: 5.78-23.27 USD/kg H_2; wind: 5.89-6.03 USD/kg H_2) (Ball et al., 2015). Nowadays, researchers are also exploring alternative green H_2 production methods through thermolysis, photocatalysis, thermochemical processes, and biomass conversion (Ahmed et al., 2022).

Photocatalysis is a promising method for eco-friendly H_2 generation, but challenges remain, including limited efficiency, stability, complexity (Meng et al., 2019). The reverse reaction between H_2 and O_2 reduces efficiency and requires expensive gas separation (Cai et al., 2017; Chen et al., 2019). Photocatalytic partial water splitting, using sacrificial agents to stabilize photo-generated charges, addresses some issues

(Wang et al., 2017). Since 1997, research on photocatalytic seawater splitting has grown, but its high salinity can deactivate photocatalysts and cause undesirable reactions, reducing efficiency and lifespan compared to pure water (Ji et al., 2007; Li et al., 2019). Water splitting for H_2 production by photocatalysis can occur via two pathways: the two-electron pathway (i.e., $2H_2O \rightarrow H_2O_2 + H_2$) (Xue et al., 2019; Malik et al., 2020) or the four-electron pathway (i.e., $2H_2O \rightarrow O_2 + 2H_2$) (Liao et al., 2014; Malik et al., 2020; Nishiyama et al., 2021; Zhou et al., 2023). Splitting water into H_2 and O_2 is an endothermic reaction with an enthalpy of 484 kJ/mol, whereas splitting water into H_2O_2 and H_2 has an enthalpy of 384.1 kJ/mol, based on the heat of formation of H_2O at 298 K (−241.8 ± 0.8 kJ/mol) (Chase et al., 1998).

In photocatalytic water splitting, the semiconductor plays an important role such as titanium dioxide (TiO_2). TiO_2 serves two main purposes: enhancing living environments through anti-stain, self-cleaning, and superhydrophilic properties, and light energy conversion, such as water splitting (Nishiyama et al., 2021). TiO_2 photocatalysts have widespread industrial applications, although previous setups like Pt/Degussa P25 and Pt/C_3N_4 achieved low efficiencies in H_2 and H_2O_2 production (Daskalaki et al., 2011; Liu et al., 2012). Nanoparticles of anatase, rutile, and brookite have been shown to oxidize water to H_2O_2 (Cao et al., 2020; Sukkasem et al., 2022, 2023). While solar H_2 production methods can reach 30% efficiency with solar cells (Jia et al., 2016), photocatalytic water splitting typically achieves 1-9% efficiency but remains simpler, cost-effective, and scalable (Hisatomi et al., 2019; Kim et al., 2019; Nishiyama et al., 2021; Zhou et al., 2023). Current systems, including a 100 m^2 photocatalysis setup, have proven to be safe and effective for H_2 production (Nishiyama et al., 2021).

Developing an efficient photocatalytic system for pure water splitting into H_2 requires a multifaceted approach. Key photocatalysts like $SrTiO_3$:Al with Rh/CrO_x and CoO_y (efficiency: 0.40%-0.76% STH) (Goto et al., 2018; Nishiyama et al., 2021), InGaN/GaN nanowires with Rh/Cr_2O_3, Co_3O_4 (6.20-9.00% STH) (Zhou et al., 2023), and CdS@SiO_2-Pt (0.68% STH) (Li et al., 2024) have shown promise, but optimizing operating conditions is also essential. These include the light source (Goto et al., 2018; Nishiyama et al., 2021; Zhou et al., 2023; Li et al., 2024), light incident angles (10°-30°) for

photoreactors (Goto et al., 2018; Nishiyama et al., 2021), reaction temperature (30-80 °C) (Zhou et al., 2023), pH levels (Zhou et al., 2023), and photocatalyst quantity (Goto et al., 2018; Nishiyama et al., 2021; Zhou et al., 2023; Li et al., 2024). Additionally, photoreactor design is crucial for enhancing efficiency. By addressing these factors, researchers can improve photocatalytic systems for sustainable H_2 production. Various photoreactors, such as stirred tanks and panel systems using sunlight, are employed for H_2 production, with panel reactors showing good scalability (Nishiyama et al., 2021; Zhou et al., 2023). However, changes in sunlight throughout the day can affect performance, reaction uniformity, and energy efficiency key factors for scaling up to industrial applications.

After producing H_2, purification is critical to meet the stringent ISO14687 standards necessary for fuel cell applications. These standards require different purity levels depending on the use: 98% for internal combustion engines (ISO14687-1), 99.9% for stationary proton-exchange membrane fuel cells (PEMFCs) (ISO14687-3), and 99.97% for PEMFC road vehicles (ISO14687-2). Pressure swing adsorption (PSA) is one of the most widely used technologies for H_2 purification, offering purities from 98% to over 99.99% with relatively low energy consumption and capital costs (Delgado et al., 2006; Sircar et al., 2009; Yáñez et al., 2020). PSA systems operate by cyclic adsorption and regeneration processes within columns filled with selective adsorbents, achieving H_2 recovery rates of 70-90% in large-scale operations. In this study, we present a lab-scale system for green H_2 production via photocatalytic water splitting, focusing on H_2 production methods, as well as the fundamental theoretical study of photocatalytic water splitting through computational calculations.

1.2 Research objectives

1.2.1 To develop a lab-scale for green H_2 production via photocatalysis as a guideline for large-scale production.

1.2.2 To develop a method for preparing photocatalyst materials suitable for mass production.

1.2.3 To investigate the operating conditions for H_2 production via the photocatalytic water splitting process.

1.2.4 To investigate photocatalytic water splitting using quantum chemical calculations.

1.2.5 To evaluate the techno-economic and environmental assessment of pilot-scale photocatalytic water splitting.

1.3 Scope and limitations of the research

1.3.1 The lab-scale process design focused on the development of a continuous panel photoreactor, together with auxiliary units such as an H_2 purification unit and an automated control system, while considering safety standards. Since testing the purification unit with high H_2 concentrations involves safety risks, this dissertation restricted the scope to prototype testing without the direct feed of concentrated H_2 (system-only operation).

1.3.2 The photocatalysts used in this research are commercial TiO_2-based materials modified by depositing 2% metal.

1.3.3 The study focuses on investigating the effects of reaction temperature, light sources (UVA-LED, LED, and natural sunlight), and sacrificial reagent (methanol) concentration on the efficiency of photocatalytic water splitting.

1.3.4 Quantum chemical calculations are carried out to explore low-energy barrier pathways for H_2 production in aqueous solutions, involving multiple photoexcitation and relaxation processes. Both two- and four-electron pathways for photocatalytic water splitting are considered. Additionally, the influence of photo-to-thermal energy conversion on improving the thermodynamic and kinetic favorability of water splitting is examined. The theoretical investigation focuses on the equilibrium structures of $(TiO_2)_2(H_2O)_2$ model clusters in the ground state (S_0), considering them as either precursor for $S_0 \rightarrow S_1$ photoexcitation or as non-radiative $S_1 \rightarrow S_0$ relaxation products.

1.3.5 The economic feasibility study evaluates the cost of H_2 production (USD/kg H_2), as well as the CO_2-equivalent (kg CO_{2eq}/kg H_2) emissions and cumulative energy demand (CED) per kilogram of H_2 produced.

1.4 Output of the research

1.4.1 Developed a lab-scale process for H_2 production via photocatalysis, advancing from Technology Readiness Level (TRL) 1 to TRL 4.

1.4.2 Presented the research findings at international conferences in four countries: Thailand, Vietnam, Japan, and China, strengthening global academic collaboration.

1.4.3 Published the research results in a high-quality, Q1-ranked (top 6%) international journal, International Journal of Hydrogen Energy (Impact Factor = 8.3).

1.4.4 Provided strategic guidance for green H_2 production via photocatalysis to support energy initiatives in Thailand, promoting green energy and clean technology. The research was funded by the Program Management Unit for Human Resources & Institutional Development, Research, and Innovation (PMU-B) [Grant Number B42G670035].

1.4.5 Served as a prototype for H_2 production technology and contributed to education by facilitating hands-on learning experiences for undergraduate and high school students.

CHAPTER II

LITERATURE REVIEWS

2.1 Hydrogen production technologies

Hydrogen (H_2) can be produced through various methods, broadly classified into non-renewable and renewable processes, as summarized in Fig. 2.1. The figure outlines feedstocks, production costs, processing methods, and the carbon footprint associated with each process (Dincer et al., 2015; Mehmeti et al., 2018). Non-renewable methods include steam methane reforming (SMR) and coal gasification. SMR, the most common approach, produces H_2 from natural gas and steam, offering over 80% efficiency in large systems at a cost of around 2 USD/kg H_2, with fuel costs accounting for approximately 75% (Thibault et al., 2020; Ahmed et al., 2022). Coal gasification, which costs about 1.34-1.63 USD/kg H_2, uses coal, steam, and O_2 but results in significant CO_2 emissions unless carbon capture technologies are employed (Ball et al., 2015). Renewable methods include biomass conversion and water splitting. Biomass gasification and biological processes, such as fermentation, utilize organic waste but are still under development and face challenges such as feedstock competition (Kim et al., 2022). Water splitting techniques, including electrolysis and photolysis, produce clean H_2 but are currently limited by high energy requirements. The choice of production method depends on resource availability, economic feasibility, and environmental impact. The classification of H_2 production colors, as presented in Table 2.1, is delineated according to feedstock sources and production processes.

2.2 Photocatalytic water splitting

Since titanium dioxide (TiO_2) was first used for photocatalytic water splitting under UV light in 1971 (Fujishima et al., 1971 and 1972), it has been widely studied for H_2 generation ($2H_2O \rightarrow 2H_2 + O_2$). With seawater comprising about 97% of Earth's water, its potential for H_2 production is substantial (Fukuzumi et al., 2017; Kumaravel et al., 2018). Research into seawater splitting began in 1997 (Ichikawa, 1997), but

challenges remain due to its high salinity and complex composition, which can deactivate photocatalysts and hinder efficiency (Ji et al., 2007; Li et al., 2019).

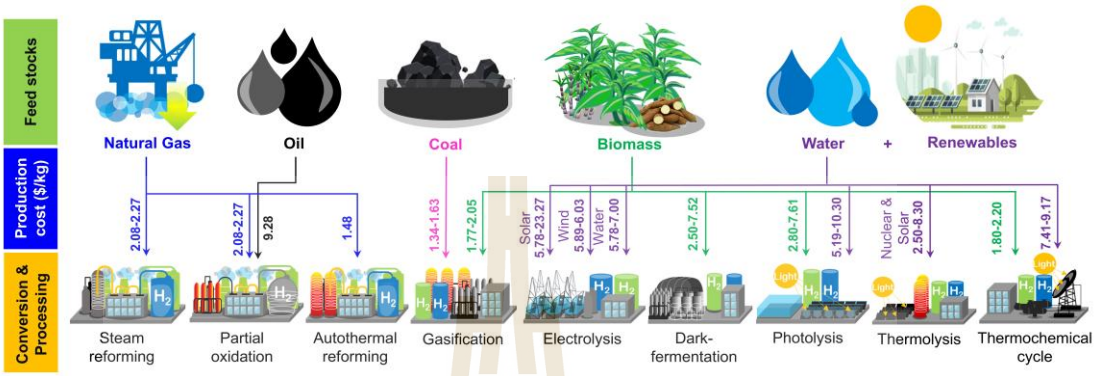

Figure 2.1 Pathways for producing H_2 technology.

Table 2.1 Color classification of H_2 production pathways (Tabrizi et al., 2023).

Category	Color	Process	Source
High environmental footprint (high carbon)	Brown/Black	Gasification	Fossil fuels; Coal
	Gray	Steam reforming	Fossil fuels; Natural gas
Low environmental footprint (low carbon)	Blue	Steam reforming or gasification + CO_2 capture and sequestration (CCS)	Fossil fuels; Natural gas
	Turquoise	Pyrolysis	Fossil fuels; Natural gas
	Yellow	Electrolysis	Water and electricity from the grid (generic)
	Prink/Red	Electrolysis	Water and electricity from nuclear source
	Green	Electrolysis (+biomass*)	Water and electricity from renewable sources/biomass *

* Classification not consolidated.

Despite notable progress, photocatalytic water splitting still faces major challenges such as low efficiency, poor stability, safety risks, and high costs from H_2/O_2 co-production (Aiyun et al., 2019). The reverse reaction between H_2 and O_2 further reduces efficiency and demands expensive gas separation (Jinmeng et al., 2017; Xianjie et al., 2019). To address these issues, partial water splitting using sacrificial agents like methanol or sodium sulfite has been explored to suppress charge recombination (Zheng et al., 2017; Shuang et al., 2020). More recently, intermediate water splitting ($2H_2O \rightarrow H_2 + H_2O_2$) has gained interest, offering a simpler, two-electron route that produces both H_2 and valuable H_2O_2 (Michelle et al., 2016; Kazuhiro, 2018; Nishiyama et al., 2021).

TiO_2 is extensively researched for photocatalytic H_2 production due to its chemical stability, low cost, and non-toxicity (Ismael et al., 2020). However, its practical application is limited by a wide bandgap and rapid charge carrier recombination (Li et al., 2019). To improve efficiency, methods such as metal or nonmetal doping, semiconductor coupling, and cocatalyst loading have been developed (Ismael et al., 2020), with a summary of photocatalyst materials shown in Fig. 2.2. TiO_2 exists in three crystalline forms: anatase, rutile, and brookite. Anatase, with a bandgap of 3.2 eV, is the most photocatalytically active form (Etacheri et al., 2011), while rutile (2.96 eV) is more thermodynamically stable and widely used (Paola et al., 2008). Brookite is less utilized due to synthesis difficulties (Liao et al., 2012). Photocatalytic water splitting proceeds via three steps: (i) light absorption, (ii) charge generation/separation, and (iii) redox reactions on the catalyst surface. For efficient H_2 and O_2 production, the conduction band (CB) must be more negative than 0 V vs. NHE and the valence band (VB) more positive than 1.23 V vs. NHE (Prasad et al., 2020). Recent advancements in photocatalyst systems have shown promising solar-to-hydrogen (STH) efficiencies, as summarized in Table 2.2.

On a lab-scale, the most efficient solar H_2 production methods achieve a STH energy conversion efficiency of 30%, achieved by combining solar cells with equipment (Jieyang et al., 2016). While photocatalytic water splitting typically achieves conversion efficiencies of only about 1-9%, the system design is considerably simpler, cost-effective, and more scalable (Hisatomi et al., 2019; Kim et al., 2019; Nishiyama et al.,

2021; Zhou et al., 2023). Furthermore, current research has successfully produced H_2 from water using a 100 m^2 photocatalysis system. It has been verified that this system is highly safe (Nishiyama et al., 2021).

Despite decades of research, photocatalytic water splitting remains limited to lab-scale batch reactors, with little focus on photoreactor design. In contrast, water purification reactors have advanced significantly toward industrial use (Sundar et al., 2020). Optimizing photoreactor design is key to improving efficiency, scalability, and safety. Effective designs enhance light absorption, reduce energy use, and support industrial transition, but scaling up introduces technical and economic challenges (Huang et al., 2011). Proper sealing is also essential to prevent air intrusion and H_2 loss (Xing et al., 2013; Sundar et al., 2020; Nishiyama et al., 2021).

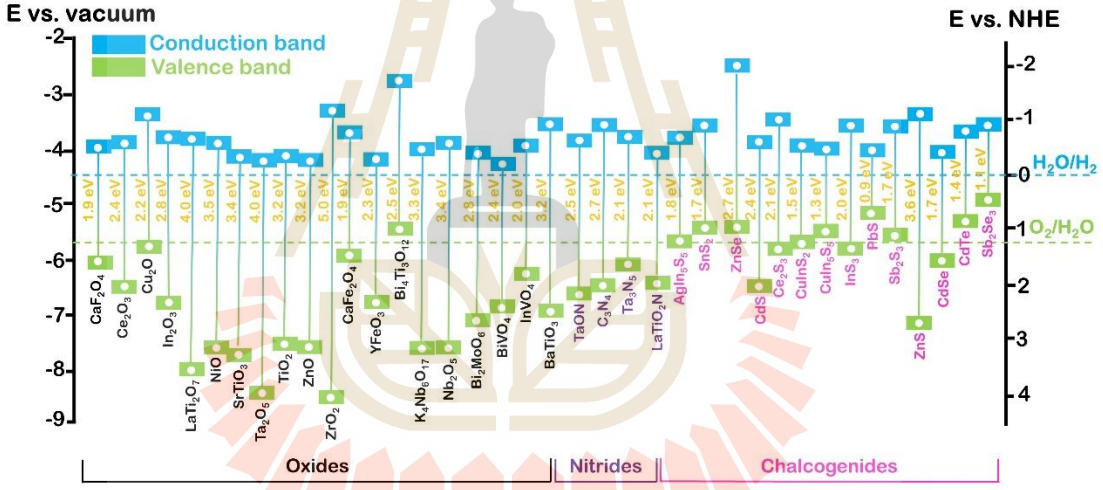

Figure 2.2 Band gap energies and CB (blue) and VB (green) edge positions of the selected oxides, nitrides and chalcogenides with respect to the vacuum level and NHE.

2.3 Photoreactor

Photoreactor design plays a vital role in enhancing the efficiency, scalability, and safety of photocatalytic processes, particularly for water splitting. Effective designs improve light absorption, minimize energy consumption, and support industrial scalability while ensuring safe handling and reduced environmental impact (Kowalska

Table 2.2 Overview of photocatalyst development to improve the %STH for H_2 production by the photocatalysis process (Zhou et al., 2023).

Year	Photocatalysts	Cocatalysts	Light sources	STH (%)	Stability
2023	InGaN/GaN nanowires	Rh/Cr_2O_3, Co_3O_4	Xe lamp with AM1.5G	9.2	74 h
2023	InGaN/GaN nanowires	Rh/Cr_2O_3, Co_3O_4	Natural solar light	6.2	140 min
2014	CoO nanoparticles	N/A	Xe lamp with AM1.5G	5.0	0.5 h
2018	InGaN/GaN nanowires	Rh/Cr_2O_3, Co_3O_4	Xe lamp with AM1.5G	1.9	3 h
2015	Mo:$BiVO_4$-TiO_2/$CH_3NH_3PbI_3$	Pt, $CoCO_3$	Xe lamp with AM1.5G	3.0	12 h
2015	InGaN/GaN nanowires	Ph, Cr_2O_3	Xe lamp with AM1.5G	1.8	10 h
2017	P-doped g-C_3N4 (PCN)	Co_1-P_4	Xe lamp with AM1.5G	0.16	24 h
2013	Si/TiO_2 nano-tree array	Pt-IrO_x	Xe lamp with AM1.5G	0.12	4.5 h
2019	$Y_2Ti_2O_5S_2$ nanoparticles	Rh/Cr_2O_3, IrO_2	Xe lamp with AM1.5G	0.007	20 h
2016	$SrTiO_3$:La/Au/$BiVO_4$:Mo sheet	Rh, $Ru/Cr_2O_3/TiO_2$	Xe lamp with AM1.5G	1.1	20 h
2021	$SrTiO_3$:Al	Rh/CrO_x, CoO_y	Natural solar light	0.76	0.5 h
2018	$SrTiO_3$:Al	Rh/CrO_x, CoO_y	Natural solar light	0.4	0.5 h

et al., 2010; Cassano et al., 2016). Most existing photoreactors like batch-type reactors are used at the lab scale, with magnetic stirring and artificial lighting (Huang et al., 2011; Nickels et al., 2012; Jamali et al., 2013). However, these designs face challenges in large-scale applications due to cost and complexity (Xing et al., 2013). While extensive research exists on photoreactors for water purification (Sundar et al., 2020), fewer studies focus on systems for H_2 production via water splitting, which requires effective

sealing to prevent H_2 loss (Xing et al., 2013; Nishiyama et al., 2021). Advanced designs from water treatment-such as parabolic troughs, inclined plate collectors, and rotating disk reactors-offer valuable insights for developing water splitting systems (Braham et al., 2009; Jing et al., 2010; Loh et al., 2024). To address current limitations, a new panel photoreactor is proposed, emphasizing simple installation, cost savings, and improved performance for lab-scale H_2 production. This design aims to overcome stirring inefficiencies and light distribution challenges, enabling uniform photocatalyst exposure and better scalability potential for future upscaling efforts.

2.4 Hydrogen purification

The effectiveness of H_2 as an energy carrier depends heavily on its purity, which is essential for applications like fuel cells, chemical processes, and advanced manufacturing (Kim et al., 2025). H_2 purification methods are classified into mechanical (e.g., adsorption, membrane separation), chemical (e.g., metal hydrides, catalytic methods), and physical techniques (Kim et al., 2025). Among these, pressure swing adsorption (PSA) and membrane separation are the most widely used (Kalman et al., 2022; Kim et al., 2025). PSA works by passing gas mixtures through adsorbents under high pressure, selectively removing impurities. It typically uses two or more columns to alternate between adsorption and regeneration, creating dynamic pressure, temperature, and composition changes (Morales et al., 2022).

PSA is extensively used for large-scale H_2 purification from steam methane reforming (SMR), effectively removing CO_2, CH_4, and CO, and achieving H_2 recovery rates above 99% (Król et al., 2024). However, its application to H_2/O_2 mixtures from photocatalytic water splitting is still limited. Most PSA studies have focused on mixtures like $H_2/CO_2/CH_4/CO/N_2$. For example, a two-bed PSA using zeolite 5A and activated carbon achieved H_2 purities of 96-99.5% and recoveries of 71-85% (Ahn et al., 2012). Another study using Cu-BTC and zeolite 5A in layered beds attained 95.47% H_2 purity and 83.22% recovery (Sun et al., 2022). In binary mixtures with 15-25% CO_2, palm kernel shell activated carbon and hollow fiber sorbents produced 99% purity and 88.1% recovery (Sircar et al., 2000; Lively et al., 2012). Similarly, purification of a

$H_2/N_2/CH_4/Ar$ (58/25/15/2% volume) mixture with zeolite 5A resulted in 99.25-99.97% H_2 purity and 55.5-75.3% recovery (Yáñez et al., 2020).

In contrast, PSA for O_2 purification is less studied. One approach combined N_2 adsorption on zeolite with O_2 enrichment via a polymer membrane, achieving 99.5% O_2 purity using a hybrid PSA/CMC system (Mercea et al., 1994). Another study showed that increasing O_2 concentration in the feed improved recovery and purity. For example, a feed of 95/4/1% volume ($O_2/Ar/N_2$) achieved 99.8% purity and 56.9% recovery (Kim et al., 2005).

2.5 Quantum chemical calculation

Photocatalytic water splitting for H_2 production can proceed through two pathways: the two-electron pathway ($2H_2O \rightarrow H_2O_2 + H_2$) and the four-electron pathway ($2H_2O \rightarrow O_2 + 2H_2$) (Liao et al., 2014; Xue et al., 2019; Malik et al., 2020; Nishiyama et al., 2021; Zhou et al., 2023). The two-electron process is thermodynamically more favorable, with a lower enthalpy change (384.1 kJ/mol) compared to the four-electron pathway (484 kJ/mol) (Chase, 1998). Despite significant experimental efforts to evaluate quantum yields and H_2 evolution rates, the detailed molecular mechanisms, especially on TiO_2 surfaces and clusters, remain unclear.

Theoretical studies, mostly using density functional theory (DFT), have examined water splitting on various TiO_2 surfaces such as rutile (110), anatase (101), and brookite (210). These studies suggest the two-electron oxidation to H_2O_2 proceeds via surface peroxide intermediates, with OH* formation being the rate-determining step (Malik et al., 2020; Harb et al., 2019). Research using DFT and the nudged elastic band (NEB) methods on 2D TiO_2 nanosheets showed enhanced hole-trapping at Ti–OH sites, beneficial for the oxidation half-reaction (Jiang et al., 2022).

Cluster model calculations (e.g., $(TiO_2)_n(H_2O)_m$) further revealed insights into water adsorption and dissociation. Dissociative adsorption is favored on under-coordinated Ti sites and becomes less exothermic as more water is added due to full Ti coordination (Chen et al., 2015). Calculations on small TiO_2 clusters in singlet (S_0) and triplet (T_1) states confirmed that water splitting can occur in both states with energy barriers ranging from 21-109 kJ/mol (Wang et al., 2011).

Extended models using $(MO_2)_n$ clusters (M = Ti, Zr, Hf) suggest that the reactions preferentially proceed on T_1 surfaces. H_2 formation occurs through H transfer to metal centers followed by recombination and desorption, not direct H–H coupling (Fang et al., 2013). However, energy barriers for full H_2/O_2 production remain high, especially for $(TiO_2)_2$ clusters ($\Delta E^{\ddagger}$ up to 749 kJ/mol), indicating the critical need for photon energy input and possibly solvent stabilization (Fang et al., 2013).

Although some low-barrier pathways have been proposed (Pandey et al., 2012), recent photochemical studies (Siriwibool et al., 2020; Khrootkaew et al., 2023; Suwannakham et al., 2024; Panajapo et al., 2024) indicate the energy requirements are still significant. Importantly, most prior research focused on single-state potential energy surfaces in the gas phase, overlooking excited-state transitions and solvent effects, which are essential for a complete understanding of photocatalytic water splitting (Wang et al., 2011; Fang et al., 2013; Chen et al., 2015; Malik et al., 2020; Jiang et al., 2022).

CHAPTER III

MATERIALS AND METHODS

3.1 Lab-scale design of the photocatalytic water splitting process

This study aims to develop a conceptual framework for transitioning hydrogen (H_2) production using batch photoreactors commonly used in small-scale laboratory investigations towards a continuous process system. As illustrated in Fig. 3.1, the proposed prototype process was designed to resemble industrial operations while remaining at the lab-scale. The lab-scale prototype comprises several key units, with the core being a continuous-panel photoreactor for H_2 production via photocatalytic water splitting (Fig. 3.1(B)). However, the research team recognized that for the produced H_2 to be practically utilized, further processing is required to purify the gas. Therefore, additional system components were incorporated to present a complete prototype process. Among various H_2 purification techniques, such as membrane separation and pressure swing adsorption (PSA), this study selected PSA technology (Fig. 3.1(E)) for the prototype due to its commercial scalability and compatibility with large-scale industrial applications. This purification unit is preceded by a moisture removal unit using zeolite adsorption (Fig. 3.1(D)), and the entire system is thermally regulated using a temperature-controlled bath capable of maintaining temperatures between 10 and 100 °C (Fig. 3.1(F)). The fluid circulation throughout the system is driven by a peristaltic pump (Fig. 3.1(A)), which draws from a 500 mL storage tank (Fig. 3.1(C)). In addition, the prototype process is equipped with a comprehensive sensor and control system, with instrumentation installed at key points, as shown in Fig. 3.2. The complete system integrates three main modules namely, the H_2 production unit (continuous panel photoreactor), the dehumidification unit, and the PSA-based purification unit providing a near-industrial representation of an operational H_2 production process.

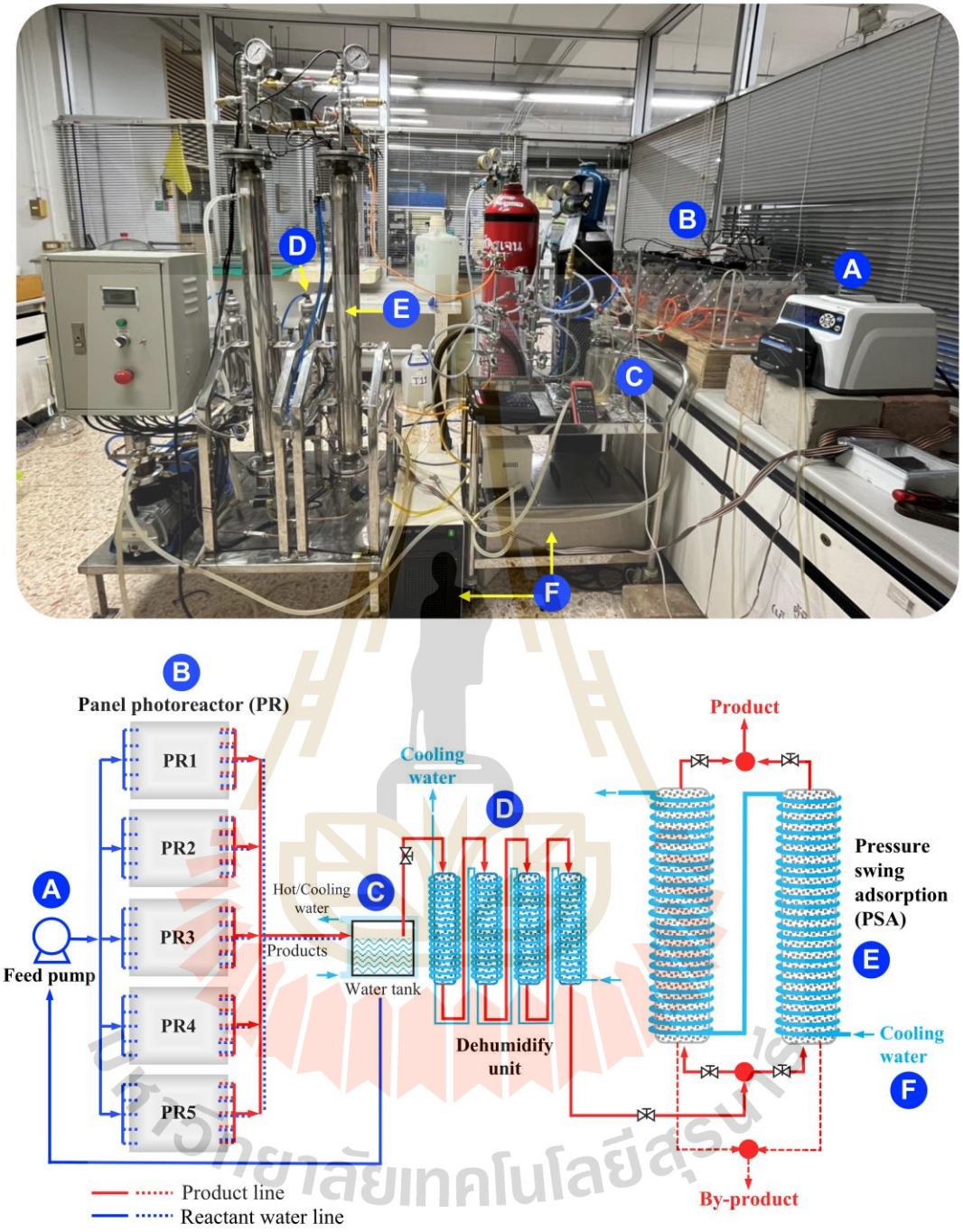

Figure 3.1 Lab-scale prototype of the H_2 production system via photocatalysis.

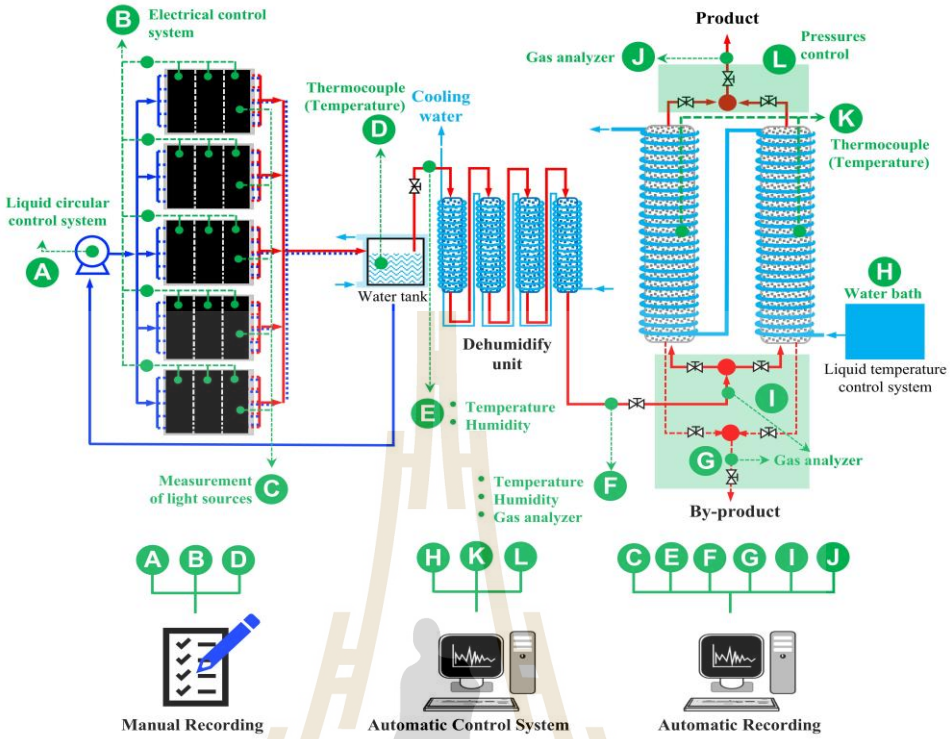

Figure 3.2 Schematic representation of the instrumentation and control system integrated into the photocatalytic H_2 production process.

3.1.1 Panel photoreactor design and setup

The panel photoreactor was designed for photocatalytic water splitting to produce H_2 in a continuous process as show in Fig. 3.4. From Fig. 3.4(a), it has external dimensions of 21.0 × 29.5 cm and internal dimensions of 16.5 × 24.5 cm, with a photocatalyst material measuring 15.0 × 23.0 cm. To enhance liquid flow, the panel photoreactor is installed at a 60° angle, as depicted in Fig. 3.4(b). Preliminary studies (Fig. 3.3) indicate that the performance of photocatalytic water splitting is influenced by the incident angle of the light source and the panel photoreactor's orientation. To optimize efficiency, this study installs the light source parallel to the panel photoreactor (Fig. 3.4(b)). Three different light sources were tested using the same panel photoreactor setup: UVA-LED (UVA-LED IP65; 50W) for wavelength scanning, as shown in Fig. 3.5(a); LED (LED IP65; 50W) for wavelength scanning, as shown in Fig. 3.5(b); and natural sunlight during February 2025 at Suranaree University of Technology, Thailand, as shown in Fig. 3.4(f), with wavelength scanning in Fig. 3.5(c). For multispectral analysis of the light source, an AS7341 11-channel spectral sensor (GY-

AS7341 11 CH) was used. Both the UVA and LED sources are mounted at the top (Fig. 3.4(e)), with a 4.5 cm gap between the light source and the photoreactor surface (Fig. 3.4(b)). This gap allows the temperature in the system to increase slightly by ~1.5 °C (UVA-LED) and ~3 °C (LED) due to heat transfer from the light source to the panel photoreactor. The panel photoreactor is equipped with quartz windows (JGS-1 grade; transmission rate at the wavelength of 185-2500 nm) at the top, leaving a 3 mm gap between the quartz window and the photocatalyst material to form a thin water film (water flows from the bottom of the panel photoreactor to the top plate). Fig. 3.4(c) provides an overview of the full system, which consists of five parallel photoreactors operating under identical conditions. The setup includes a peristaltic pump to regulate liquid flow at 52 ml/min (Masterflex® L/S®; easy-load® II, Model 77202-60), a water bath for temperature control (HAAKE DC 30 and EK 20), and a thermocouple for temperature monitoring (Digital thermometer; RS PRO, RS 5311), all operating under atmospheric pressure. Gas production is analyzed using gas chromatography (GC-GAS; Agilent, 7890A) and a H_2 sensor (Gas detector GAP-H2; Switzerland). Fig. 3.4(d) illustrates the process flow diagram of photocatalytic water splitting in the panel photoreactor.

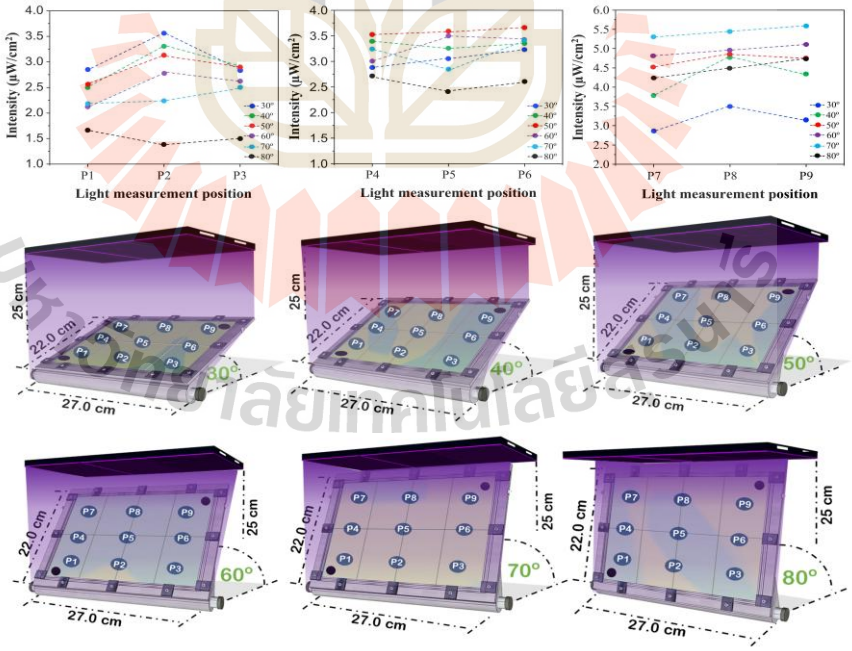

Figure 3.3 Schematic of the panel photoreactor at different incident angles and the light intensity at various positions on the panel photoreactor.

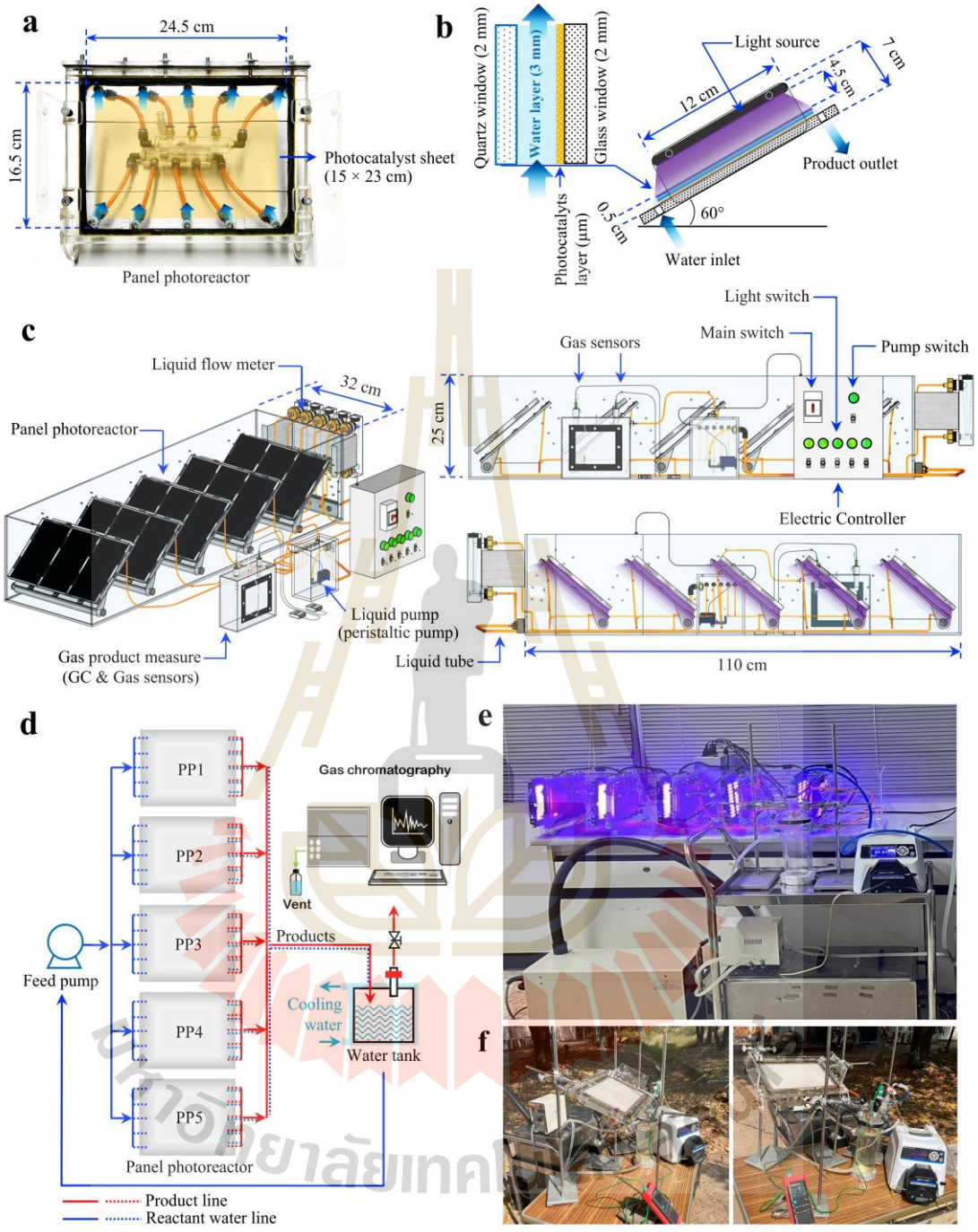

Figure 3.4 Photocatalytic water splitting for H_2 production using a panel photoreactor in a continuous process: (a) panel photoreactor design, (b) installation setup, (c) continuous operation of the panel photoreactor, (d) process flow diagram, (e) lab-scale testing with UVA-LED and LED light sources, and (f) lab-scale testing with natural sunlight.

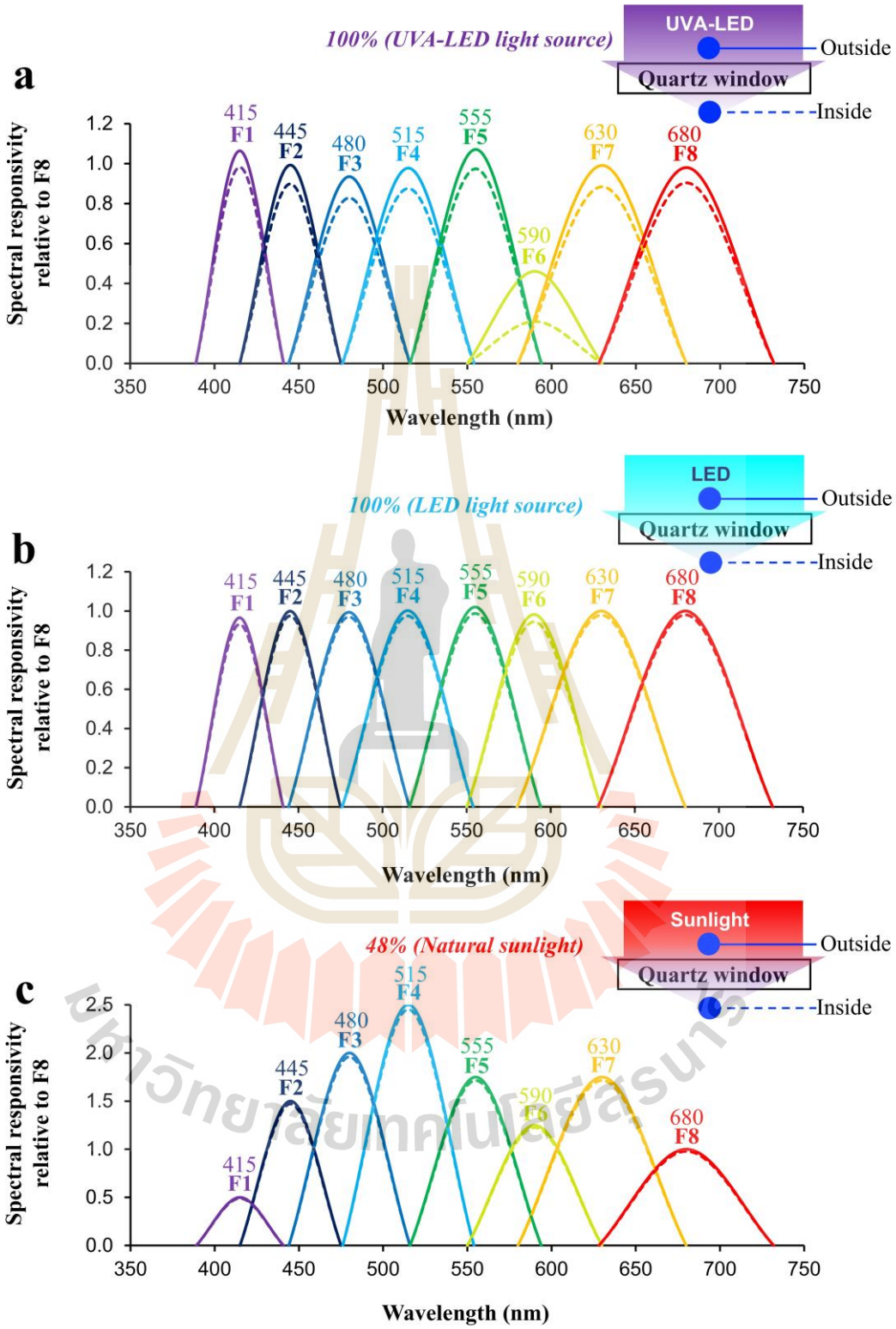

Figure 3.5 Wavelength scan of the light source inside and outside the panel photoreactor for (a) a UVA-LED light source, (b) an LED light source, and (c) natural sunlight.

3.1.2 Dehumidify unit

After the mixed gas product is generated from the continuous panel photoreactor, it exhibits a relative humidity of approximately 60% RH. This moisture is removed using an adsorption column system, as shown in Fig. 3.6. The moisture removal unit consists of four adsorption columns connected in series →[A]→[B]→[C]→[D]→, as illustrated in Fig. 3.7(a). Each column has an internal diameter of 4 cm and a height of 50 cm. The inner pipe is enclosed within an outer pipe, leaving a 1 cm gap between the two, which serves as a channel for cooling water circulation. The cooling system is temperature-regulated at 25 °C using a temperature-controlled bath (HAAKE DC 30 and EK 20) throughout the entire process. Inside each column, 3A-type zeolite adsorbent is packed (Fig. 3.7(b)-(c)), with a particle size of 0.1972 cm (Fig. 3.7(d)). Surface morphology and characteristics of the zeolite material were analyzed using SEM, as shown in Fig. 3.7(e)-(f). Each column is filled with 670 grams of 3A zeolite. Additional physicochemical properties of the 3A zeolite are provided in Table 3.1. The surface properties of 3A zeolite, analyzed using nitrogen adsorption-desorption techniques, reveal a specific surface area of 21.13 m^2/g, a micropore volume of 8.23×10^{-6} cm^3/g, and an average pore diameter of 16.76 nm.

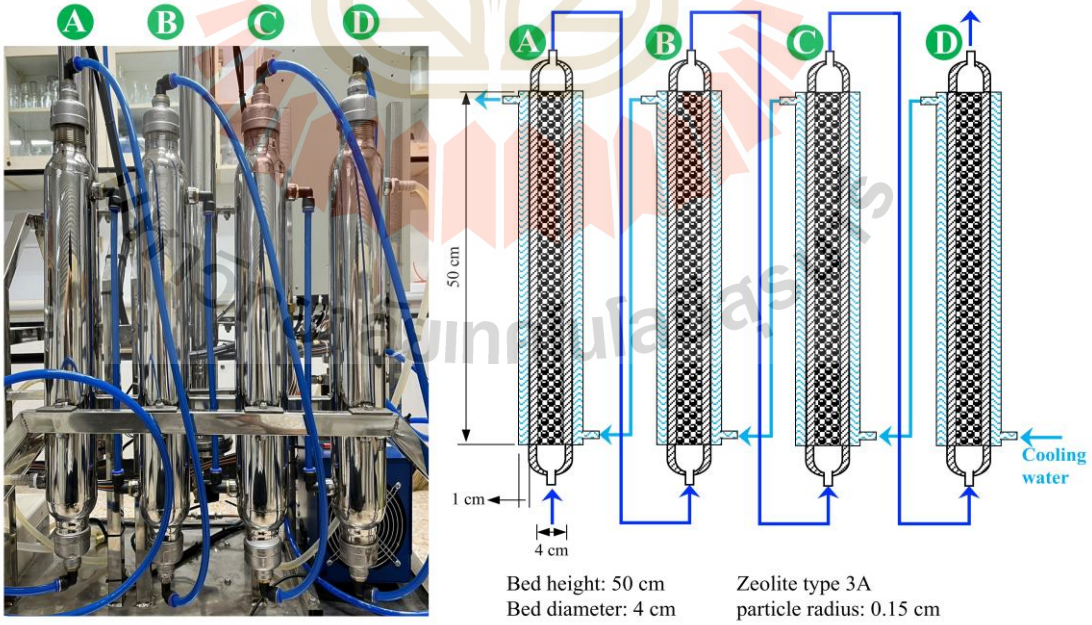

Figure 3.6 Lab-scale prototype of the moisture removal unit employing 3A-type zeolite adsorption in the H_2 production process.

Table 3.1 Specific characteristics of 3A-type zeolite.

Properties	Unit	Bead		Pellet		Note
Diameter	mm	1.6-2.5	3.0-5.0	1/16”	1/8"	-
Static water adsorption	%wt.	≥21.50	≥21.50	≥20.00	≥20.00	75%RH, 25 ℃
Bulk density	g/ml	≥0.74	≥0.74	≥0.65	≥0.65	Tapped
Loss on Ignition	%wt.	≤1.50	≤1.50	≤1.50	≤1.50	575 ℃, 1 hr
Loss on attrition	%wt.	≤0.10	≤0.10	≤0.30	≤0.30	-
Crush strength	N	≥30.00	≥80.00	≥30.00	≥70.00	Avg. 25 bead
Particle ratio	%	≥ 97.00	≥99.00	-	-	-

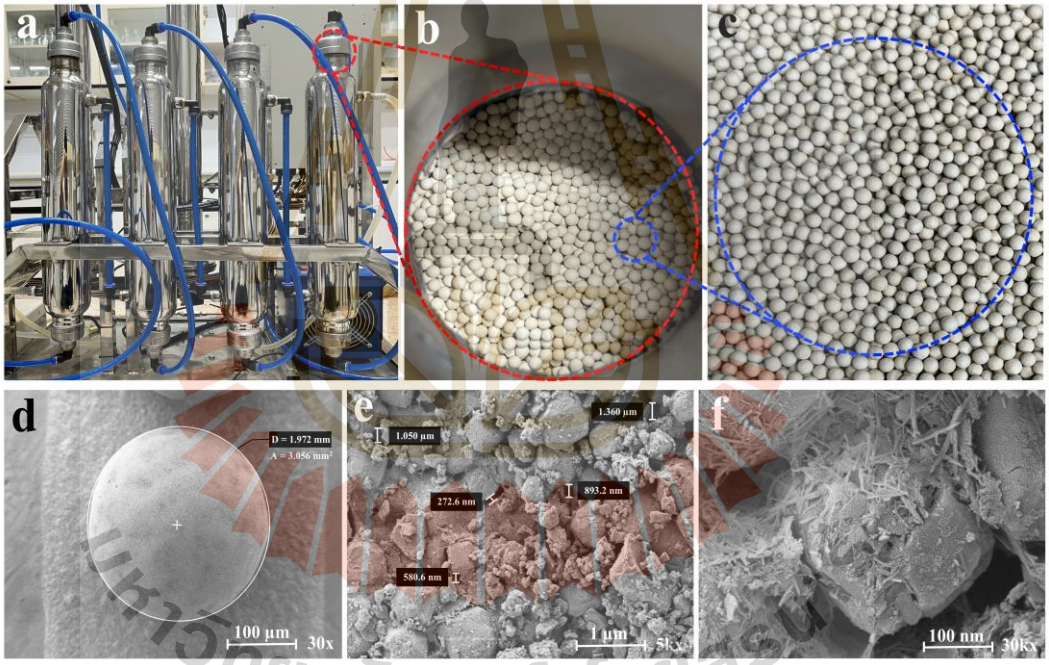

Figure 3.7 Dehumidifier unit: (a) adsorption columns; (b) packed 3A zeolite inside the column; (c) 3A zeolite and surface morphology analyzed by SEM; (d) particle size; (e) surface structure; and (f) pore characteristics on the 3A zeolite surface.

3.1.3 H_2 purification unit

As shown in Fig. 3.8, the H_2 purification unit using pressure swing adsorption (PSA) consists of two adsorption columns (Fig. 3.8(a)) packed with 5A-type

zeolite adsorbent (Fig. 3.9(b)-(c)) having a particle size of 0.20 cm (Fig. 3.9(d)). The columns are arranged in parallel to allow gas flow between them (Fig. 3.8(c)). The system employs 11 solenoid valves (Fig. 3.8(b)) for automated valve control, enabling cyclic operation through different stages including adsorption, depressurization, purging, and repressurization. The feed gas and is processed under operating conditions of 950 kPa production pressure at 25 °C, with the purge pressure maintained at 100 kPa (atmospheric pressure). Surface properties of the 5A zeolite, analyzed via nitrogen adsorption-desorption techniques, show a specific surface area of 551.15 m^2/g, a micropore volume of 0.18 cm^3/g, and an average pore diameter of 3.74 nm. Additional surface morphology analyses using SEM are presented in Fig. 3.9(d)-(f). The PSA unit operates under a four-step cycle for H_2 purification, as illustrated in Fig. 3.8(d). The cycle consists of the following steps: adsorption, depressurization, purging, and pressurization.

Adsorption: In the first step, Bed 1 (B1) adsorbs and separates H_2 for 70 seconds, allowing purified H_2 to exit the system. Simultaneously, Bed 2 (B2) undergoes a purging process to clean the zeolite adsorbent.

Depressurization: B1 is rapidly depressurized for 3 seconds to regenerate the adsorbent. Concurrently, B2 continues purging to prepare for the next adsorption cycle. These two actions occur simultaneously.

Purging: B1 is purged for 70 seconds to remove the adsorbed gases, while B2 begins a new adsorption cycle.

Pressurization: B1 is repressurized for 3 seconds to restore the initial operating pressure and prepare for the next cycle, while B2 performs an additional purging step during the same interval.

The duration and configuration of each step, including valve operation, are based on the pressure profiles inside the columns. One key consideration is that prolonged adsorption may lead to adsorbent saturation, resulting in reduced H_2 separation efficiency. Conversely, shorter depressurization and purging steps help regenerate the adsorbent more effectively by releasing adsorbed O_2. All solenoid valve operations are controlled automatically, with gas sensors installed at positions V1, V6, and V11, as shown in Fig. 3.8(b). Each column is packed with 945 grams of 5A zeolite. The physical and structural properties of the 5A zeolite are detailed in Table 3.2.

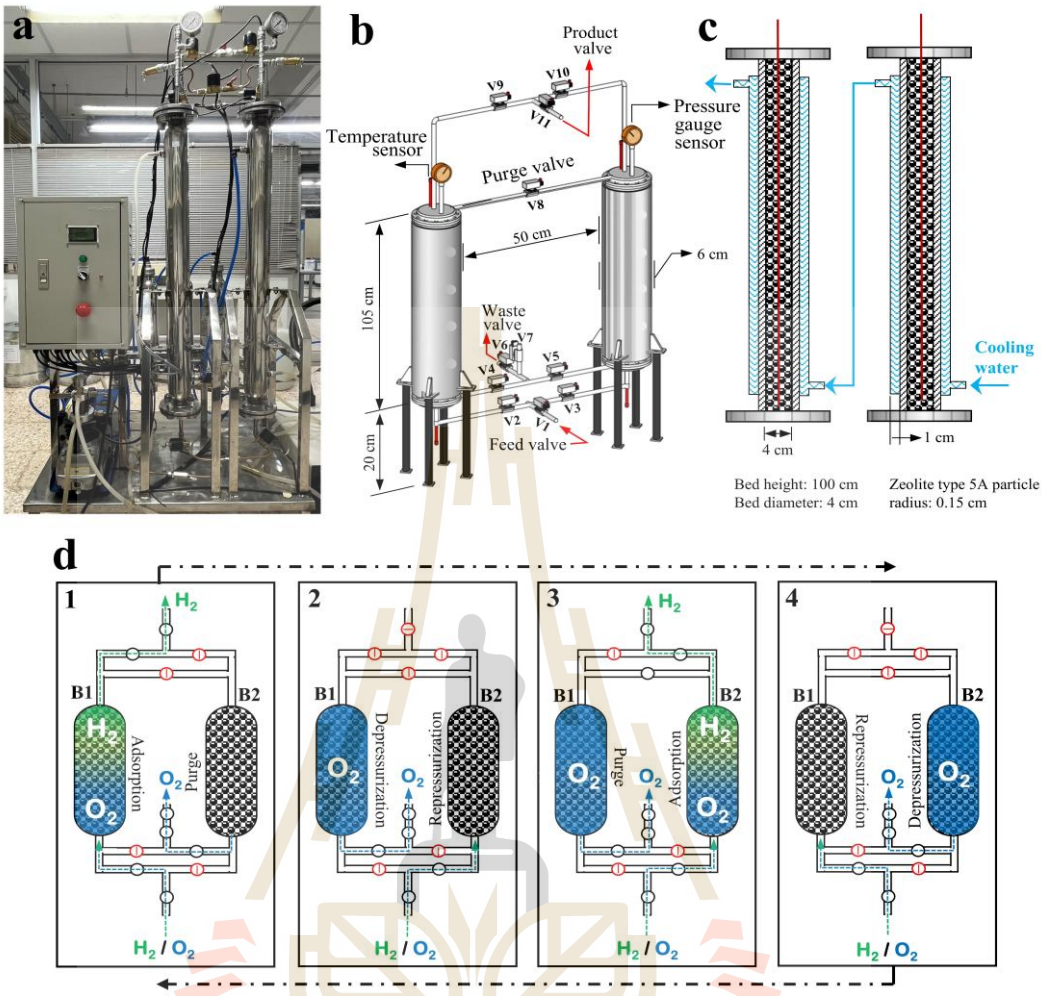

Figure 3.8 Prototype of H_2 purification unit using PSA technique: (a) Lab-scale PSA prototype, (b) Components and installation, (c) Internal schematic of the column, and (d) Operating cycle.

Table 3.2 Specific characteristics of 5A-type zeolite.

Properties	Unit	Bead		Pellet		Note
Diameter	mm	1.6-2.5	3.0-5.0	1/16”	1/8"	-
Static water adsorption	%wt.	22.00	22.00	21.00	21.00	75%RH, 25 °C
Bulk density	g/ml	0.70	0.68	0.64	0.64	Tapped
Water content	%wt.	1.50	1.50	1.50	1.50	575 °C, 1 hr
Loss on attrition	%wt.	0.10	0.10	0.20	0.30	-
Crush strength	N	30.00	80.00	30.00	80.00	Avg. 25 bead

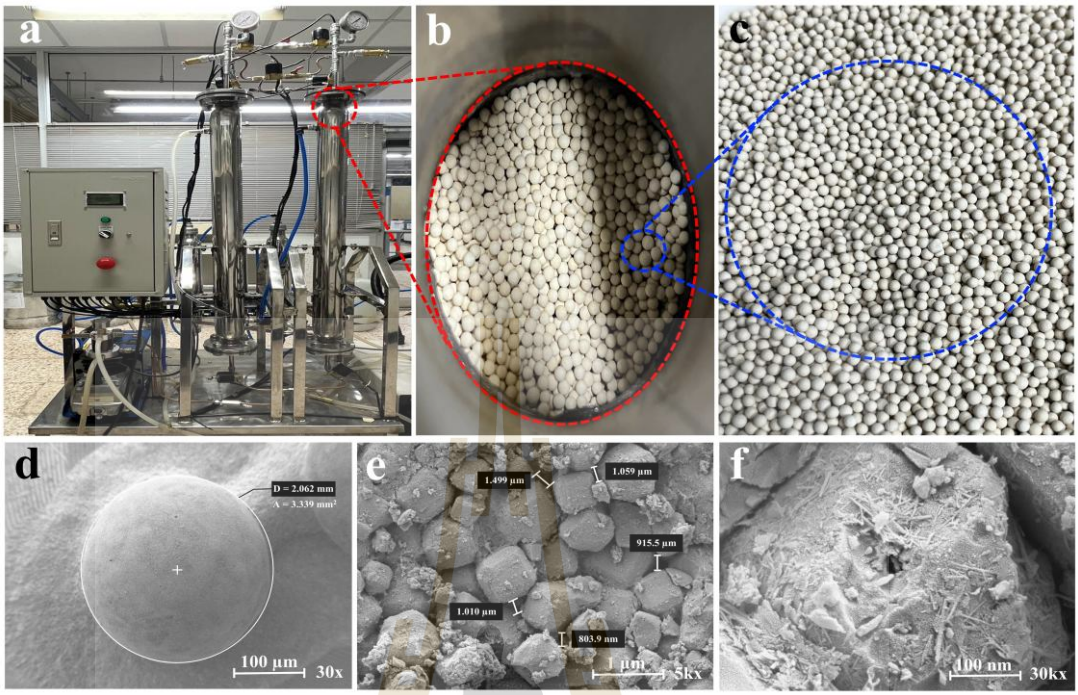

Figure 3.9 H_2 purification unit using PSA technique: (a) PSA unit under the project, (b) packing configuration of 5A zeolite inside the column, (c) 5A zeolite and surface morphology analysis by SEM technique, (d) particle size, (e) surface characteristics, and (f) surface pore structure of 5A zeolite.

3.2 Preparation of photocatalyst materials

3.2.1 Preliminary photocatalyst testing for photocatalytic water splitting

All chemicals used were of reagent grade and required no further purification. In our preliminary studies on photocatalyst preparation, we focused on commercial TiO_2-anatase (98.8% TiO_2-anatase, DHA-100, Guangxi Bluestar Dahua Chemical Co., Ltd., China) as the base material for synthesizing various photocatalysts, including 2%Pt/TiO_2, 2%Ag/TiO_2, 2%Pt/$SrTiO_3$, 2%RuRh/$SrTiO_3$, and 2%Al/$SrTiO_3$.

Strontium titanate ($SrTiO_3$) was synthesized via a solid-state reaction using strontium carbonate ($SrCO_3$) (97.5%, Alfa Aesar) (1.6093 g) and TiO_2 (0.8706 g). The mixed $SrCO_3$ and TiO_2 powders were calcined at 1200 °C at a heating rate of 5 °C/min for 2 h following the reaction: $SrCO_3 + TiO_2 \rightarrow SrTiO_3 + CO_2$, and confirmed the crystal structure using the XRD technique, as shown in Fig. 3.10. After that, 2% metal was deposited on the surface of the $SrTiO_3$ and TiO_2 photocatalysts.

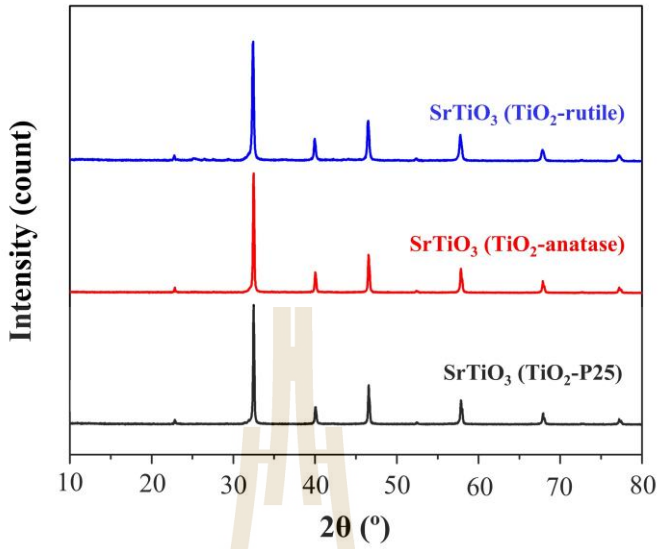

Figure 3.10 The XRD patterns were used to analyze the crystal structure of $SrTiO_3$ synthesized via the solid-state reaction at 1200 °C of $SrCO_3$ with different types of TiO_2 (e.g., rutile, anatase, and P25, which contains both anatase and rutile phases).

All synthesized photocatalyst powders were tested in a batch photoreactor (Fig. 3.11(a)-(b)) under the following conditions: 40 mL of solution (either 10% MeOH (99.9% methanol (MeOH), Carlo Erba) or deionized water (DI water)), 50 mg of photocatalyst, a 300 W Xe lamp (PLS-SXE300D/300DUV; Perfect Light) without a filter, and Ar as the gas carrier at 25 °C. Preliminary results (Fig. 3.11(c)) showed that the H_2 evolution rates in the presence of a sacrificial agent (10% MeOH) were: 490 μmol g^{-1} h^{-1} for 2%Pt/TiO_2, 320 μmol g^{-1} h^{-1} for 2%Pt/$SrTiO_3$, 145 μmol g^{-1} h^{-1} for 2%RuRh/$SrTiO_3$, and 140 μmol g^{-1} h^{-1} for 2%Ag/TiO_2. When tested with DI water, the H_2 evolution rates for 2%Pt/$SrTiO_3$ and 2%Al/$SrTiO_3$ were similar, both at 85 μmol g^{-1} h^{-1}. These results indicate that 2%Pt/TiO_2 exhibited the highest photocatalytic efficiency among the tested materials, making it the focus of this study.

Further tests (Fig. 3.11(d)) involved coating 2%Pt/TiO_2 onto a glass sheet (2 × 2 cm) using different TiO_2 sources (TiO_2-anatase and TiO_2-P25 (P25; Acros Organics)). We found that applying a 16.67 mg photocatalyst coating to the substrate before reaction testing (Fig. 3.11(d)) resulted in better performance compared to using 50 mg of powdered photocatalyst (Fig. 3.11(c)). Since the photocatalyst powder is

immobilized on the material, it can interact more efficiently with the light source. Additionally, TiO_2-anatase outperformed P25 in this system, demonstrating higher photocatalytic activity.

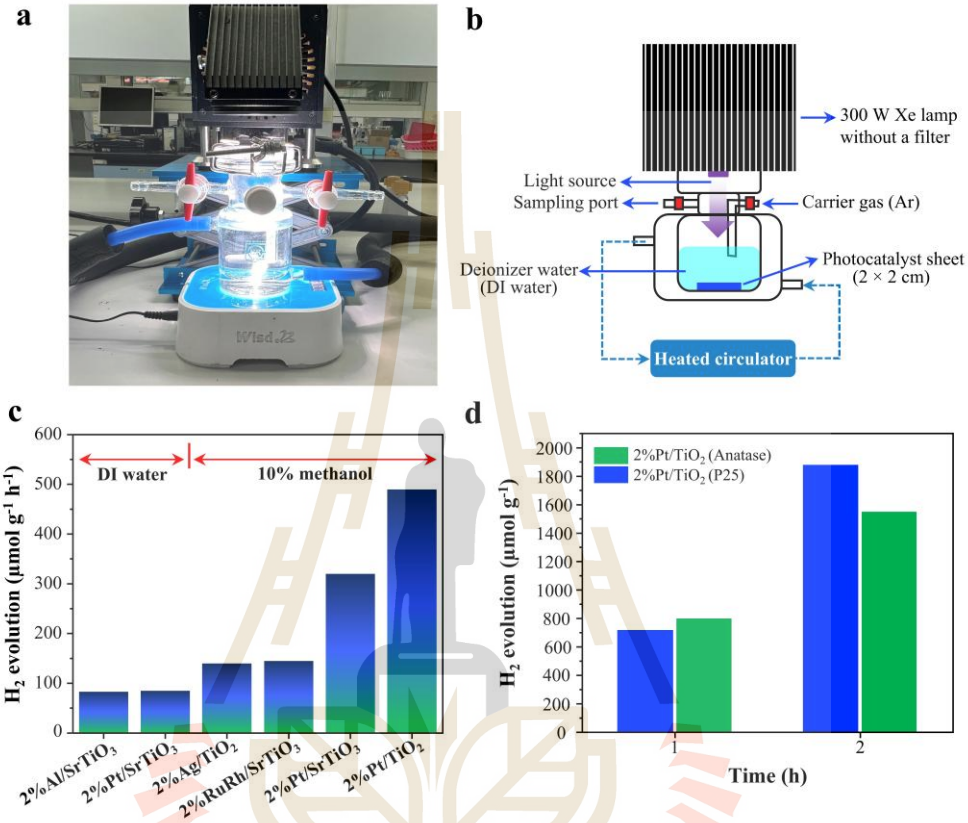

Figure 3.11 (a) Batch photoreactor setup, (b) schematic diagram of the photoreactor with detailed components, (c) comparison of 50 mg photocatalyst powder performance with and without a sacrificial reagent (10% MeOH) at 25 °C, and (d) 2%Pt/TiO_2 photocatalyst (using TiO_2-anatase and TiO_2-P25) coated on a glass sheet of 2 × 2 cm (16.67 mg) and tested for photocatalytic water splitting in a 10% MeOH.

3.2.2 Preparation of photocatalyst materials

From preliminary studies, we selected 2%Pt/TiO_2 as the primary photocatalyst for this research. The preparation involved mixing 1 g of TiO_2-anatase powder with 800 µL of polyurethane (TOA polyurethane) before coating it onto a 15 × 23 cm glass sheet (Fig. 3.12(a)), covering an active area of 14 × 22 cm (308 cm^2) (Fig. 3.12(b)). The coated sheet was dried at 60 °C for 24 hours (Fig. 3.12(c)) and then

calcined at 500 °C at a heating rate of 5 °C/min for 3 hours (Fig. 3.12(d)-(e)). Subsequently, H_2PtCl_6 (2% w/w platinum; Merck) was deposited onto the TiO_2-coated material using the photodeposition technique with a UV light source. After photodeposition, 2% w/w of Pt was further deposited onto the photocatalyst surface, followed by drying at 80 °C for 24 hours.

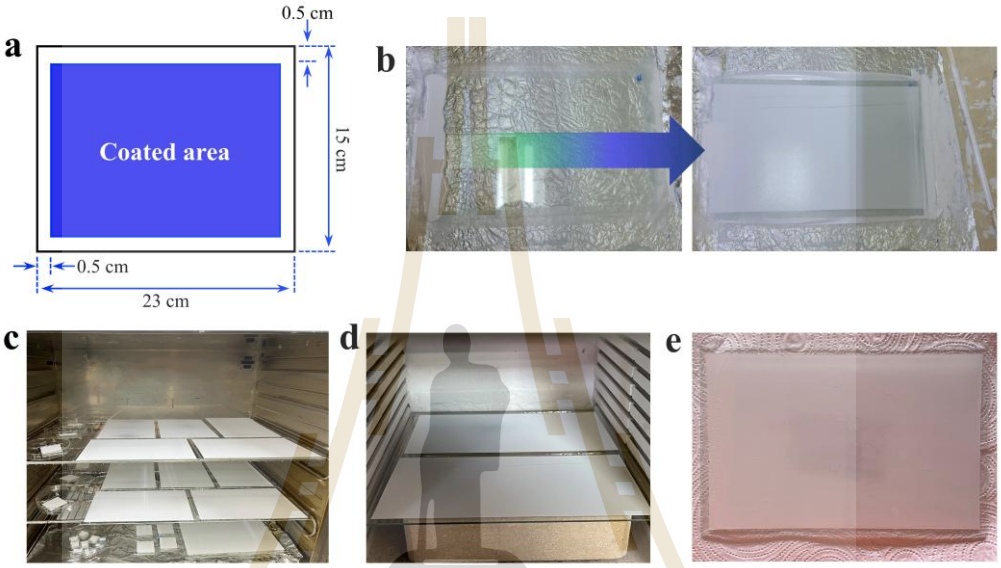

Figure 3.12 The TiO_2-anatase photocatalyst powder was coated onto a glass sheet (15 × 23 cm). The following steps were performed: (a) a schematic of the coated area on the material, (b) the coating method, (c) drying at 60 °C for 24 hours, (d) calcination at 500 °C with a heating rate of 5 °C/min for 3 hours, and (e) the photocatalyst material without metal loading.

3.2.3 Photocatalyst characterizations

The crystal structures of commercial TiO_2-anatase, $SrTiO_3$ and 2%Pt/TiO_2 were identified using X-ray diffraction (XRD) with a Bruker D2 Phaser diffractometer, employing Cu-Kα radiation (λ = 1.5406 Å). XRD patterns were collected over a 2θ range of 10° to 80° using Bragg-Brentano geometry. The band gap energy of the photocatalysts was measured using an Ultraviolet-visible spectrometer (UV-Vis; Agilent, Cary 300). The measurement parameters were set as follows: a wavelength range of 250-800 nm, a spectral bandwidth (SBW) of 2 nm, and a data interval of 1 nm. The resulting spectra for TiO_2 and 2%Pt/TiO_2 showed absorbance as a function of

wavelength. The spectral data revealed a significant cut-off point where the absorbance value was at its lowest. The band gap energy of the sample was estimated using the Tauc method, which assumes that the energy-dependent absorption coefficient (α) follows the equation: $(\alpha h\upsilon)^{1/\gamma} = B(h\upsilon - E_g)$ where h is Planck's constant, υ is the photon frequency, E_g is the band gap energy, and B is a constant. The γ factor depends on the nature of the electronic transition, with values of 1/2 for direct band gaps and 2 for indirect band gaps (Makula et al., 2018). The specific surface area, pore volume, and pore diameter of the TiO_2 photocatalyst were measured using a Bel-Japan Belsorp Mini (BET surface area analyzer). Before the surface area measurement, the samples were degassed at 1.6 Pa and 200 °C for 4 hours in an N_2 environment using a degassing device to remove adsorbed contaminants. The specific surface area of the photocatalyst was determined using the N_2 adsorption-desorption method. The morphology and internal features of the composite were analyzed using a Field Emission Scanning Electron Microscope and Energy-dispersive X-ray spectroscopy (FESEM/EDS, JEOL, JSM 7800F).

3.3 Computational methods

3.3.1 Quantum chemical methods

The present theoretical study began by calculating the equilibrium structures of all molecules in the hypothesized elementary reactions in the ground state (S_0) and the excited electronic state (S_1) using DFT and TD-DFT methods with the Becke, three-parameter, and Lee-Yang-Parr hybrid functionals and triple-zeta basis sets, abbreviated DFT/B3LYP/TZVP and TD-DFT/B3LYP/TZVP methods, respectively.

Remarks should be made on applying the TD-DFT method with the B3LYP hybrid functional. The TD-DFT method has become a primary theoretical method for excited state calculations on large molecules and avoids direct state calculations by concentrating solely on excitation energy and transition dipole moment (González et al., 2012). However, benchmark TD-DFT calculations have shown that pure density functionals often underestimate transition energies, while hybrid functionals, such as B3LYP, provide more accurate results, particularly for low-lying singlet transition states (Jacquemin et al., 2011).

In practice, the presence of the nearly degenerate highest occupied molecular orbital and lowest unoccupied molecular orbital energies at the intersections of the S_0 and S_1 states causes spin instability, which is linked to holes located below the Fermi level. The theoretical findings in Ref. (Tapavicza et al., 2008) demonstrated that this issue can be avoided by using the Tamm-Dancoff approximation (TDA) alongside the TD-DFT method. As a simplified version of the full TD-DFT method, the TD-DFT/TDA approach greatly enhances computational efficiency by truncating full equations to reduce algorithmic failures caused by spin instability (Wang et al., 2008). Thus, the TD-DFT/B3LYP method with TDA was applied in this study and in all of our previous studies on large molecular systems (Siriwibool et al., 2020; Khrootkaew et al., 2023; Suwannakham et al., 2024; Panajapo et al., 2024).

3.3.2 PES calculations

Because the transitions from the ground electronic state (S_0) to the lowest triplet electronic excited state (T_1) are generally forbidden, the present TD-DFT/B3LYP/TZVP calculations focused primarily on the reaction on the S_1 PESs, on which the $S_0 \rightarrow S_1$ excitation energy, characteristic structures, S_0/S_1 intersection, and nonradiative $S_1 \rightarrow S_0$ relaxation were calculated and analyzed. Based on the hypothesized pathways (Wang et al., 2011; Fang et al., 2013; Chen et al., 2015), the PESs in the S_1 and S_0 states were preliminarily scanned using a double-ended equilibrium structure method (Halgren et al., 1977; Plessow et al., 2013), which is based on self-consistent optimizations of the PESs (Halgren et al., 1977; Plessow et al., 2013). In this case, TURBOMOLE 7.80 software package (TURBOMOLE V7.8 2023) was used in the PES calculations.

The equilibrium structures at the stationary points in the S_1 and S_0 states and the structures at the S_0/S_1 intersections were reoptimized at the same level of theory. The PESs were then refined using the nudged elastic band (NEB) method included in ORCA 6 software package (Neese et al., 2012 and 2022), from which some photophysical properties [e.g., excitation energy (ΔE^{Ex})] were calculated. To study the solvent effects, the conductor-like screening model (COSMO) (Klamt et al., 1993 and 1998) was also included in the quantum chemical calculations, with the dielectric constants, ε = 80, for the aqueous solution.

3.3.3 Kinetic and thermodynamic property calculations

Characteristic structures of the chemical species on the S_1 and S_0 PESs were used to calculate rate constants using the TST method (Hänggi et al., 1990; Pollak et al., 2005). In this study, the quantized vibrational rate constants ($k^{Q\text{-}vib}$) were determined over the temperature range of 280-3000 K using Eq. (3.1):

$$k^{Q\text{-}vib}(T) = \frac{k_B T}{h} \frac{Q^{\ddagger}_{ZPC}}{Q^{R}_{ZPC}} e^{-\Delta E^{\ddagger}_{ZPC}/k_B T} \tag{3.1}$$

where the barrier ($\Delta E^{\ddagger}_{ZPC}$) was determined using the zero-point vibrational energy correction; Q^{R}_{ZPC} and $Q^{\ddagger}_{ZPC}$ represent the partition functions of the precursor and transition state structures, respectively; and k_B and h denote the Boltzmann and Planck constants, respectively.

Because some elementary reactions in the proposed photocatalytic pathways involve H/proton transfer, the crossover temperature (T_c) was calculated using Eq. (3.2). T_c is the temperature below which the transition states are dominated by quantum mechanical tunneling (Wigner et al., 1932 and 1938).

$$T_c = \frac{h\Omega^{\ddagger}}{2\pi k_B} \tag{3.2}$$

where $\Omega^{\ddagger}$ is the imaginary frequency of the transition structure. In addition, $k^{Q\text{-}vib}$ was corrected using the second-order Wigner correction to estimate the effect of the quantum mechanical tunneling on the reaction rates (Wigner et al., 1932 and 1938). By assuming that tunneling occurs at the top of the energy barrier, the Wigner correction to the rate constant is as follows Eq. (3.3):

$$\kappa^{S\text{-}Wig}(T) = 1 + \frac{1}{24}\left(\frac{h\Omega^{\ddagger}}{k_B T}\right)^2 \tag{3.3}$$

where $\kappa^{S\text{-}Wig}$ is the Wigner transmission coefficient, which is 1 in the classical limit (h = 0). The Wigner corrected rate constant is $k^{S\text{-}Wig}(T) = \kappa^{S\text{-}Wig}(T)\, k^{Q\text{-}vib}(T)$. The thermodynamic

properties of interest were the Gibbs free energies of the reaction ($\Delta G°$ and $\Delta G°^{,\ddagger}$) and the corresponding enthalpies ($\Delta H°$ and ($\Delta H°^{,\ddagger}$) (House et al., 2007).

3.3.4 Hypothesized photocatalytic water splitting pathways

Because previous theoretical studies revealed that the dissociative adsorption dominates for the first two H_2O molecules, and formation of O_2, H_2 and H_2O_2 were of our interest, both two- and four-electron pathways (Xue et al., 2019; Malik et al., 2020) were studied in this work using the $(TiO_2)_2(H_2O)_2$ cluster as a model system. Dissociative adsorption was hypothesized to occur primarily at the Ti centers. Due to the limited information on the elementary reactions involved in the photodecomposition of H_2O on TiO_2 crystals and nanoclusters, those proposed from theoretical results in the gas phase were primarily adopted (Wang et al., 2011; Fang et al., 2013; Chen et al., 2015). These included water adsorption, dehydrogenation, deoxygenation, H_2O_2 formation, and $(TiO_2)_2$ photocatalyst regeneration. A schematic diagram outlining the step-by-step optimization of the nonradiative photochemical pathway is shown in Fig. 3.13.

3.4 Techno-economic and environmental assessment of pilot-scale photocatalytic water splitting

This study presents a preliminary assessment to evaluate the feasibility of production costs and to examine the associated environmental impacts.

3.4.1 Annual hydrogen production

The H_2 evolution rates presented in Table B1-B4 were obtained from experiments conducted under conditions closely resembling real operating scenarios. The effects of methanol (MeOH) solution concentration, light source, and catalyst type were evaluated at an operating temperature of 25 °C over a period of 1 hour. The conversion of H_2 evolution rates from per hour to per day is shown in Table B2. For the daily production calculation, a 24-hour operation is assumed for UVA-LED and LED light sources, as they can be continuously controlled. However, for natural sunlight as a light source, only 7 hours per day (08:00-15:00) are considered, based on the duration during which solar irradiance is sufficiently intense for the process. In Table B3, the

annual H_2 evolution rates are estimated based on the number of operational days per year, which varies depending on the type of light source. For UVA-LED and LED light sources, which can be continuously controlled, 300 operational days per year are assumed. In contrast, for natural sunlight, the production is considered feasible for only 6 months per year, equivalent to approximately 180 days, based on seasonal solar availability in Thailand.

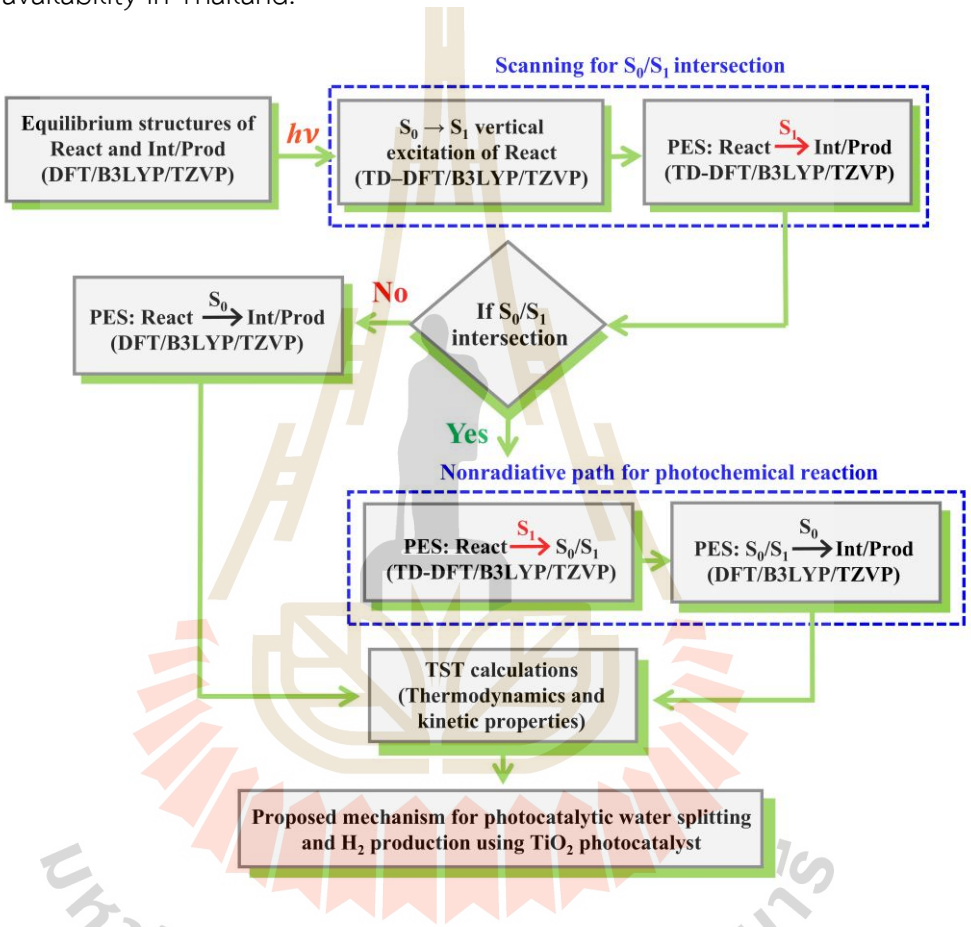

Figure 3.13 Computational strategy and methods used in the study on photocatalytic water splitting and H_2, O_2 and H_2O_2 productions using $(TiO_2)_2$ photocatalyst. React = reactant; Int = intermediate; Prod = product; PES = potential energy surface; S_0/S_1 = S_0 and S_1 state intersection.

3.4.2 Photocatalyst material extraction

Fig. 3.14 presents a flowchart outlining the experimental procedure for synthesizing TiO_2 and 2%Pt/TiO_2 photocatalysts. The process layout, including the required equipment, is illustrated in Fig. 3.15. This synthesis method served as a

reference for developing a production system capable of manufacturing photocatalyst materials on an industrial scale. The sequence of operations forms a critical path in the overall process, with each stage clearly identified along with its time requirement to determine the key steps that influence the efficiency and total duration of production. Table 4.5 summarizes the material and energy requirements for fabricating a single photocatalyst panel at the laboratory scale. Using these values for material consumption and primary energy use, the cumulative energy demand (CED) and greenhouse gas (GHG) emissions were determined.

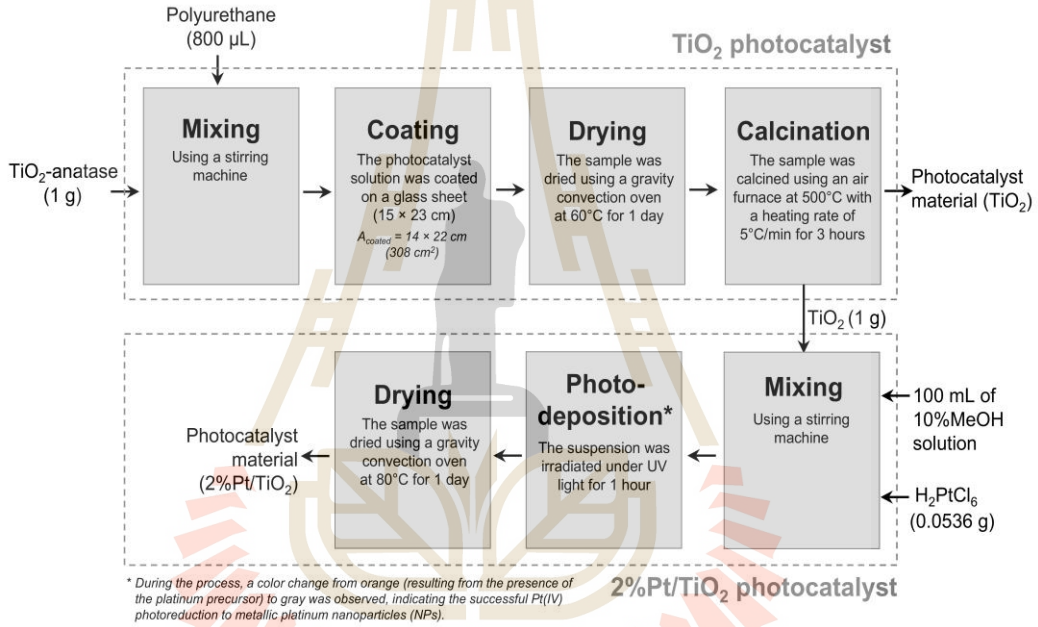

Figure 3.14 Flowchart of the preparation of photocatalyst materials: TiO_2 and 2%Pt/TiO_2 for mass-scale production.

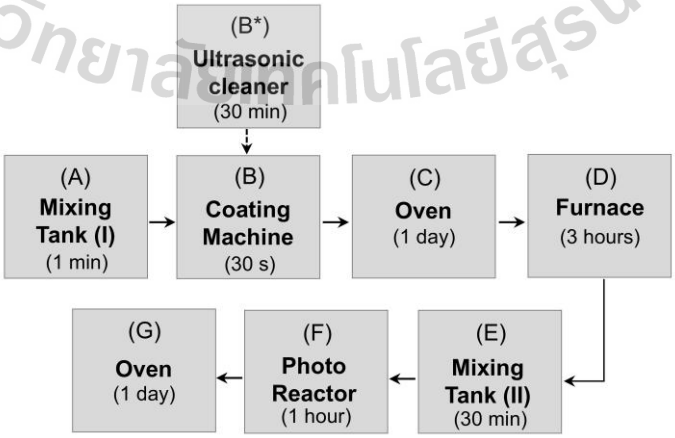

Figure 3.15 Layout of the process design for photocatalyst material preparation.

3.4.3 Equipment sizing

This study considers commercially available equipment for each unit operation within the system. It is observed that power consumption does not scale linearly with equipment capacity. To minimize energy usage, equipment selection is based on the required production volume for the panel-photoreactor area. This selection significantly affects the GHG emissions per kilogram of H_2 produced. A daily production capacity of 3,247 panels (equivalent to 100 m^2) is assumed for the facility. The cycle time of each fabrication step is recorded, and equipment with a capacity equal to or greater than 3,247 panels per day is selected for analysis, as shown in Table 3.3.

Table 3.3 Equipment for process design.

Process: Cleaning of the glass sheet material using an ultrasonic cleaner					
Tank size (mm)	Overall size (mm)	Power (W)	Time (min)	Cost ($/No.)	Reference
600×480×390	1260×980×940	2400	30	4980	Alibaba. Industrial Ultrasonic Cleaners. 2025 [date accessed 25-07-2025]; Available from: https://shorturl.at/CZjOS.
750×550×390	1410×1050×980	3000	30	5600	
1000×550×420	1660×1050×1100	4000	30	6600	
1200×650×490	1860×1150×1180	6000	30	8480	
1450×720×570	2010×1220×1260	8000	30	11400	
1500×800×640	2060×1300×1330	10800	30	13600	
1700×900×640	2260×1400×1330	12000	30	15600	
2500×1200×840	3060×1700×1530	24000	30	24200	
Process: Mixing tanks with agitators for mixing the photocatalyst solution					
Volume (L)	Motor power (W)	Stirring speed (rpm)	Time (min)	Cost ($/No.)	Reference
100	680	40-2990	1	1000	Alibaba. Industrial Machinery, Mixing Equipment. 2025 [date accessed 25-07-2025]; Available from: https://surl.li/lxlfqn.
200	750	40-2990	1	1200	
300	870	40-2990	1	1500	
500	1100	40-2990	1	1800	
1000	1500	40-2990	1	2800	
2000	3000	40-2990	1	5500	
3000	3600	40-2990	1	8200	

Table 3.3 Equipment for process design (continue).

Process: Coating of photocatalyst solution film						
Max. coating dimensions (cm)	Power (W)	Traverse speed (mm/sec)	Coating thickness	Time (sec)	Cost ($/No.)	Reference
43 × 30 (1290 cm^2)	200	0-200	Thinnest film: 1.5 µm	30	1590	Alibaba. Industrial Machinery, Coating Machines. 2025 [date accessed 25-07-2025]; Available from: https://surl.li/kkbnyn.

Process: Calcination of photocatalyst materials				
Power (W)	Volume (L)	Time (h)	Cost ($/No.)	Reference
15000	468	3	12000	(Maurya et al., 2022)
39000	2456	3	48000	
950000	30000	3	250000	
210000	57600	3	400000	

Process: Photodeposition of metal onto photocatalyst materials				
Power (W)	Area (m^2)	Time (h)	Cost ($/No.)	Reference
2500	1	1	34000	Alibaba. Flat-Panel Photochemical Reaction System. 2025 [date accessed 25-07-2025]; Available from: https://surli.cc/omodrq.

Process: Photodeposition of metal onto photocatalyst materials				
Power (W)	Volume (L)	Time (h)	Cost ($/No.)	Reference
15000	3328	24	25000	(Maurya et al., 2022)
18000	4032	24	25650	
20000	18050	24	70000	

CHAPTER IV

RESULTS AND DISCUSSION

4.1 Characterization of photocatalysts

The 2%Pt/TiO_2 photocatalyst was prepared by the photodeposition method. In this process, hexachloroplatinic acid (H_2PtCl_6) was dissolved in 10% v/v aqueous methanol (MeOH), where it dissociates to yield $[PtCl_6]^{2-}$ and protons ($H_2PtCl_6 \rightleftharpoons 2H^+ + [PtCl_6]^{2-}$) (Jiang et al., 2016). Upon UV irradiation, TiO_2 generates photoexcited charge carriers ($TiO_2 + h\nu \rightarrow e^-$ (conduction band (CB)) + h^+ (valence band (VB))). The photogenerated holes (h^+) are consumed by MeOH acting as a sacrificial electron (e^-) donor, producing oxidized intermediates (Jiang et al., 2016; Wenderich et al., 2016). The photogenerated electrons reduce the adsorbed Pt(IV) precursor according to: $[PtCl_6]^{2-} + 4e^- \rightarrow Pt^0 + 6Cl^-$ (Wenderich et al., 2016). Adsorption of $[PtCl_6]^{2-}$ occurs preferentially at surface hydroxyl groups, oxygen vacancies, or Ti^{3+} defect sites of TiO_2, where ligand exchange may replace a chloride ligand with a surface –O–Ti group, forming surface-bound Pt complexes (Yoshida et al., 2016). These surface species are gradually reduced by CB electrons to yield Pt^0 atoms, which nucleate into clusters and finally grow into metallic Pt nanoparticles: Pt^0 (ads) → Pt atom aggregation → small Pt clusters → Pt nanoparticles (Yoshida et al., 2016). Once initial Pt^0 nuclei are formed, the reduction of residual Pt(IV) complexes proceeds autocatalytically on the growing Pt particles, accelerating deposition. The overall particle growth is limited by the concentration of Pt precursor in solution (Yoshida et al., 2016). Anchoring sites such as oxygen vacancies, Ti^{3+} centers, surface hydroxyls, and defect sites concentrate electrons and promote Pt nucleation, resulting in highly dispersed Pt nanoparticles on TiO_2 (Jiang et al., 2016; Kubiak et al., 2024).

Fig. 4.1(a) presents the crystal structure analysis of TiO_2 and 2%Pt/TiO_2 photocatalysts, examined using X-ray diffraction (XRD). The results confirm that the XRD pattern corresponds to the anatase phase of TiO_2, as identified by ICSD No. 98-017-2916 (tetragonal, space group I41/amd (141)). Characteristic diffraction peaks were

observed at 2θ values of 25.3°, 36.9°, 37.8°, 38.6°, 48.0°, 53.9°, 55.0°, 62.7°, 68.8°, 70.3°, and 75.0°, which are associated with the crystalline planes (011), (103), (004), (112), (020), (015), (121), (024), (116), (220), and (125), respectively. In the case of 2%Pt/TiO_2, no detectable diffraction signals from Pt species were observed. This absence may be attributed to the low Pt concentration (~2.5% as follow in Fig. 4.2(d)) on the TiO_2-anatase surface or the high dispersion of Pt species, which prevents the formation of periodic structures. The average crystallite size of TiO_2 anatase was determined using the Scherrer equation: $D = K\lambda/\beta cos\theta$ where D represents the average crystallite size (nm), K is the Scherrer constant (0.68 for spherical crystallites, as depicted in Fig. 4.2(a)-(b)), λ is the X-ray wavelength (Cu-Kα = 1.5406 Å), β denotes the line broadening at full width at half maximum (FWHM) in radians, and θ is the Bragg angle in degrees (half of 2θ) (Rayes-Gasga et al., 2015). The analysis revealed that the mean crystallite size of TiO_2 particles was 6.63 nm, with only a slight reduction to 6.29 nm after Pt loading.

Fig. 4.1(b) presents the UV-vis absorption spectra of the photocatalysts. Pure TiO_2 exhibits a distinct absorption edge at approximately 386 nm, characteristic of its anatase phase. Upon incorporating Pt into TiO_2, the absorption edge gradually shifts toward the visible region, which can be attributed to the visible light absorption by highly dispersed Pt species around 400 nm. As shown in Fig. 4.1(c), the band gap of the 2%Pt/TiO_2 photocatalyst (3.1 eV) is lower than the 3.2 eV value observed for pure TiO_2. This variation in binding energy for 2%Pt/TiO_2 may result from changes in Pt particle dispersion or alterations in their oxidation state.

The average particle size of TiO_2 is 85.42 nm (Fig. 4.2(a(I)-(II))), while for 2%Pt/TiO_2, it is 86.65 nm (Fig. 4.2(b(I)-(II))). The corresponding film thicknesses are 22.33 μm (Fig. 4.2(a(III))) and 25.46 μm (Fig. 4.2(b(III))), respectively. The addition of 2%Pt does not significantly alter the surface characteristics, so the specific surface area analysis focuses only on TiO_2-anatase. Fig. 4.1(d) shows the adsorption isotherm of TiO_2. BET analysis indicates a specific surface area of 13.42 m^2/g, a pore volume of 0.0261 cm^3/g, and an average pore size of 3.51 nm.

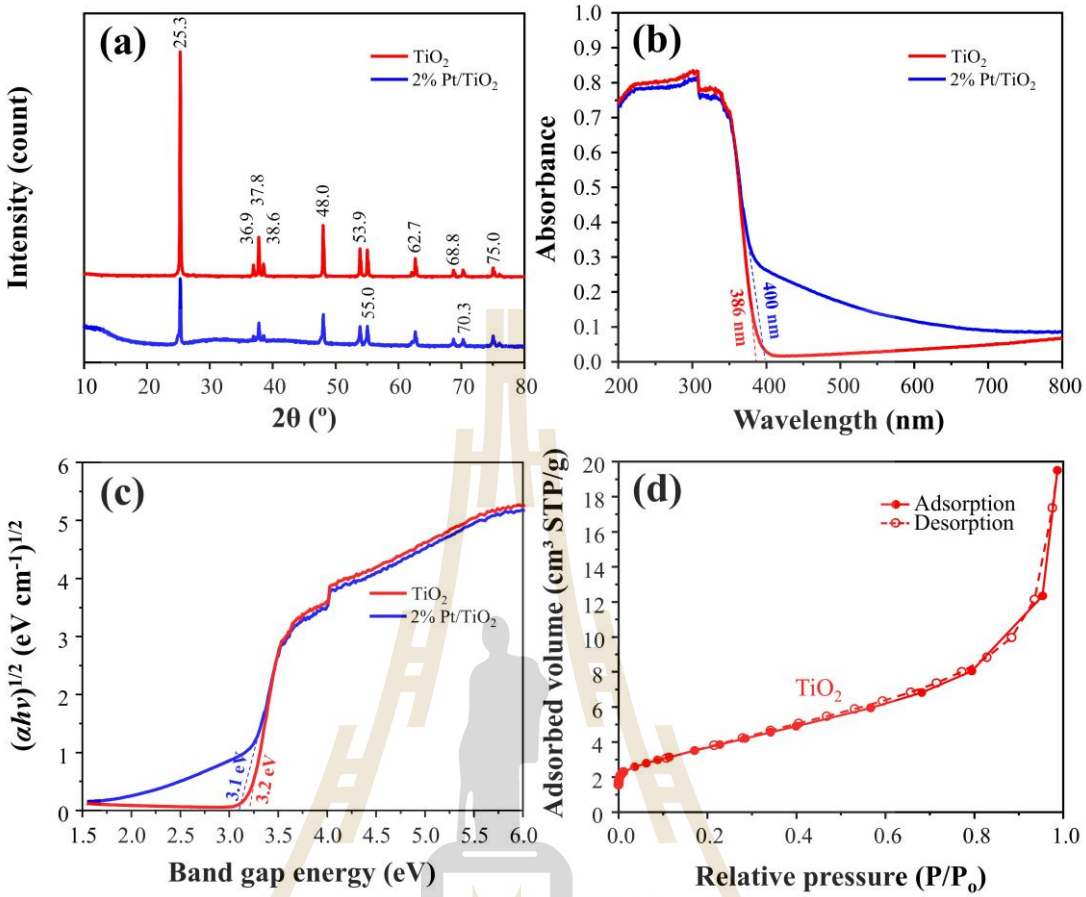

Figure 4.1 The characterization of the TiO_2 and 2%Pt/TiO_2 photocatalysts includes: (a) XRD patterns for crystal structure analysis, (b) UV-Vis spectroscopy for optical properties, (c) band gap energy determination using the Tauc method, and (d) adsorption isotherm of TiO_2.

4.2 The performance of photocatalytic water splitting in a panel photoreactor

The effect of temperature on photocatalytic water splitting using a TiO_2 photocatalyst under UVA light without a sacrificial reagent (MeOH) is shown in Fig. 4.3. When the UVA light source is turned on, the system's temperature increases by approximately ~1.5 °C, even under controlled conditions. The results indicate that as the temperature rises, the rate of H_2 evolution decreases.

Although photocatalytic water splitting is an endothermic reaction, and H_2 evolution would typically increase with rising temperature (Zhou et al., 2023), this

system exhibits more complex behavior. In a panel photoreactor, light passes through the quartz window (98%) and excites the TiO_2 photocatalyst, generating electron (e^-) and hole (h^+) pairs. According to photocatalytic principles, these charge carriers must participate in redox reactions before recombining. During this process, photooxidation generates O_2, while photoreduction produces H_2 (Fujishima et al., 1971 and 1972; Hwang et al., 2022).

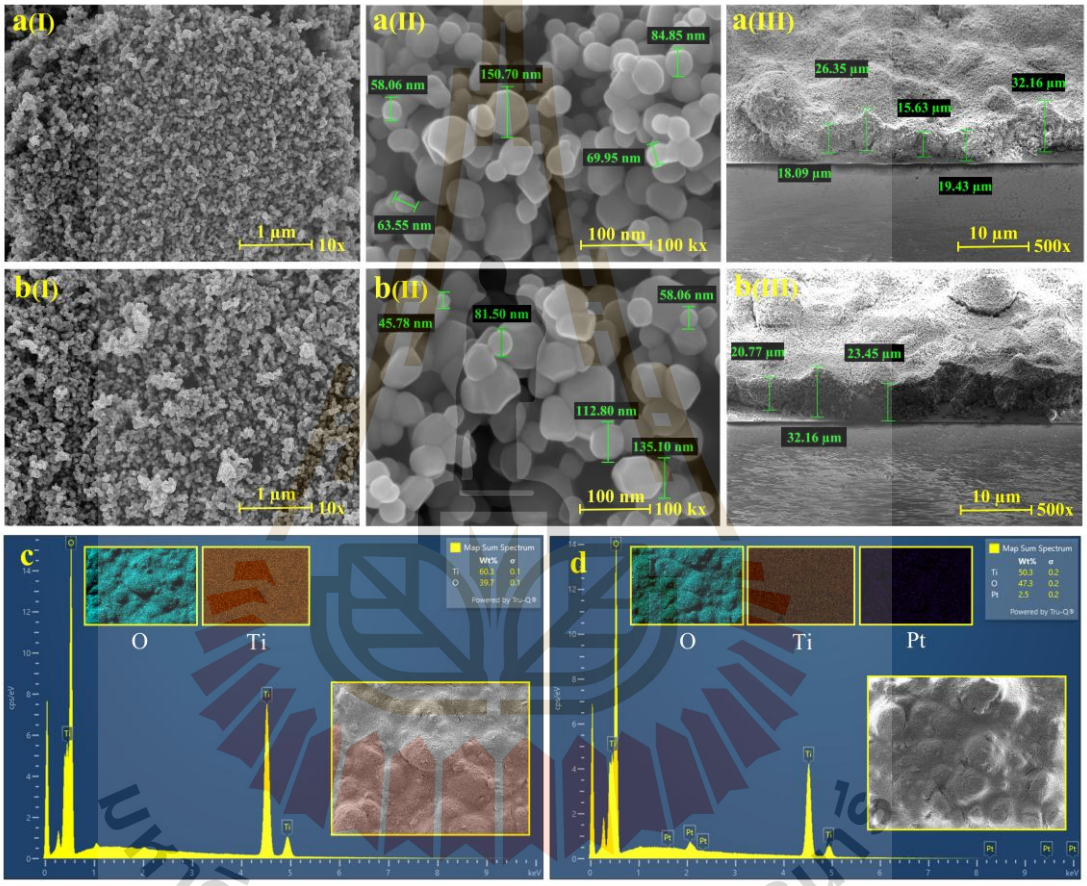

Figure 4.2 The morphology analysis was performed using the FESEM/EDS technique to investigate the photocatalyst materials. FESEM was used to observe the surface morphology of (a) TiO_2 and (b) 2%Pt/TiO_2. The FESEM images provide information on (I) the photocatalyst surface structure, (II) the particle size distribution, and (III) the photocatalyst layer coated on a glass sheet. EDS was used for atomic mapping to analyze the elemental distribution in (c) TiO_2 and (d) 2%Pt/TiO_2.

At lower reaction temperatures (13 and 25 °C), the activity of TiO_2 increases with temperature. However, at higher temperatures (40-70 °C), the H_2 evolution efficiency decreases. Similar studies have reported that an increase in temperature can reduce the photocatalytic water-splitting efficiency using single-particulate CrO_x/Rh/$SrTiO_3$: Ir, Sb, Al photocatalysts co-loaded with CoOOH under visible light irradiation (Kikuchi et al., 2025). In this study, increasing the reaction temperature from approximately 7 °C (280 K) to 67 °C (340 K) significantly decreased the photocatalytic activity. This decline was attributed to both the irreversible degradation of the CoOOH cocatalyst, due to detachment or aggregation, and the increased recombination of photogenerated carriers, as evidenced by the reduced photoluminescence of Eu^{3+} in the $SrTiO_3$ host. In contrast, the CrO_x/Rh cocatalyst remained stable, and reverse reactions of H_2 and O_2 were not enhanced. These results indicate that the decrease in photocatalytic performance at elevated temperatures is dominated by these negative factors rather than by any positive effect from accelerated surface reactions (Kikuchi et al., 2025). Other research also suggests that temperature primarily affects quantum phenomena, particularly electron-hole separation and recombination (Chen et al., 2021). In this system, 25 °C is considered optimal for efficient photocatalytic water splitting in a panel photoreactor operating continuously.

Photocatalytic water splitting using pure water and a TiO_2-anatase photocatalyst demonstrated that, although the panel photoreactor confirmed the effectiveness of our design for H_2 production, the H_2 production rate remained very low (0.51 μmol g^{-1} min^{-1}), as shown in Fig. 4.3. To improve H_2 production, the panel photoreactor was further tested using TiO_2 and 2%Pt/TiO_2 photocatalysts with MeOH as a sacrificial reagent at various concentrations, under a reaction temperature of 25 °C. The results are shown in Fig. 4.4(a)-(b).

According to Fig. 4.4(a), when using TiO_2 with MeOH, the H_2 evolution increased to 5.89, 11.48, 43.82, and 144.88 μmol g^{-1} min^{-1} at MeOH concentrations of 2%, 4%, 6%, and 8%, respectively. As shown in Table 4.1, when comparing the batch and continuous photoreactors, the continuous photoreactor exhibited better performance than the batch system (Pala et al., 2021). This improvement can be attributed to the continuous removal of products from the reaction zone. Therefore, the continuous

photoreactor demonstrated superior performance in H_2 evolution compared to the batch photoreactor

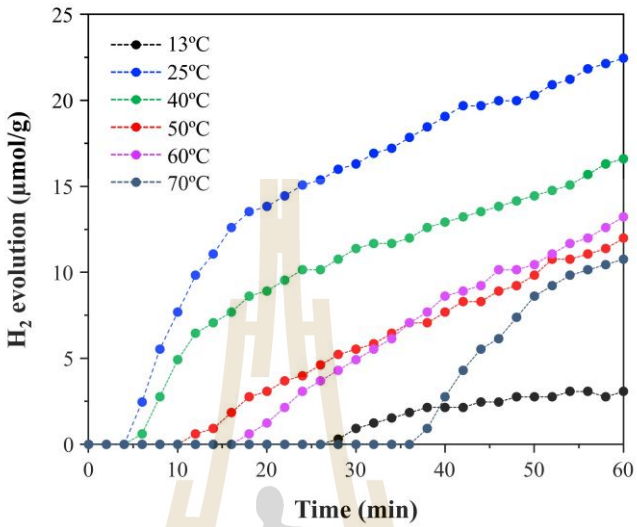

Figure 4.3 Photocatalytic water splitting for H_2 evolution using a TiO_2-anatase photocatalyst without a sacrificial reagent (MeOH) at different reaction temperatures.

The photocatalytic water splitting process begins with the excitation of TiO_2 under light irradiation, following the reaction ($TiO_2 + h\nu \rightarrow TiO_2$ (e^- (CB), h^+ (VB))). In this process, hydroxyl radicals ($^{\bullet}OH$) and superoxide radicals ($O_2^{\bullet-}$) are the main reactive species responsible for oxidation. Once these radicals are formed, they initiate the decomposition of MeOH through radical reactions on the TiO_2 surface (Lin et al., 2009). The effect of MeOH concentration on H_2 production using TiO_2 under UVA light is illustrated in Fig. 4.4(a). As the MeOH concentration increases, H_2 production also rises. This is because higher MeOH concentrations lead to more MeOH molecules being adsorbed onto the photocatalyst surface, which promotes further reaction. To support the decomposition of this additional MeOH, a higher amount of reactive species ($^{\bullet}OH$ and $O_2^{\bullet-}$) would ideally be needed. However, since the light intensity, irradiation time, and photocatalyst dosage are kept constant, the production of these reactive species does not increase accordingly. As a result, as shown in Fig. 4.4(f), when the MeOH concentration exceeds 10%, the rate of H_2 production begins to slow down, forming a

gradual curve, which indicates the system is approaching its reaction limit under the given conditions.

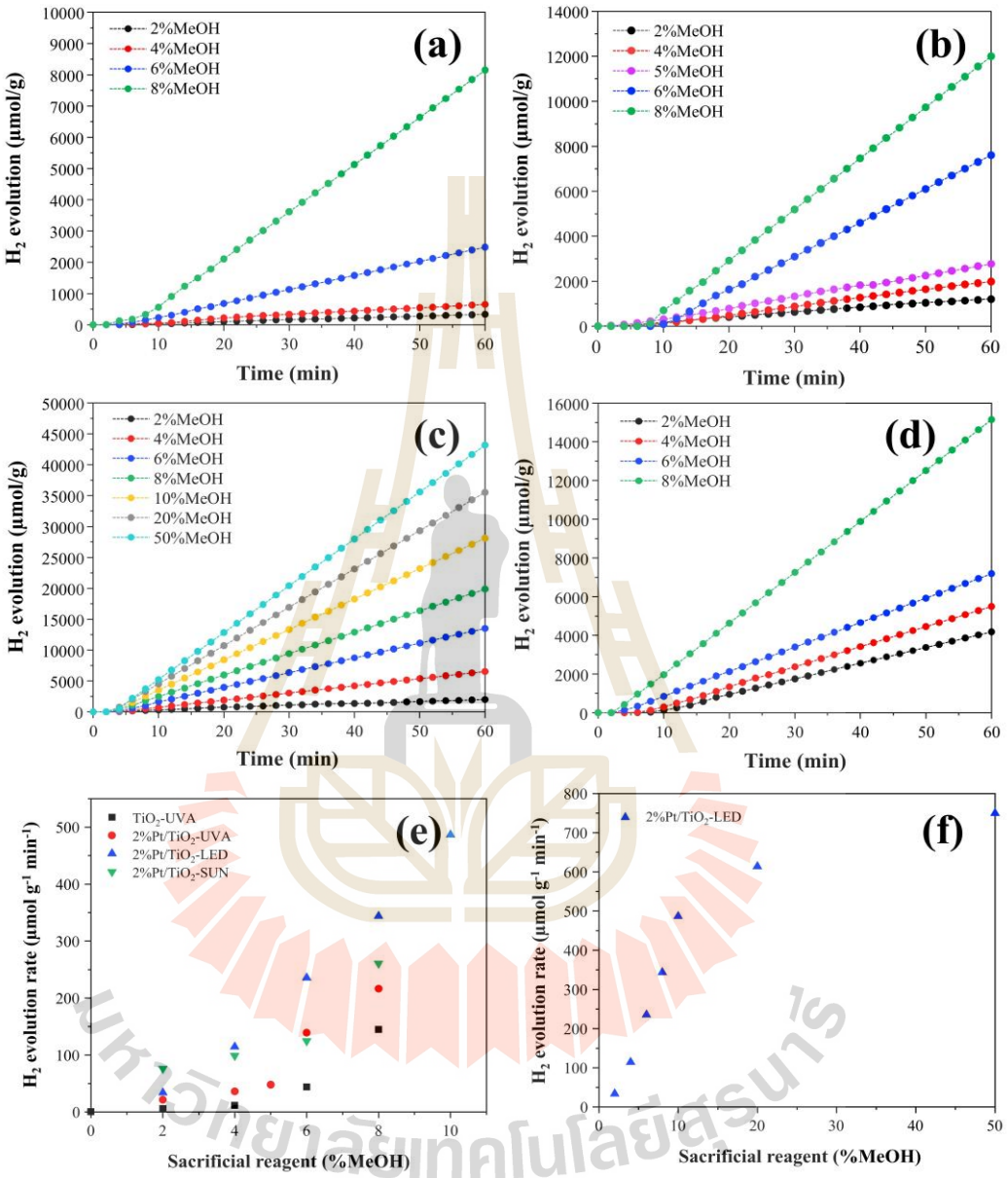

Figure 4.4 Plots of H_2 evolution versus time: (a) TiO_2 under UVA-LED, (b) 2%Pt/TiO_2 under UVA-LED, (c) 2%Pt/TiO_2 under LED, and (d) 2%Pt/TiO_2 under natural sunlight. All experiments were conducted using MeOH as a sacrificial reagent at different concentrations. (e) Comparison of photocatalyst types and light sources at different concentrations of sacrificial reagent (MeOH), and (f) H_2 evolution as a function of sacrificial reagent concentration for 2%Pt/TiO_2 under LED light source.

Table 4.1 Comparison of photocatalytic water spitting for H_2 evolution.

Catalysts	Sacrificial reagent	Light source (nm)	H_2 evolution rate (μmol g^{-1} min^{-1})	Process types	References
TiO_2	-	365-400	0.51	Continuous	This work
TiO_2	-	254	0.0019	Batch	(Chen et al., 2011)
TiO_2	8%MeOH	365-400	144.88	Continuous	This work
TiO_2 (P25)	10%MeOH	352	0.2000	Batch	(Afrin et al., 2025)
2%Pt/TiO_2	8%MeOH	365-400	216.40	Continuous	This work
2%Pt/TiO_2	10%MeOH	350-2000	8.17	Batch	This work
1%Pt/TiO_2	10%MeOH	352	51.95	Batch	(Afrin et al., 2025)
1%Pt/TiO_2	10%MeOH	365	290.00	Batch	(Al-Azri et al., 2015)
1%Pd/TiO_2	10%MeOH	365	521.67	Batch	(Al-Azri et al., 2015)
1%Au/TiO_2	10%MeOH	365	293.33	Batch	(Al-Azri et al., 2015)
2%Pt/TiO_2	20%MeOH	400-700	614.12	Continuous	This work
2%Pt/TiO_2	20%EtOH	420-780	9.70	Batch	(Zhang et al., 2014)
2%Pt/TiO_2	8%MeOH	400-700	343.87	Continuous	This work
1%Pt/TiO_2	20%MeOH	350-2000	272.50	Continuous	(Pala et al., 2021)
2%Pt/TiO_2	8%MeOH	Natural sun light	260.71	Continuous	This work
1%Pt/TiO_2	20%MeOH	350-2000	12.77	Continuous	(Pala et al., 2021)
0.5%Pt-1%Au/TiO_2	33%MeOH	> 400	21.25	Batch	(Melvin et al., 2015)
1%Pt/TiO_2	33%MeOH	> 400	-	Batch	(Melvin et al., 2015)
TiO_2 (P25)	33%MeOH	> 400	-	Batch	(Melvin et al., 2015)

In Fig. 4.4(b), the TiO_2 photocatalyst was modified with 2%Pt loading (confirmed as approximately 2.5% by FESEM/EDS analysis in Fig. 4.2(d)). H_2 production increased significantly with rising MeOH concentration, similar to the trend observed in Fig. 4.4(a). However, when compared to TiO_2 without Pt loading, the H_2 evolution using 2%Pt/TiO_2 was higher of 3.62, 3.15, 3.17, and 1.49 times at MeOH concentrations of 2%, 4%, 6%, and 8%, respectively. The low activity of TiO_2 in photocatalytic water splitting without Pt is mainly due to its high overpotential for H_2 production and the rapid reverse reaction, where H_2 and O_2 recombine to form water (Yu et al., 2010). Typically,

depositing noble metals such as Pt on the surface of a semiconductor significantly improves the separation of photogenerated electrons (e^-) and holes (h^+), extends their lifetimes, and suppresses the reverse reaction between O_2 and H_2. These effects ultimately enhance the photocatalytic activity (Yu et al., 2010). As a result, in the photocatalytic water splitting system using Pt-loaded TiO_2 with MeOH, a high H_2 production rate was achieved, reaching 21.32, 36.14, 47.91, 139.08, and 216.40 μmol g^{-1} min^{-1} at MeOH concentrations of 2%, 4%, 5%, 6%, and 8%, respectively.

From Fig. 4.4(b)-(d), the 2%Pt/TiO_2 photocatalysts demonstrated stable performance across all MeOH concentrations under three different light sources: UVA-LED (Fig. 4.4(b)), LED (Fig. 4.4(c)), and natural sunlight (Fig. 4.4(d)). This stability is confirmed by the linear H_2 evolution observed over the 1-hour reaction period, indicating consistent photocatalytic activity. The introduction of Pt onto the TiO_2 surface reduced the energy band gap from 3.2 eV to 3.1 eV (Fig. 4.1(c)), allowing the 2%Pt/TiO_2 photocatalyst to utilize visible light more effectively.

In this work, we designed a panel photoreactor using a commercial TiO_2-based photocatalyst. Despite its simplicity, this prototype successfully produced H_2 under UVA-LED, LED, and natural sunlight, highlighting its potential for practical applications. To evaluate the feasibility of scaling up the system, we compared the performance of different light sources, considering their potential for commercial use. As shown in Fig. 4.4(e), the highest H_2 production was achieved under LED irradiation for all MeOH concentrations. Further analysis of the light sources wavelength distributions is provided in Fig. 4.6, with UVA-LED shown in Fig. 3.5(a), LED in Fig. 3.5(b), and natural sunlight in Fig. 3.5(c). The panel photoreactor was equipped with a quartz window, allowing approximately 98% light transmittance (LED and natural sunlight), and 90% for UVA-LED, which ensured efficient light penetration into the reaction zone. Under 10% MeOH concentration, the H_2 evolution rates were 486.94, 258.25, and 333.82 μmol g^{-1} min^{-1} for LED, UVA-LED, and natural sunlight, respectively. Additionally, during operation, the system temperature increased due to infrared (near IR) irradiation, rising by approximately 1.5 °C, 3 °C, and 5 °C under UVA-LED, LED, and natural sunlight, respectively. Finally, as shown in Table 4.1, we compared our system with previous studies, most of which used batch photoreactors and similar types of photocatalysts.

The results suggest that photoreactor design plays a key role in enhancing photocatalytic efficiency. Therefore, to scale up from lab-scale to large-scale H_2 production, it is crucial to develop systems that closely mimic industrial conditions and maximize the utilization of available light sources.

4.3 Exploring photocatalytic water splitting pathways for efficient hydrogen production: A theoretical investigation

In this study, Roman numerals in square bracket ($[...]^{eq}$) are used to discuss the equilibrium structures of molecules, whereas a capital English letter and a number in square bracket, e.g., [B1] and [A1], are used to label the structures on the PESs in ε = 80 and 1, respectively. In addition, [...] and $[...]^*$ are the structures on the S_0 and S_1 PESs, respectively; $[...]^{‡}$ and $[...]^{§}$ are the transition structure (‡) and S_0/S_1 intersection structure (§), respectively; ΔE^{Ex} is $S_0 \rightarrow S_1$ vertical excitation energy; $\Delta E^{§}$ is the energy difference at the S_0/S_1 intersection (§), and $\Delta E^{‡}$ is the energy barrier.

4.3.1 Photocatalytic pathway optimizations

Analysis of the refined PESs in ε = 80 results in the potential energy profiles, as shown in Figs. 4.7 and 4.8. These potential energy profiles indicate that pathways with low or no energy barriers can be accessed through a series of photoexcitation events. It appeared that to generate O_2, H_2, and H_2O_2 in ε = 80, the photocatalytic water splitting cycle involves three consecutive and three parallel elementary reactions on $(TiO_2)_2$. H_2 can be generated through irradiations at λ^{abs} = 279 and 911 nm, whereas O_2 and H_2O_2 can be generated at λ^{abs} = 458 and 381 nm, respectively. The three consecutive elementary reactions are water adsorption [Eq. (4.1)], dehydrogenation **(I)** [Eqs. (4.2) and (4.3)], and deoxygenation [Eq. (4.4)], whereas the three parallel elementary reactions that regenerate the $(TiO_2)_2$ photocatalyst, producing H_2O_2 and the second H_2, include H_2O_2 formation and dehydrogenation **(IIa)** and **(IIb)** [Eqs. (4.5)-(4.7), respectively].

Water adsorption:

$$\mathbf{[I]}^{eq,S0} \xrightarrow{h\nu} \mathbf{[I]}^{*} \rightarrow \mathbf{[I]}^{eq,S1} \rightarrow \mathbf{[B1]}^{§} \xrightarrow{S_1/S_0} \mathbf{[II]}^{eq,S0} \quad (4.1)$$

Dehydrogenation **(I)**:

$$[II]^{eq,S0} \xrightarrow{h\nu} [II]^{*} \rightarrow [B2]^{\S} \xrightarrow{S_1/S_0} [III]^{eq,S0} \quad (4.2)$$

$$[III]^{eq,S0} \xrightarrow{h\nu} [III]^{*} \rightarrow [B3]^{\S} \xrightarrow{S_1/S_0} [IV]^{eq,S0} \rightarrow H_2 \quad (4.3)$$

Deoxygenation:

$$[V]^{eq,S0} \xrightarrow{h\nu} [V]^{*} \rightarrow [V]^{eq,S1} \rightarrow [VI]^{eq,S1} \rightarrow [B4]^{\S} \xrightarrow{S_1/S_0} [VI]^{eq,S0} \rightarrow O_2 \quad (4.4)$$

H_2O_2 formation, Dehydrogenation **(IIa)** and **(IIb)**:

$$[VI]^{eq,S0} \xrightarrow{h\nu} [VI]^{*} \rightarrow [B5]^{\S} \xrightarrow{S_1/S_0} [VII]^{eq,S0} \rightarrow H_2O_2 \quad (4.5)$$

$$[VI]^{eq,S0} \xrightarrow{h\nu} {}^{a}[VI]^{*} \rightarrow {}^{a}[B5]^{\S} \xrightarrow{S_1/S_0} {}^{a}[VII]^{eq,S0} \rightarrow H_2 \rightarrow (TiO_2)_2 \quad (4.6)$$

$$[VI]^{eq,S0} \xrightarrow{-O_2} {}^{a}[VI]^{eq,S0} \rightarrow {}^{b}[B7]^{eq,S0} \rightarrow {}^{a}[VII]^{eq,S0} \rightarrow H_2 \rightarrow (TiO_2)_2 \quad (4.7)$$

Because photocatalytic water splitting experiments were generally conducted in the aqueous solution, the results in ε = 80 are mainly discussed, whereas those in ε = 1 are included in the supplementary section (e.g., Figs. A1 and A2).

4.3.1.1 Consecutive reactions

The analysis of the characteristic structures in the S_0 state, obtained using DFT/B3LYP/TZVP optimizations (Table 4.2), suggests that structure **[I]^{eq,S0}** is the equilibrium structure of the $(TiO_2)_2(H_2O)_2$ cluster [water adsorption in Eq. (4.1)] with the Ti–O distances, R_{Ti-O} = 1.87 and 1.66 Å. The Ti–O distances are in excellent agreement with those obtained using the DFT/B3LYP/DZVP2 method, R_{Ti-O} = 1.86 and 1.64 Å (Wang et al., 2011). The $S_0 \rightarrow S_1$ vertical excitation energy of structure **[I]^{eq,S0}** [ΔE^{Ex} = 4.44 eV (λ^{abs} = 279 nm)] is also in reasonable agreement with the principal absorption wavelengths of TiO_2 nanoparticles obtained in UV-vis experiment (λ^{abs} = 250-330 nm) (Rathod et al., 2015).

As shown in the potential energy profiles in Fig. 4.5(a), after the $S_0 \rightarrow S_1$ vertical excitation (λ^{abs} = 279 nm), structure **[I]*** barrierlessly relaxes to the equilibrium structure in the S_1 state (**[I]^{eq,S1}**) and further relaxes to the structure at the S_0/S_1 intersection (structure **[B1]§** with $\Delta E^{\S}$ = 0.34 kJ/mol). This is followed by the $S_1 \rightarrow S_0$ internal conversion to structure **[II]^{eq,S0}** [Eq. (4)], which becomes the precursor for dehydrogenation **(I)** [Eq. (4.2)]. Structure **[II]^{eq,S0}** can be considered as a photo-

dissociative product of the adsorbed $(H_2O)_2$ on the $(TiO_2)_2$ photocatalyst, which has no energy barrier in this case.

As shown in Fig. 4.5(b), for dehydrogenation **(I)** [Eqs. (4.2) and (4.3)], two photons with comparable energies are required to generate the first H_2 molecule product, by sequential $S_0 \rightarrow S_1$ vertical excitations of structures $\mathbf{[II]}^{eq,S0}$ [ΔE^{Ex} = 4.55 eV (λ^{abs} = 272 nm)] and $\mathbf{[III]}^{eq,S0}$ [ΔE^{Ex} = 4.44 eV (λ^{abs} = 279 nm)]. With structure $\mathbf{[III]}^{eq,S0}$ acting as the intermediate and $\mathbf{[IV]}^{eq,S0}$ as the product [Eq. (4.3)], the successive photoexcitation occurs across low-energy barriers in the S_1 state, with $\Delta E^{\ddagger}$ values of 24 and 32 kJ/mol, respectively. Meanwhile, structures $\mathbf{[B2]}^{\S}$ and $[\mathbf{B3}]^{\S}$ at the S_0/S_1 intersection possess $\Delta E^{\S}$ values of 0.34 and 3.03 kJ/mol, respectively. Structure $\mathbf{[IV]}^{eq,S0}$ is characterized by a peroxide (O–O) linkage and two O–H bonds with R_{O-O} = 1.47 and R_{Ti-OH} = 1.80 Å. The covalent bond distance in H_2 is R_{H-H} = 0.76 Å, with the Van der Waals binding energy ΔE^{VdW} = −17.8 kJ/mol; R_{H-H} is in good agreement with the experimental value, with R_{H-H} = 0.74 Å (Huber et al., 1979).

After dehydrogenation **(I)**, the first H_2 molecule product can be easily removed from structure $\mathbf{[IV]}^{eq,S0}$, resulting in structure $\mathbf{[V]}^{eq,S0}$. As shown in the potential energy profile in Fig. 4.5(c), deoxygenation (Eq. 4.4) could proceed from the $S_0 \rightarrow S_1$ vertical excitation of structure $\mathbf{[V]}^{eq,S0}$ in the visible region [ΔE^{Ex} = 2.71 eV (λ^{abs} = 458 nm)], followed by the barrierless energy relaxation of structure $\mathbf{[V]}^{*}$ to the S_0/S_1 intersection (structure $\mathbf{[B4]}^{\S}$ with $\Delta E^{\S}$ = 1.24 kJ/mol). The $\mathbf{[V]}^{*} \rightarrow \mathbf{[B4]}^{\S}$ structural relaxation is accomplished via the O–H isomerization in the S_1 state, followed by the formation of a strong peroxide linkage (the O_2 molecule) after the $S_1 \rightarrow S_0$ relaxation in structure $\mathbf{[VI]}^{eq,S0}$ with R_{O-O} and ΔE^{VdW} of 1.44 Å and −540 kJ/mol, respectively. The O–O covalent bond in the adsorbed O_2 molecule is slightly longer than that in the free O_2 molecule, with an R_{O-O} = 1.21 Å (Huber et al., 1979).

4.3.1.2 Parallel reactions

After deoxygenation, two structures were considered for the $(TiO_2)_2$ regeneration, namely, structure $\mathbf{[VI]}^{eq,S0}$ or $^{a}\mathbf{[VI]}^{eq,S0}$ acting as the precursors. Structure $^{a}\mathbf{[VI]}^{eq,S0}$ was generated by removing the O_2 molecule from structure $\mathbf{[VI]}^{eq,S0}$. The potential energy profiles obtained from the DFT and TD-DFT/B3LYP/TZVP and NEB methods in Fig. 4.6 indicate that for the $(TiO_2)_2$ regeneration, three parallel reactions,

namely, H_2O_2 formation, dehydrogenation **(IIa)**, and dehydrogenation **(IIb)** [Eqs. (4.5)-(4.7)], could be hypothesized after deoxygenation (Eq. 4.4).

The analysis of Fig. 4.6(a) reveals that while the oxidations of H_2O to generate H_2O_2 on the TiO_2 surfaces [rutile (110), anatase (101), and brookite (210)] in Ref. (Malik et al., 2020) involve moderate-energy barriers ($\Delta E^{\ddagger}$ = 19-60 kJ/mol (Malik et al., 2020), obtained based on the DFT/PBE plain wave method), the $S_0 \rightarrow S_1$ vertical excitation of structure **[VI]**^{eq,S0} [the O_2 molecule adsorbed onto $(TiO_2)_2(OH)_2$] in the UVA range [ΔE^{Ex} = 3.25 eV (λ^{abs} = 381 nm)] could barrierlessly lead to the adsorption of H_2O_2 onto $(TiO_2)_2$ in structure **[VII]**^{eq,S0} with the O–O covalent bond distance (R_{O-O}) of 1.45 Å. This R_{O-O} value is in excellent agreement with the experimental value (R_{O-O} = 1.48 Å) (Redington et al., 1962), and the O–H...O–H bond with R_{O-HO} = 2.76 Å is responsible for the H_2O_2 adsorbed on $(TiO_2)_2$, with $\Delta E^{H\text{-bond}}$ = −92 kJ/mol [Eq. (4.5)].

As illustrated by the potential energy profiles in Figs. 4.6(b) and 4.6(c), the production of the second H_2 molecule and regeneration of $(TiO_2)_2$ could proceed in both S_1 and S_0 states, i.e., dehydrogenation **(IIa)** and dehydrogenation **(IIb)** [Eqs. (4.6) and (4.7), respectively]. As shown in Fig. 4.6(b), for dehydrogenation **(IIa)**, the $S_0 \rightarrow S_1$ vertical excitation of structure ^{a}**[VI]**^{eq,S0} in the near-IR range [ΔE^{Ex} = 1.36 eV (λ^{abs} = 911 nm)] can generate an H_2 molecule without an energy barrier, ΔE^{VdW} = −28 kJ/mol.

By contrast, in the S_0 state, dehydrogenation **(IIb)** in ε = 80 proceeds through two consecutive reactions with moderate-energy barriers (Fig. 4.6(c)), with $\Delta E^{\ddagger}$ values of 158 and 132 kJ/mol, respectively. These energy barriers are associated with an H transfer from one O–H group to one of the Ti atoms, followed by the formation the second H_2 molecule, with structure ^{b}**[B7]**^{eq,S0} as the intermediate. Structure ^{b}**[B7]**^{eq,S0} is characterized by a Ti–H bond with R_{Ti-H} = 1.71 Å, which is comparable with the reported values of R_{Ti-H} = 1.69-1.72 Å (Fang et al., 2013). However, our energy barriers are significantly lower than those reported for the first and second H transfers to the Ti atom, which were obtained based on the DFT/B3LYP/DZVP2 method to be $\Delta E^{\ddagger}$ = 460 and 586 kJ/mol, respectively (Fang et al., 2013).

Remarks should be made on the parallel elementary reactions in Eqs. (4.5)-(4.7). Because the O_2 molecule could be strongly adsorbed onto $(TiO)_2(OH)_2$

via a peroxide linkage [structure **[VI]**^{eq,S0} in Fig. 4.5(c)], the regeneration of $(TiO_2)_2$ via structure ^{a}**[VI]**^{eq,S0} [dehydrogenation **(IIa)** and dehydrogenation **(IIb)** in Eqs. (4.6) and (4.7), respectively] could be less favorable than through H_2O_2 production [Eq. (4.5)]. This issue will be addressed in the dynamic analysis. Based on the above PES analysis, holistic elementary reaction networks for photocatalytic water splitting and production of H_2, O_2, and H_2O_2 are summarized in Fig. 4.7.

4.3.2 Kinetic and thermodynamic properties

Kinetic and thermodynamic properties of the rate-determining elementary reactions are thoroughly analyzed and discussed to identify the optimal conditions for photocatalytic water splitting. Results in Figs. 4.5 and 4.6 suggested barrierless energies for almost all the proposed elementary reactions; therefore, the discussion is focused on dehydrogenation **(IIb)**. On the S_0 PESs, the second H_2 molecule production and regeneration of $(TiO_2)_2$ in ε = 80 involve $\Delta E^{\ddagger}$ = 158 and 132 kJ/mol. Two thermodynamic models were hypothesized in Fig. 4.8 to study the effect of the photo-to-thermal energy transformation in dehydrogenation **(IIb)**. Model **(a)** is characterized by dehydrogenation **(IIb)** occurring in an isolated system. Alternatively, for Model **(b)** (a photo-to-thermal energy transformation model), dehydrogenation **(IIb)** and deoxygenation (the preceding step) are treated as two interconnected closed systems within an isolated system. The thermodynamic results in ε = 80 are presented in Table 4.3, and the detailed analysis is shown in Fig. 4.9.

The thermodynamic results in Table 4.3(a) indicate that for the ^{a}**[VI]**^{eq,S0}$\rightarrow$^{b}**[B7]**^{eq,S0} reaction, the Gibbs free energy barrier ($\Delta G^{o,\ddagger}$) for the formation of the ^{b}**[B6]**‡ transition state is highly positive, whereas $\Delta G^{o,Tot}$ for the formation of the ^{b}**[B7]**^{eq,S0} intermediate is slightly negative, for example, at 296 K, $\Delta G^{o,\ddagger}$ = 152 and $\Delta G^{o,Tot}$ = −45 kJ/mol. The plot of $\Delta G^{o,Tot}$ as a function of the local temperature (red line [a] in Fig. 4.19(a) shows that the ^{a}**[VI]**^{eq,S0}$\rightarrow$^{b}**[B7]**^{eq,S0} reaction is thermodynamically favorable (spontaneous, $\Delta G^{o,Tot} < 0$) at all temperatures and that the thermodynamic spontaneity slightly increases ($\Delta G^{o,Tot}$ more negative) at higher temperatures, whereas the endothermic ^{b}**[B7]**^{eq,S0}$\rightarrow$^{a}**[VII]**^{eq,S0} reaction is not spontaneous at the same temperature, with $\Delta G^{o,Tot}$ value of 49 kJ/mol, as presented in Table 4.3(b). The plot of $\Delta G^{o,Tot}$ as a function of the local temperature (green line [b] in Fig. 4.9(a)) suggests that

this reaction could be thermodynamically favorable, i.e., $\Delta G^{o,Tot} \leq 0$ above T_s = 1600 K, where T_s is spontaneous temperature above which $\Delta G^{o,Tot}$ are negative.

Table 4.2 Equilibrium structures of the $(TiO_2)_2(H_2O)_2$ precursor and characteristic structures of the chemical species on the S_0 and S_1 PESs, obtained from the DFT, TD-DFT/B3LYP/TZVP and NEB methods in aqueous solution (ε = 80). The symbols used are explained in the text. E^{Tot} = total energy in au; ΔE^{Ex} = $S_0 \rightarrow S_1$ vertical excitation energy in eV; (...) = excitation wavelength in nm; $\Delta E^{\S}$ = energy difference at the S_0/S_1 intersection (§) in kJ/mol.

Labels	Structures	E^{Tot}	ΔE^{Ex}	ΔE^{VdW} [$\Delta E^{H\text{-}bond}$]	Labels	Structures	E^{Tot}	$\Delta E^{\S}$
$[I]^{eq,S0}$	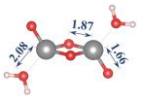	-2152.94326	4.44 (279)	-269.95	$[I]^{eq,S1}$	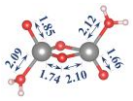	-2152.80281	–
$[II]^{eq,S0}$	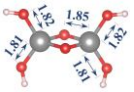	-2152.98685	4.55 (272)	–	$[V]^{eq,S1}$	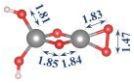	-2151.52628	–
$[III]^{eq,S0}$	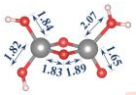	-2152.96694	4.44 (279)	–	$[VI]^{eq,S1}$	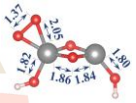	-2151.55562	–
$[IV]^{eq,S0}$	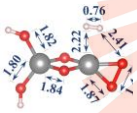	-2152.80970	–	-17.80	$[B1]^{\S}$	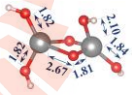	-2152.81013	0.34
$[V]^{eq,S0}$	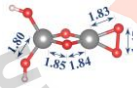	-2151.62845	2.71 (458)	–	$[B2]^{\S}$	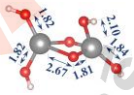	-2152.81013	0.34
$[VI]^{eq,S0}$	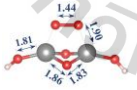	-2151.62383	3.25 (381)	-539.92	$[B3]^{\S}$	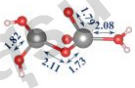	-2152.79166	3.03
$[VII]^{eq,S0}$	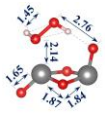	-2151.56240	–	[-91.60]	$[B4]^{\S}$	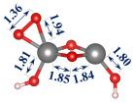	-2151.55547	1.24
$^{a}[VI]^{eq,S0}$		-2001.15676	1.36 (911)	–	$[B5]^{\S}$	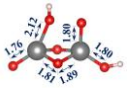	-2151.52839	0.40
$^{a}[VII]^{eq,S0}$	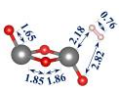	-2001.15447	–	-27.61	$^{a}[B5]^{\S}$	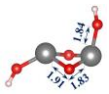	-2001.10628	0.38

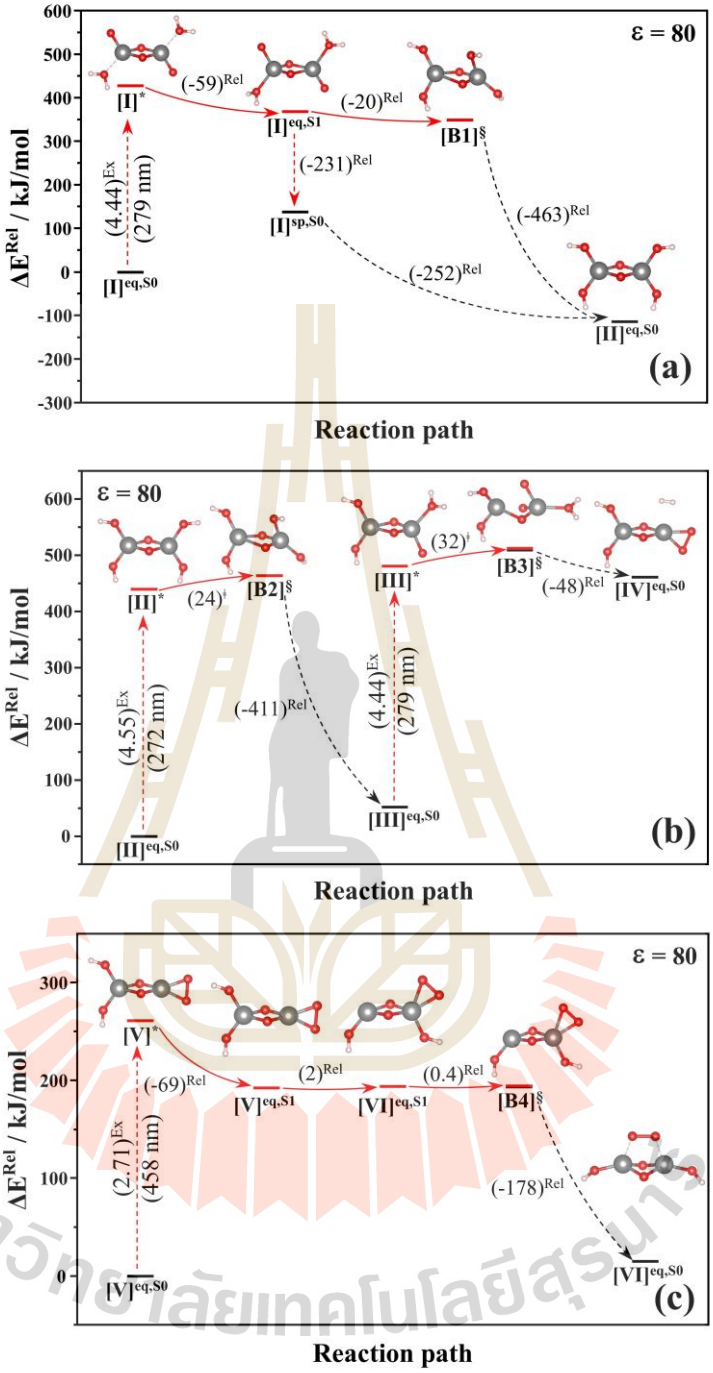

Figure 4.5 Consecutive elementary reactions involving multiple $S_0 \rightarrow S_1$ photoexcitations, $S_1 \rightarrow S_0$ internal conversion at the S_0/S_1 intersection and relaxation in the S_0 state (ε = 80). (a) Photodissociation of the adsorbed $(H_2O)_2$ on $(TiO_2)_2$, (b) Dehydrogenation **(I)**, and (c) Deoxygenation. The symbols are explained in the text. $(...)^{Ex}$ = vertical excitation energy in eV; $(...)^{Rel}$ = relaxation energy in kJ/mol; $(...)^{‡}$ = energy barrier in kJ/mol.

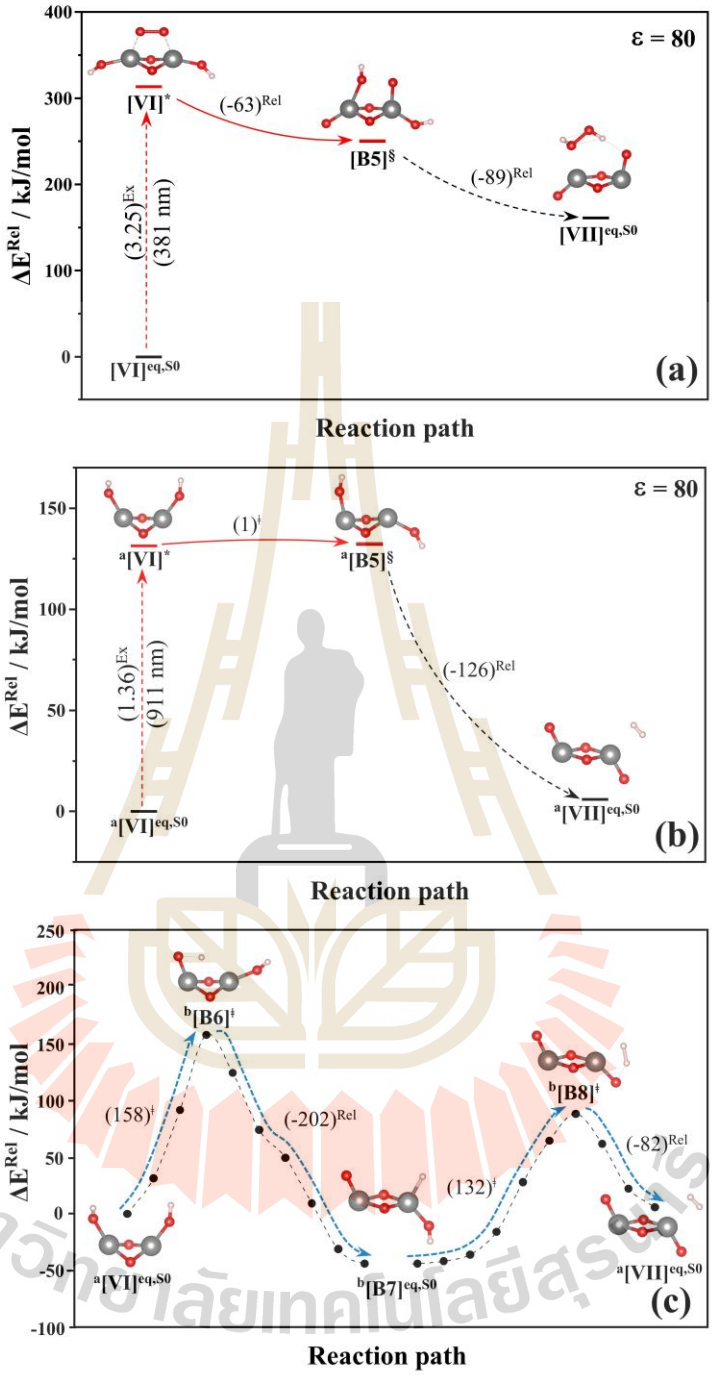

Figure 4.6 Parallel elementary reactions to regenerate the $(TiO_2)_2$ photocatalyst and H_2O_2, O_2 and H_2 productions (ε = 80). (a) H_2O_2 formation from the photoexcitation of the O_2 absorbed on $(TiO_2)_2$, (b) Dehydrogenation **(IIa)** in the S_1 state, proceeding after the O_2 molecule removed from the surface, and (c) Dehydrogenation **(IIb)** in the S_0 state, proceeding after the O_2 molecule removed from the surface.

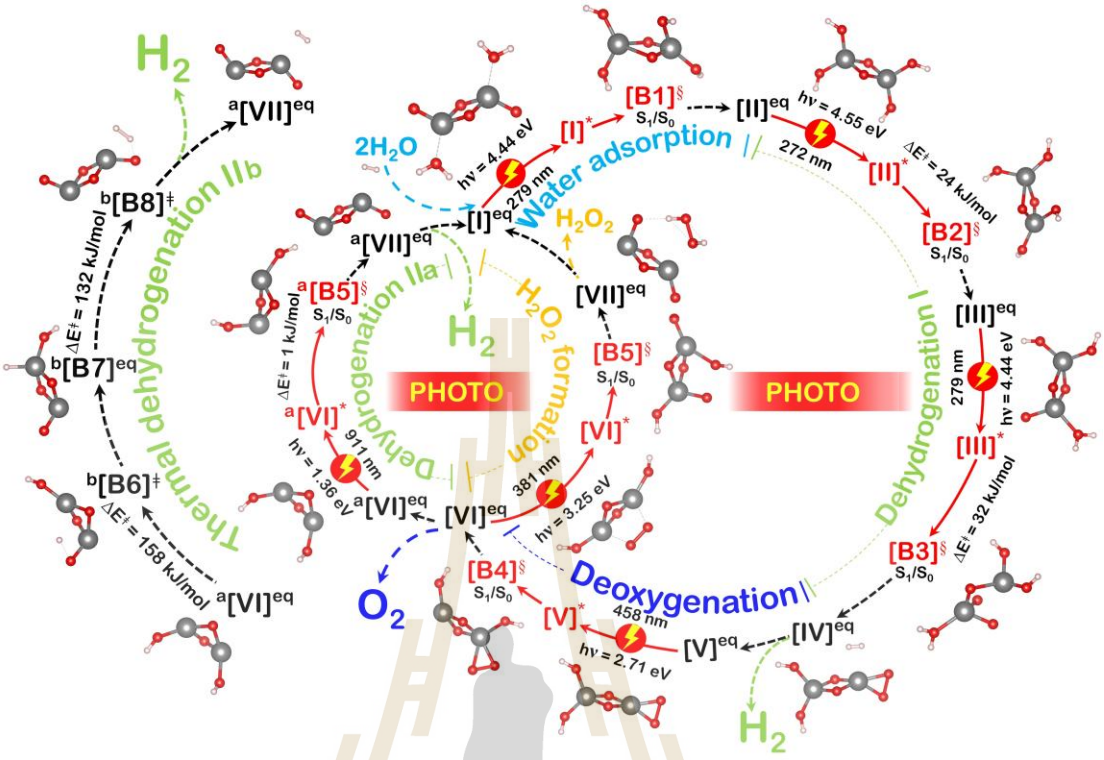

Figure 4.7 Holistic elementary reaction networks for photocatalytic water splitting and H_2, O_2 and H_2O_2 productions using $(TiO_2)_2$ photocatalyst (ε = 80), obtained from the analysis of the potential energy profiles in Figs. 4.5 and 4.6. The symbols are explained in the text.

Based on the assumption that all the heat released from $^{a}[VI]^{eq,S0} \rightarrow {}^{b}[B7]^{eq,S0}$ directly transfers to the $^{b}[B7]^{eq,S0} \rightarrow {}^{a}[VII]^{eq,S0}$ reaction, the spontaneous temperature of the $^{a}[VI]^{eq,S0} \rightarrow {}^{a}[VII]^{eq,S0}$ reaction is reduced to T_s = 500 K (black line [c] in Fig. 4.9(a)). Therefore, for Model **(a)**, the effective thermodynamic condition for dehydrogenation **(IIb)** is T ≥ 500 K. For Model **(b)**, assuming that all the $S_1 \rightarrow S_0$ relaxation energies released from the preceding step (deoxygenation), $[V]^{*} \rightarrow [VI]^{eq,S0}$ in Eq. (4.4), directly transfer to dehydrogenation **(IIb)**, the reaction becomes thermodynamically highly favorable at all temperatures (Table 4.3(c) and blue line [d] in Fig. 4.9(a)).

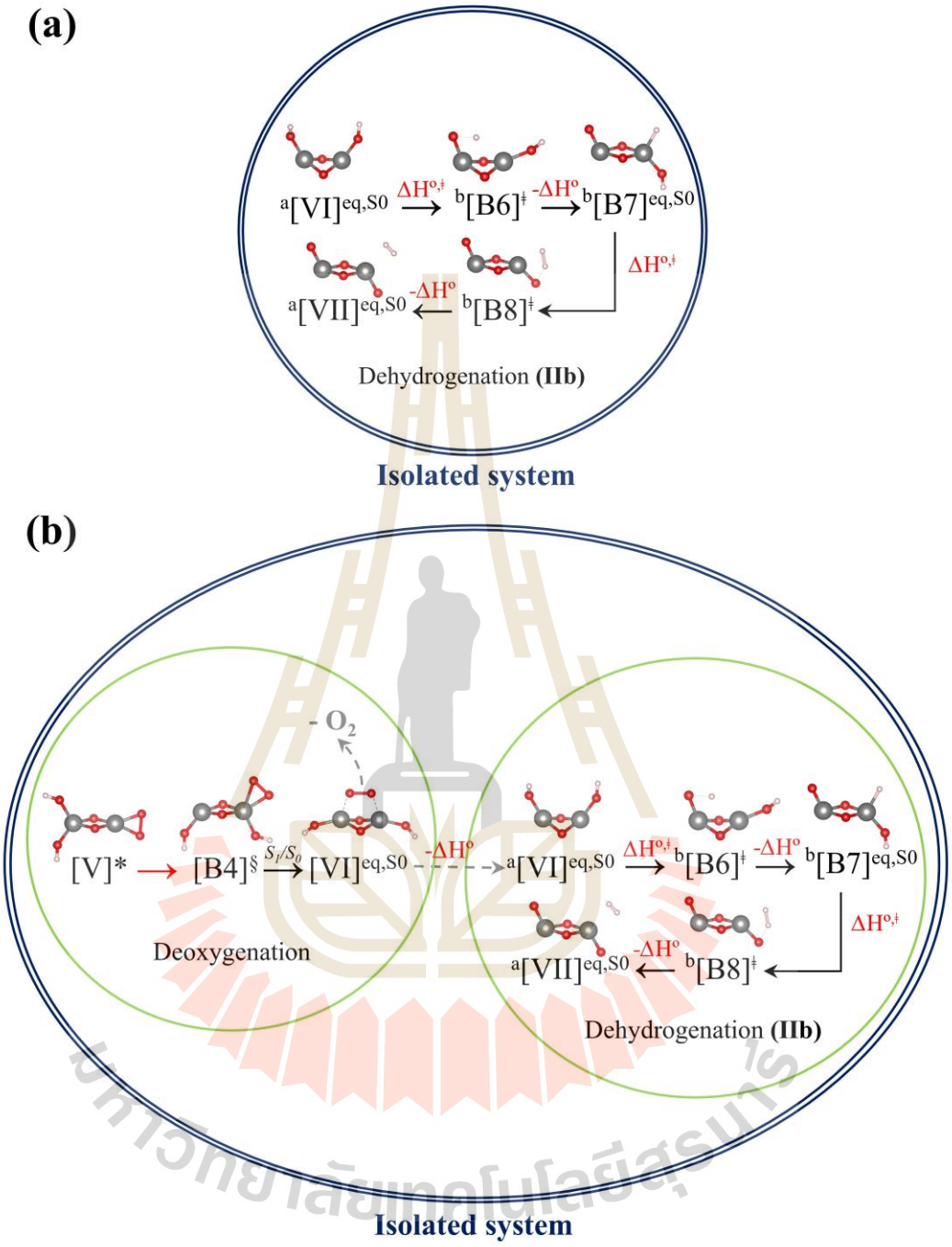

Figure 4.8 The heat transfer models used in the study on the production of the second H_2 molecule and $(TiO_2)_2$ regeneration [Eq. (4.7)]. (a) Model **(a)**: Dehydrogenation **(IIb)** as an isolated system. (b) Model **(b)**: Deoxygenation [Eq. (4.4)] and Dehydrogenation **(IIb)** as two close systems within an isolated system (photo-to-thermal energy conversion).

Table 4.3 Thermodynamic properties of the exothermic and endothermic elementary reactions in ε = 80. (a) The O_2 production [deoxygenation in [Eq. (4.4)]. (b)-(c) Formation of the **^{b}[B7]^{eq,S0}** intermediate and second H_2 production and $(TiO_2)_2$ regeneration [dehydrogenation **(IIb)** in Eq. (4.7)]. (d) Formation of **^{b}[B6]‡** and **^{a}[VII]^{eq,S0}** from **[V]*** in Model **(b)** in Fig. 4.8(b).

(a)	^{a}[VI]^{eq,S0} ⟶ ^{b}[B6]‡			^{b}[B6]‡ ⟶ ^{b}[B7]^{eq,S0}			^{a}[VI]^{eq,S0} ⟶ ^{b}[B7]^{eq,S0}		
T	$\Delta H^{o,‡}$	$\Delta S^{o,‡}$	$\Delta G^{o,‡}$	ΔH^{o}	ΔS^{o}	ΔG^{o}	$\Delta H^{o,Tot}$	$\Delta S^{o,Tot}$	$\Delta G^{o,Tot}$
280	150.9	-1.2	152.1	-197.7	-0.5	-197.3	-46.8	-1.7	-45.2
296	150.9	-1.3	152.2	-197.7	-0.3	-197.3	-46.8	-1.7	-45.1
333	150.9	-1.5	152.4	-197.5	-0.1	-197.3	-46.6	-1.6	-45.0
380	151.0	-1.6	152.6	-197.2	0.2	-197.4	-46.2	-1.4	-44.8
609	152.1	-1.3	153.4	-195.6	2.7	-198.3	-43.5	1.4	-44.9
900	154.8	1.2	153.6	-193.3	7.2	-200.5	-38.6	8.3	-46.9
1066	156.6	3.3	153.3	-192.0	10.2	-202.2	-35.4	13.5	-48.9
2382	171.2	28.5	142.7	-181.3	40.8	-222.1	-10.1	69.3	-79.4
(b)	^{b}[B7]^{eq,S0} ⟶ ^{b}[B8]‡			^{b}[B8]‡ ⟶ ^{a}[VII]^{eq,S0}			^{b}[B7]^{eq,S0} ⟶ ^{a}[VII]^{eq,S0}		
T	$\Delta H^{o,‡}$	$\Delta S^{o,‡}$	$\Delta G^{o,‡}$	ΔH^{o}	ΔS^{o}	ΔG^{o}	$\Delta H^{o,Tot}$	$\Delta S^{o,Tot}$	$\Delta G^{o,Tot}$
280	132.7	2.0	130.8	-81.7	-79.2	2.6	53.6	4.6	49.0
296	132.8	2.2	130.6	-81.9	-79.0	2.9	53.8	5.1	48.8
333	133.0	2.7	130.3	-82.3	-78.6	3.6	54.4	6.3	48.1
380	133.3	3.4	129.8	-82.8	-78.1	4.7	55.2	8.1	47.1
609	135.4	8.4	127.0	-86.1	-76.1	10.0	59.3	18.4	40.9
900	139.7	17.9	121.8	-91.0	-75.0	16.0	64.6	33.9	30.8
1066	142.5	24.4	118.1	-94.0	-74.9	19.0	67.6	43.5	24.1
2382	166.7	91.6	75.1	-116.3	-76.9	39.4	89.8	131.0	-41.2
(c)	[V]* ⟶ [B4]§			[B4]§ ⟶ [VI]^{eq,S0}			[V]* ⟶ [VI]^{eq,S0}		
T	ΔH^{o}	ΔS^{o}	ΔG^{o}	ΔH^{o}	ΔS^{o}	ΔG^{o}	$\Delta H^{o,Tot}$	$\Delta S^{o,Tot}$	$\Delta G^{o,Tot}$
280	-70.8	3.1	-73.8	-178.2	-0.7	-177.5	-248.9	2.4	-251.4
296	-70.8	3.1	-73.9	-178.2	-0.8	-177.4	-249.0	2.4	-251.4
333	-70.9	3.3	-74.1	-178.2	-1.0	-177.2	-249.1	2.3	-251.4
380	-71.0	3.3	-74.4	-178.2	-1.2	-177.0	-249.2	2.1	-251.3
609	-72.4	2.4	-74.7	-178.1	-2.6	-175.5	-250.5	-0.2	-250.3
900	-74.5	-0.8	-73.8	-178.0	-4.5	-173.5	-252.5	-5.3	-247.3
1066	-75.9	-3.2	-72.7	-177.9	-5.7	-172.2	-253.8	-8.9	-244.9
2382	-86.8	-31.8	-54.9	-178.0	-17.6	-160.4	-264.7	-49.4	-215.3

(d)	[V]* ⟶ ^{b}[B6]‡			[V]* ⟶ ^{a}[VII]^{eq,S0}		
T	$\Delta H^{o,‡}$	$\Delta S^{o,‡}$	$\Delta G^{o,‡}$	$\Delta H^{o,Tot}$	$\Delta S^{o,Tot}$	$\Delta G^{o,Tot}$
280	-98.0	1.2	-99.3	-242.1	5.3	-247.6
296	-98.1	1.1	-99.2	-242.0	5.8	-247.7
333	-98.2	0.8	-99.0	-241.3	7.0	-248.3
380	-98.2	0.5	-98.7	-240.2	8.8	-249.0
609	-98.4	-1.5	-96.9	-234.7	19.6	-254.3
900	-97.7	-4.1	-93.7	-226.5	36.9	-263.4
1066	-97.2	-5.6	-91.6	-221.6	48.1	-269.7
2382	-93.5	-20.9	-72.6	-185.0	150.9	-335.9

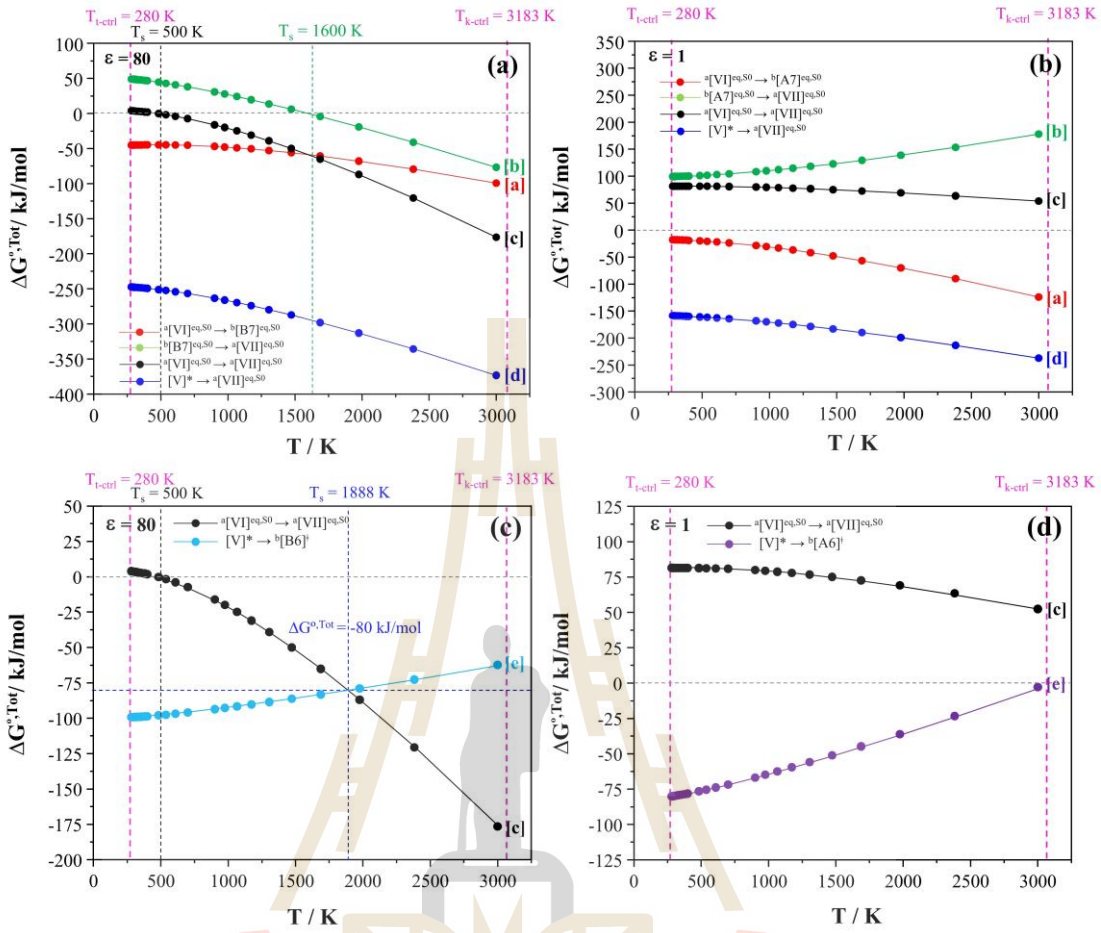

Figure 4.9 (a)-(b) Plots of the total Gibbs free energy ($\Delta G^{o,Tot}$) as a function of local temperature (T) for the elementary reactions in deoxygenation, dehydrogenation **(IIb)** and regeneration of $(TiO_2)_2$, in **ε** = 80 and 1, respectively. (c) Plots of the total Gibbs free energy ($\Delta G^{o,Tot}$) as a function of local temperature (T) for the **[V]*⟶^{b}[B6]‡** ([e]) and **^{a}[VI]^{eq,S0}⟶^{a}[VII]$^{eq,S0}** ([c]) reactions in the S_0 state and in **ε** = 80. (d) Plot of the total Gibbs free energy ($\Delta G^{o,Tot}$) for the **[V]*⟶^{b}[A6]‡** ([e]) and **^{a}[VI]^{eq,S0}⟶^{a}[VII]$^{eq,S0}** ([c]) reactions in the S_0 state and in **ε** = 1.

Alternatively, because formation of the **^{b}[B6]‡** transition structure precedes the formation of the second H_2 molecule product in the S_0 state, the **[V]*⟶^{b}[B6]‡** reaction could be both thermodynamically and kinetically important elementary steps in dehydrogenation **(IIb)** (Fig. 4.6(c)). Therefore, the thermodynamic spontaneity of the **[V]*⟶^{b}[B6]‡** reaction was additionally studied. The plot of $\Delta G^{o,Tot}$

versus the local temperatures (Table 4.3(d) and cyan line [e] in Fig. 4.9(c)) demonstrates that in ε = 80, the thermodynamic spontaneity of this reaction is temperature dependent. In particular, as temperature decreases, the thermodynamic spontaneity increases, with an asymptotic value, $\Delta G^{o,Tot} \approx -100$ kJ/mol for T ≤ 280 K. Therefore, T = 280 K could be considered as the "thermodynamically controlled temperature" ($T_{t\text{-}ctrl}$) for the $\mathbf{[V]^{*} \rightarrow {}^{b}[B6]^{\ddagger}}$ reaction.

The trend of $\Delta G^{o,Tot}$ contrasts with that of the $\mathbf{{}^{a}[VI]^{eq,S0} \rightarrow {}^{a}[VII]^{eq,S0}}$ reaction, where decreasing temperature leads to reduced thermodynamic spontaneity [black line [c] in Fig. 4.9(c)]. An analysis of the kinetic data presented in Table 4.4 reveals that at low temperatures (e.g., T = 280 K), the $\mathbf{{}^{a}[VI]^{eq,S0} \rightarrow {}^{b}[B6]^{\ddagger}}$ reaction is kinetically unfavorable due to a high Gibbs free energy barrier ($\Delta G_f^{\ddagger}$ = 153 kJ/mol), with extremely low rate constants ($k_f^{Q\text{-}vib}$ = 2.02 × 10^{-16} and $k_f^{S\text{-}Wig}$ = 7.35 × 10^{-16} s^{-1}). Therefore, the "kinetically controlled temperature" ($T_{k\text{-}ctrl}$) for Model **(b)** must be estimated to balance the thermodynamic and kinetic factors for the $\mathbf{[V]^{*} \rightarrow {}^{b}[B6]^{\ddagger}}$ and $\mathbf{{}^{a}[VI]^{eq,S0} \rightarrow {}^{a}[VII]^{eq,S0}}$ reactions.

In this study, the average $S_1 \rightarrow S_0$ relaxation temperature (T_{S0}^{Av}) in the photo-to-thermal energy transformation reaction [deoxygenation, $\mathbf{[V]^{*} \rightarrow [VI]^{eq,S0}}$, in Eq. (4.4)] was evaluated by performing nonadiabatic microcanonical molecular dynamics simulations with surface-hopping dynamics (NVE-MDSH) (Suwannakham et al., 2024), for which several initial configurations were generated using the Wigner distribution. NVE-MDSH simulations were subsequently performed over a period of ~4 ps using the TURBOMOLE 7.80 software package. An example NVE-MDSH result in Fig. 4.10 reveals that for the photo-to-thermal energy transfer in Model **(b)**, the average local temperature (kinetic energy, KE) in the S_1 state, T_{S1}^{Av} = 2343 K ± 844 K (KE = 235 ± 85 kJ/mol) and that in the S_0 state, T_{S0}^{Av} = 3183 K ± 1041 K (KE = 321 ± 105 kJ/mol), with an extremely short $S_1 \rightarrow S_0$ relaxation time ($\tau_{S1 \rightarrow S0}$) of 151 fs. Moreover, at this high temperature (T_{S0}^{Av}), the adsorbed O_2 molecule on the $(TiO_2)_2$ photocatalyst can be easily desorbed (Fig. 4.10).

Assuming the concentration of the reaction "hot spots" in Model **(b)** is ~10^{-2} M and $q_{H2O} = ms_{H2O}\Delta T$, the temperature of the aqueous solution surrounding the hot spots is expected based on the NVE-MDSH results in Fig. 4.10 to increase by a

maximum of only ~1 K. As shown in Fig. 4.9(c), the plots of $\Delta G^{o,Tot}$ for the $\mathbf{[V]^{*}\rightarrow {}^{b}[B6]^{\ddagger}}$ and $\mathbf{{}^{a}[VI]^{eq,S0}\rightarrow {}^{a}[VII]^{eq,S0}}$ reactions versus the local temperature, together with the kinetically ($T_{k\text{-}ctrl} = T_{S0}^{Av} \approx 3183$ K) and thermodynamically controlled temperatures ($T_{t\text{-}ctrl} \approx 280$ K), suggest that the ideal local temperature could be at T = 1888 K with $\Delta G^{o,Tot} \approx -80$ kJ/mol to balance the thermodynamic and kinetic factors. Moreover, at this temperature, the rate constants for the $\mathbf{{}^{a}[VI]^{eq,S0}\rightarrow {}^{b}[B6]^{\ddagger}}$ reaction are $k_f^{Q\text{-}vib} = 4.83 \times 10^{7}$ and $k_f^{S\text{-}Wig} = 5.11 \times 10^{7}$ s^{-1}.

Remarks should be made on the rate constants calculated using the TST method. The results presented in Table 4.4 show that the crossover temperature (T_c) is high because $\mathbf{{}^{a}[VI]^{eq,S0}\rightarrow {}^{b}[B7]^{eq,S0}}$ and $\mathbf{{}^{b}[B7]^{eq,S0}\rightarrow {}^{a}[VI]^{eq,S0}}$ involve an H/proton transfer. Therefore, the effect of the quantum mechanical tunneling could be important at low temperatures, $k_f^{S\text{-}Wig} >> k_f^{Q\text{-}vib}$, e.g., for $\mathbf{{}^{b}[B7]^{eq,S0}\rightarrow {}^{b}[B8]^{\ddagger}}$ at 280 K, $k_f^{S\text{-}Wig} = 3.03 \times 10^{-15}$ and $k_f^{Q\text{-}vib} = 8.26 \times 10^{-16}$ s^{-1}.

The results for $\varepsilon = 1$ differ significantly from those observed for $\varepsilon = 80$. Although the formation of the intermediate via the $\mathbf{{}^{a}[VI]^{eq,S0}\rightarrow {}^{b}[A7]^{eq,S0}}$ reaction is exothermic (Table A2[†]), due to strong endothermicity in the $\mathbf{{}^{b}[A7]^{eq,S0}\rightarrow {}^{a}[VII]^{eq,S0}}$ reaction, the thermal energy transfer within Model **(a)** (an isolated system) is not sufficient to make $\mathbf{{}^{a}[VI]^{eq,S0}\rightarrow {}^{a}[VII]^{eq,S0}}$ thermodynamically favorable over a reasonable local temperature range (e.g., T = 298-3000 K). The plot of $\Delta G^{o,Tot}$ as a function of the local temperature in Fig. 4.9(b) suggests that without the $S_1 \rightarrow S_0$ relaxation energy released from deoxygenation ($\mathbf{[V]^{*}\rightarrow {}^{a}[VI]^{eq,S0}}$), the production of the second H_2 molecule and regeneration of $(TiO_2)_2$ in Eq. (4.7) cannot be spontaneous (black line [c] in Fig. 4.9(b)). Most importantly, because $\Delta G^{o,Tot}$ for the $\mathbf{{}^{a}[VI]^{eq,S0}\rightarrow {}^{a}[VII]^{eq,S0}}$ and $\mathbf{[V]^{*}\rightarrow {}^{b}[A6]^{\ddagger}}$ reactions does not intersect in Fig. 4.9(d), the thermodynamic and kinetic factors cannot be balanced over the temperature range T = 298-3000 K.

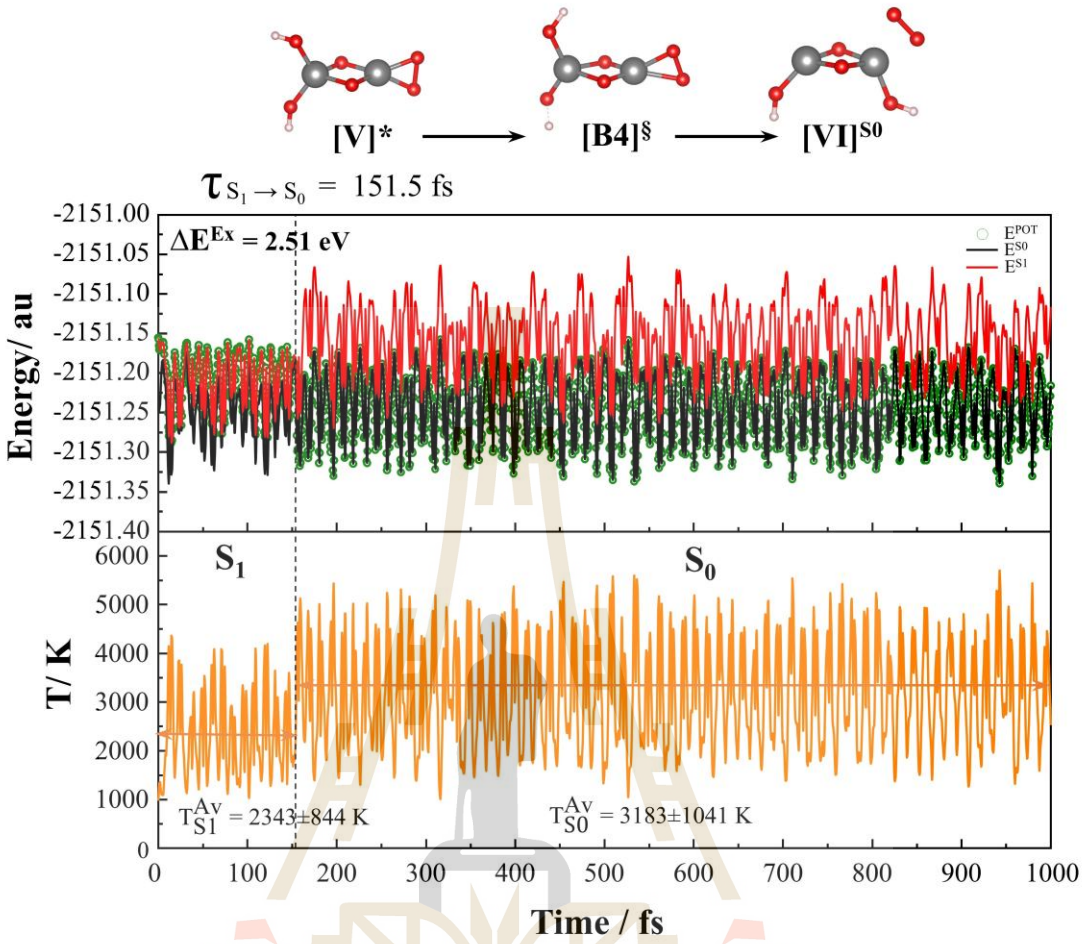

Figure 4.10 An example of the time evolution and dynamics for the [V]*→[B4]§→[VI]S0 reaction [Eq. (4.4)], obtained from nonadiabatic microcanonical molecular dynamics simulations with surface-hopping dynamics (NVE-MDSH) simulations. $\tau_{S_1 \rightarrow S_0}$ = $S_1 \rightarrow S_0$ surface hopping time; T_{S1}^{Av} = average temperature in the S_1 state; T_{S0}^{Av} = average temperature in the S_0 state.

Table 4.4 Kinetics and thermodynamic properties of the rate-determining elementary reactions in the S_0 state (ε = 80). Rate constants, temperatures and energies are in s^{-1}, K and kJ/mol, respectively. The symbols used are explained in the text.

Reaction path	$\Delta E^{\ddagger}$	$\Delta E^{\ddagger,ZPC}$	T_c	T	$k_f^{Q\text{-}Vib}$	$k_f^{S\text{-}Wig}$	$\Delta G_f^{\ddagger}$
$^{a}[VI]^{eq,S0} \xrightarrow{\mathbf{k_f}} {}^{b}[B6]^{\ddagger}$	157	149	352	280	2.04×10^{-16}	7.34×10^{-16}	152.5
				296	5.74×10^{-15}	1.91×10^{-14}	153.0
				313	1.61×10^{-13}	4.97×10^{-13}	153.4
				333	4.52×10^{-12}	1.28×10^{-11}	154.0
				355	1.26×10^{-10}	3.31×10^{-10}	154.6
				380	3.51×10^{-9}	8.47×10^{-9}	155.3
				400	3.59×10^{-8}	8.18×10^{-8}	156.0
				483	6.94×10^{-5}	1.30×10^{-4}	158.6
				538	3.03×10^{-3}	5.17×10^{-3}	160.5
				609	1.32×10^{-1}	2.05×10^{-1}	162.9
				700	5.74×10^{0}	8.13×10^{0}	166.2
				1091	4.79×10^{4}	5.62×10^{4}	181.2
				1385	1.52×10^{6}	1.68×10^{6}	193.0
				1600	8.60×10^{6}	9.29×10^{6}	201.8
				1888	4.83×10^{7}	5.11×10^{7}	213.9
				2323	2.85×10^{8}	2.96×10^{8}	232.5
				3000	1.67×10^{9}	1.71×10^{9}	262.6
$^{b}[B7]^{eq,S0} \xrightarrow{\mathbf{k_f}} {}^{b}[B8]^{\ddagger}$	130	125	357	280	8.26×10^{-16}	3.03×10^{-15}	149.3
				296	1.38×10^{-14}	4.69×10^{-14}	150.8
				313	2.30×10^{-13}	7.22×10^{-13}	152.5
				333	3.82×10^{-12}	1.11×10^{-11}	154.4
				355	6.33×10^{-11}	1.69×10^{-10}	156.6
				380	1.04×10^{-9}	2.56×10^{-9}	159.2
				400	7.40×10^{-9}	1.71×10^{-8}	161.2
				438	1.79×10^{-7}	3.75×10^{-7}	165.1
				538	1.03×10^{-4}	1.77×10^{-4}	175.6
				609	2.44×10^{-3}	3.82×10^{-3}	183.1
				700	5.75×10^{-2}	8.21×10^{-2}	193.0
				1091	1.08×10^{2}	1.27×10^{2}	236.5
				1385	1.92×10^{3}	2.12×10^{3}	269.8
				1600	8.11×10^{3}	8.78×10^{3}	294.5
				1888	3.40×10^{4}	3.59×10^{4}	327.8
				2323	1.49×10^{5}	1.54×10^{5}	378.5
				3000	6.45×10^{5}	6.60×10^{5}	458.7

$\Delta E^{\ddagger}$ = energy barrier in kJ/mol; $\Delta E^{\ddagger,ZPC}$ = energy barrier with the zero-point vibrational energy correction; T_c = crossover temperature; T = temperature; $k_f^{Q\text{-}vib}$ = rate constant obtained with quantized vibration correction; $k_f^{S\text{-}Wig}$ = second-order Wigner corrected $k_f^{Q\text{-}vib}$; $\Delta G_f^{\ddagger}$ = activation Gibbs free energy; f = forward direction.

4.4 Techno-economic and environmental assessment of pilot-scale photocatalytic water splitting

This section presents a preliminary evaluation of the H_2 production cost, cumulative energy demand (CED), and greenhouse gas (GHG) emissions per unit of H_2 produced. The assessment is based on experimental H_2 production data to evaluate the feasibility of industrial-scale implementation. It aims to provide a comprehensive analysis of the economic, energy, and environmental aspects associated with H_2 production under various conditions. Details of the calculated results are provided in Appendix B.

4.4.1 Estimated annual H_2 production

The estimated annual H_2 production presented in Fig. 4.11 was calculated based on the experimental results of the H_2 production rate obtained from photocatalytic water splitting using the panel photoreactor described in Section 4.2. The estimation was made under different light sources, namely UVA-LED, LED, and natural sunlight. For UVA-LED and LED light sources, which are stable and controllable, the system was assumed to operate continuously for 300 days per year, 24 hours per day. In contrast, the estimation under natural sunlight was based on seasonal availability in Thailand, where the system was assumed to operate for up to six months per year (approximately 180 days), with an average of 7 hours of effective sunlight per day (from 08:00 to 15:00). The estimated H_2 production is shown in Tables B1-B3 in Appendix B. The results indicate that the combination of LED light and a 2%Pt/TiO_2 photocatalyst produces the highest H_2 production among all tested conditions. Furthermore, the H_2 yield increases with higher concentrations of MeOH used as the sacrificial reagent in the feed solution, highlighting the significant influence of reactant composition on the overall process efficiency.

4.4.2 GHG emission

The United States Department of Energy's Clean Hydrogen Production Standard (CHPS) sets a lifecycle GHG emission limit of no more than 4.0 kg CO_{2eq}/kg H_2, measured from well-to-gate. Current production pathways that can meet this standard include steam methane reforming with high carbon capture and

sequestration, electrolysis powered primarily by clean energy, and certain biomass-based methods. In this work, the potential of photocatalytic water splitting to produce H_2 using the panel photoreactor will be evaluated by calculating GHG emissions (in kg CO_{2eq}/kg H_2) based on experimental process data. The analysis will consider two categories of emissions: direct GHG emissions (Scope 1) and indirect emissions from purchased energy (Scope 2) (World Resources Institute & World Business Council for Sustainable Development, 2004).

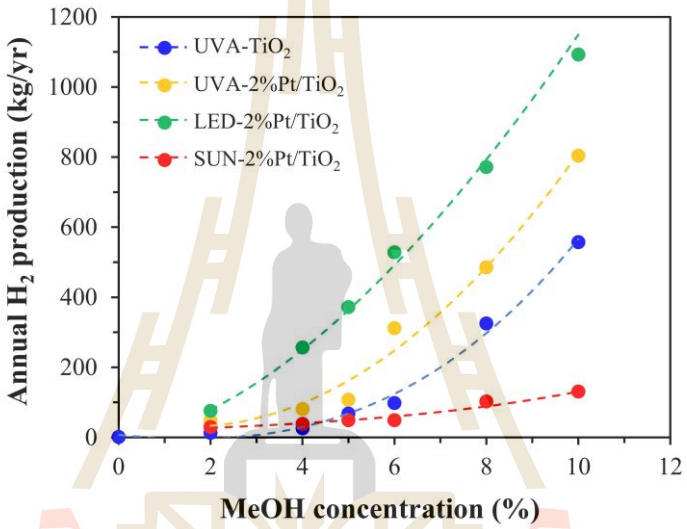

Figure 4.11 Annual H_2 production via photocatalytic water splitting at varying MeOH concentrations (2-10%) in the feed solution.

Scope 1: Direct GHG emissions.

Emissions from sources owned or controlled by the organization, such as fuel combustion in boilers, engines, or process emissions within the facility.

Scope 2: Indirect GHG emissions from purchased energy.

Emissions from the generation of purchased electricity, heat, or steam consumed by the organization, occurring offsite but resulting from the organization's energy use.

Scope 3: Other indirect GHG emissions.

Emissions from activities in the value chain not included in Scope 1 or 2 include: transportation of raw materials or products, waste management, use of sold products or services, and production of purchased goods and services.

4.4.2.1 GHG emission from photocatalyst material preparation

Based on the experimental procedure for the preparation of TiO_2 and 2%Pt/TiO_2 photocatalyst materials, the associated material and energy consumption, as well as the corresponding GHG emissions, are summarized in Table 4.5. The preparation process consists of seven main steps:

(1) Photocatalyst solution preparation: 0.0000027 g CO_{2eq}/g_{cat}.

(2) Coating of the photocatalyst solution onto a glass substrate: 0.000001 g CO_{2eq}/g_{cat}.

(3) Drying of the photocatalyst material: 0.00378 g CO_{2eq}/g_{cat}.

(4) Calcination of the photocatalyst material: This step involves the combustion of polyurethane present in the photocatalyst material to promote the TiO_2. The GHG emission from this step was estimated based on the stoichiometry of polyurethane (—[-NH-CO-O-R-]$_n$—), with an approximate elemental composition of C:H:O:N ≈ 3:5:2:1. For 800 µL (0.96 g) of polyurethane and assuming 50 wt% carbon (C) content, the carbon mass is 0.96 × 0.5 ≈ 0.48 g C. Based on the combustion reaction, $C + O_2 \rightarrow CO_2$, the resulting CO_2 emission is 0.48 × (44/12) ≈ 1.76 g CO_2. Therefore, the total GHG emission for this step is 0.00594 + 1.76 ≈ 1.76594 g CO_{2eq}/g_{cat}.

(5) Preparation of the Pt solution for deposition onto the photocatalyst material: 0.000081 g CO_{2eq}/g_{cat}.

(6) Photodeposition of 2%Pt onto TiO_2: 0.00003 g CO_{2eq}/g_{cat}.

(7) Drying of the 2%Pt/TiO_2 photocatalyst: 0.00492 g CO_{2eq}/g_{cat}.

In summary, considering GHG emissions from Scope 1 and 2 activities, the total emissions for TiO_2 photocatalyst production (steps 1-4) were 1.76972 g CO_{2eq}/g_{cat}, whereas for 2%Pt/TiO_2 (steps 1-7) the total emissions were 1.77475 g CO_{2eq}/g_{cat}.

Table 4.5 Inventory analysis of fabrication steps for TiO_2 and 2%Pt/TiO_2 based on experimental data.

Process		Materials	Amount	Unit	CED^{cal} (MJ)	GHG^{cal} (gCO_{2eq})	CED^{ref} (MJ/Unit)		GHG^{ref} (gCO_{2eq}/Unit)		References	Scope (GHG)
Photocatalyst solution preparation	Material	TiO_2-anatase	1.00	g	0.09260	7.47	0.09260	MJ/g	7.47	gCO_{2eq}/g	(Middlemas et al., 2015)	3
		Polyurethane (800 µL)	0.96	g	0.07248	2.93	0.07550	MJ/g	3.05	gCO_{2eq}/g	(Patel et al., 2003)	3
	Energy	Electricity (0.0045 kWh) (Stirring machine)	Machine input		0.01620	0.0000027	-	-	0.60	$kgCO_{2eq}$/kWh	Thai National LCI Database, TIIS-MTEC-NSTDA	2
	Output	Photocatalyst solution			0.18128	10.40						
Coating of photocatalyst solution on a glass sheet	Material	Photocatalyst solution	-	-	-	-	-	-	-	-		
		Glass sheet (345 cm^2)	167.45	g	1.30611	212.83	7800	MJ/ton	1.27	gCO_{2eq}/g	Thai National LCI Database, TIIS-MTEC-NSTDA, and Schmitz et al., 2011	3
	Energy	Electricity (0.0017 kWh) (Doctor blade coater)	Machine input		0.006	0.0000010	-	-	0.60	$kgCO_{2eq}$/kWh	Thai National LCI Database, TIIS-MTEC-NSTDA	2
	Output	Photocatalyst coated on glass sheet			1.31211	212.83						
Drying of photocatalyst material (TiO_2)	Material	Photocatalyst coated on glass sheet	-	-	-	-	-	-	-	-		
	Energy	Electricity (6.3 kWh) (Convection oven)	Machine input		22.68	0.00378	-	-	0.60	$kgCO_{2eq}$/kWh	Thai National LCI Database, TIIS-MTEC-NSTDA	2
	Output	Photocatalyst coated on glass sheet (dry)			22.68	0.00378	-	-	-	-		
Calcination of photocatalyst material (TiO_2)	Material	Photocatalyst coated on glass sheet (dry)	-	-	-	-	-	-	-	-	-	
	Energy	Electricity (9.9 kWh) (Air furnace)	Machine input		35.64	0.00594			0.60	$kgCO_{2eq}$/kWh	Thai National LCI Database, TIIS-MTEC-NSTDA	2
	Output	TiO_2 photocatalyst material			35.64	0.00594	-	-	-	-		

Table 4.5 Inventory analysis of fabrication steps for TiO2 and 2%Pt/TiO2 based on experimental data (continue).

Process		Materials	Amount	Unit	CED^{cal} (MJ)	GHG^{cal} (gCO_{2eq})	CED^{ref} (MJ/Unit)		GHG^{ref} (gCO_{2eq}/Unit)		References	Scope (GHG)
Preparation of the Pt solution for deposition onto the photocatalyst material	Material	Water	90	mL	0.00180	0.0000002	0.00002	MJ/mL	2.04	$kgCO_{2eq}/m^3$	Thai National LCI Database, TIIS-MTEC-NSTDA, and (Maurya et al., 2022)	1
		Methanol (10 mL)	7.91	g	0.31956	13.53	0.04040	MJ/g	1.17	gCO_{2eq}/g	(Patel et al., 2003)	3
		H_2PtCl_6	0.0536	g	0.05521	72.36	1.03	MJ/g	1.350	$kgCO_{2eq}/g$*	(Maurya et al., 2022; Hwang et al., 2023)	3
	Energy	Electricity (0.135 kWh) (Stirring machine)	Machine input		0.486	0.000081	-	-	0.60	$kgCO_{2eq}$/kWh	Thai National LCI Database, TIIS-MTEC-NSTDA	2
	Output	Mixed solution			0.86257	85.8901	-	-	-	-		
Photo-deposition	Material	TiO_2 photocatalyst material	-	-	-	-	-	-	-	-		
		Mixed solution	-	-	-	-	-	-	-	-		
	Energy	Electricity (0.05 kWh) (UV light)	Machine input		0.18	0.00003	-	-	0.60	$kgCO_{2eq}$/kWh	Thai National LCI Database, TIIS-MTEC-NSTDA	2
	Output	2%Pt/TiO_2 photocatalyst material			0.18	0.00003	-	-	-	-		
Drying of photocatalyst material (2%Pt/TiO_2)	Material	2%Pt/TiO_2 photocatalyst material	-	-	-	-	-	-	-	-	-	
	Energy	Electricity (8.2 kWh) (Convection oven)	Machine input		29.52	0.00492	-	-	0.60	$kgCO_{2eq}$/kWh	Thai National LCI Database, TIIS-MTEC-NSTDA	2
	Output	2%Pt/TiO_2 photocatalyst material			29.52	0.00492						

Cumulative energy demand (CED) and greenhouse gas (GHG).

* Due to the lack of data, we assume based on Pt.

4.4.2.2 GHG emission from the H_2 production process

The estimated CO_2 emissions from the photocatalytic water splitting reaction using MeOH as a sacrificial reagent were calculated for different concentrations (2-10% v/v). Although the H_2 evolution rate increases with MeOH concentration, the reaction stoichiometry remains unchanged. Assuming no side reactions, the GHG emissions were estimated based on the amount of H_2 produced, with the corresponding CO_2 calculated by back-referencing the reaction stoichiometry. Consequently, the GHG emissions are theoretically identical under all MeOH concentrations. Thus, the GHG emission from the photocatalytic water splitting reaction is 7.28 kg CO_{2eq}/kg H_2 (The details of the calculations are shown in Appendix B).

Photocatalytic water splitting is driven by light sources such as UVA-LEDs and LEDs, which are powered by electricity. Therefore, GHG emissions can be estimated based on the electricity consumption (Table B5). For this study, emission factors of 0.60 kg CO_{2eq}/kWh for non-renewable electricity and 0.05 kg CO_{2eq}/kWh for renewable electricity were applied.

4.4.2.3 GHG emissions from the photocatalytic water splitting process

Fig. 4.12 illustrates the GHG emissions associated with the photocatalytic water splitting process, considering three primary sources: (i) electricity consumption from both non-renewable and renewable sources, (ii) photocatalyst preparation, and (iii) the photocatalytic reaction ($CH_3OH + H_2O \rightarrow CO_2 + 3H_2$). The results indicate that GHG emissions decrease with increasing MeOH concentration due to the enhanced H_2 production rate.

The analysis shows that the dominant contributor to GHG emissions is electricity consumption. When renewable electricity is employed, total GHG emissions are reduced by up to 91% across all conditions using UVA-LED and LED light sources. For example, as shown in Fig. 4.12(a), non-renewable electricity use results in emissions as high as 115 kg CO_{2eq}/kg H_2. In contrast, under renewable electricity at 10% v/v MeOH, emissions are significantly reduced to 16 kg CO_{2eq}/kg H_2

(Fig. 4.12(b)). Nevertheless, the clean H_2 production standard requires GHG emissions to remain below 4 kg CO_{2eq}/kg H_2.

To improve photocatalytic activity, deposition of 2% w/w Pt on TiO_2 was investigated. This modification further reduces emissions, achieving 14 kg CO_{2eq}/kg H_2 at 10% v/v MeOH (Fig. 4.12(c)-(d)). When combined with renewable electricity, LED irradiation using 2%Pt/TiO_2 achieves emissions as low as 12 kg CO_{2eq}/kg H_2 (Fig. 4.12(f)). Despite these improvements, none of the tested conditions reached the < 4 kg CO_{2eq}/kg H_2 threshold, primarily because the photocatalytic reaction contributes approximately 7.28 kg CO_{2eq}/kg H_2 on average.

Carbon capture technology (CCT), which has already demonstrated high efficiency when integrated with steam methane reforming (U.S. Department of Energy, 2021), offers a promising solution. Incorporating CCT into this process reduces emissions to 9, 6, and 5 kg CO_{2eq}/kg H_2 for UVA-LED with TiO_2, UVA-LED with 2%Pt/TiO_2, and LED with 2%Pt/TiO_2, respectively (Fig. 4.13). Among these, LED with 2%Pt/TiO_2 approaches compliance with the clean H_2 standard. Further reductions below 5 kg CO_{2eq}/kg H_2 may require increasing the H_2 production rate or developing more efficient photocatalysts.

Interestingly, when natural sunlight is employed as the light source with 2%Pt/TiO_2, the theoretical GHG emission is as low as 0.12 kg CO_{2eq}/kg H_2. However, real-production process must account for additional factors such as H_2 production rate, stability of the light source, and overall production cost. In this study, the most favorable condition was achieved with an LED light source, a 2%Pt/TiO_2 photocatalyst, and 10% v/v MeOH as a sacrificial agent, resulting in GHG emissions of approximately 5 kg CO_{2eq}/kg H_2 when integrated with CCT.

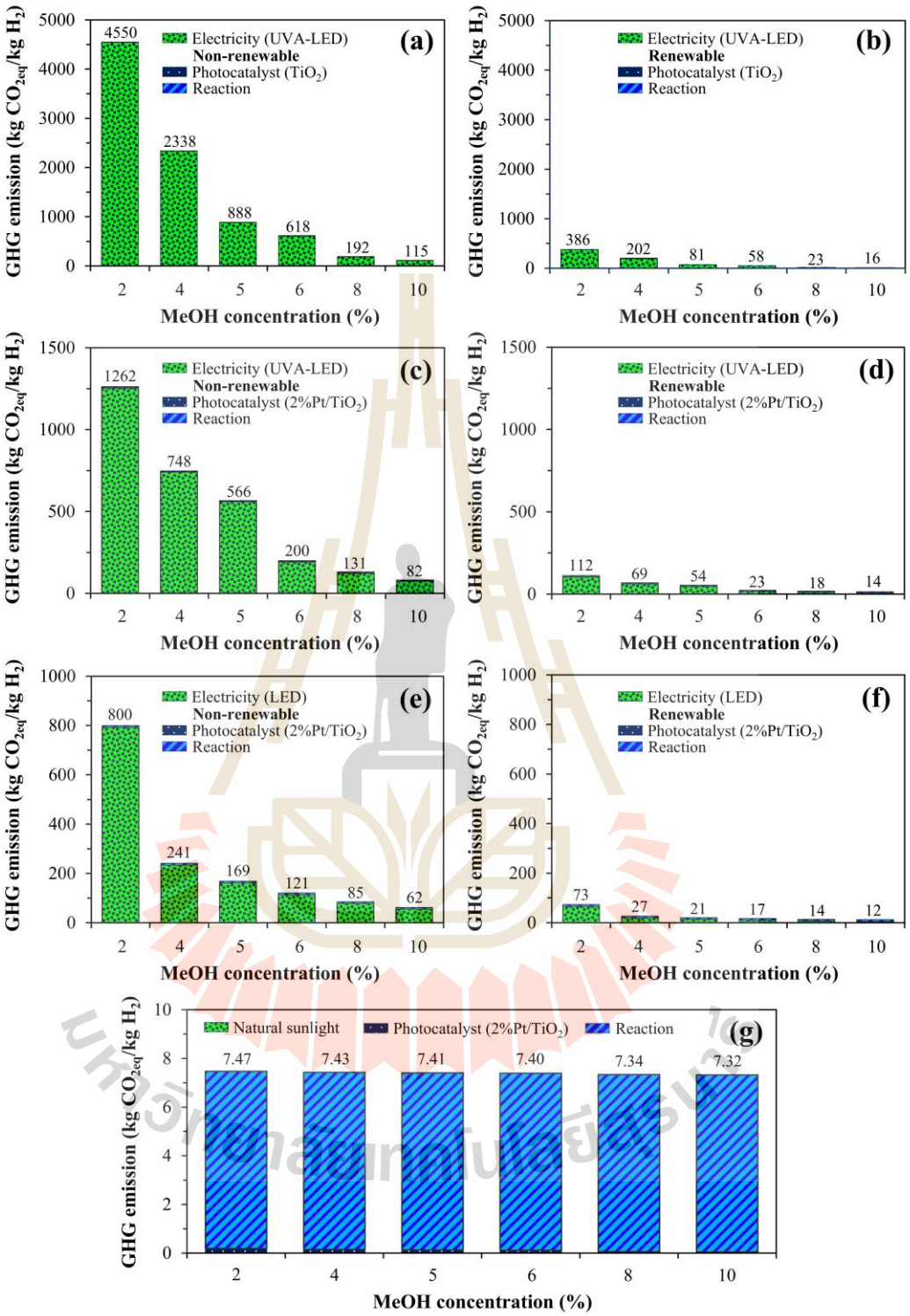

Figure 4.12 Life cycle GHG emissions from photocatalytic water splitting for H_2 production using non-renewable and renewable electricity sources: (a)-(b) UVA-LED with TiO_2, (c)-(d) UVA-LED with 2%Pt/TiO_2, (e)-(f) LED with 2%Pt/TiO_2, and (g) natural sunlight with 2%Pt/TiO_2.

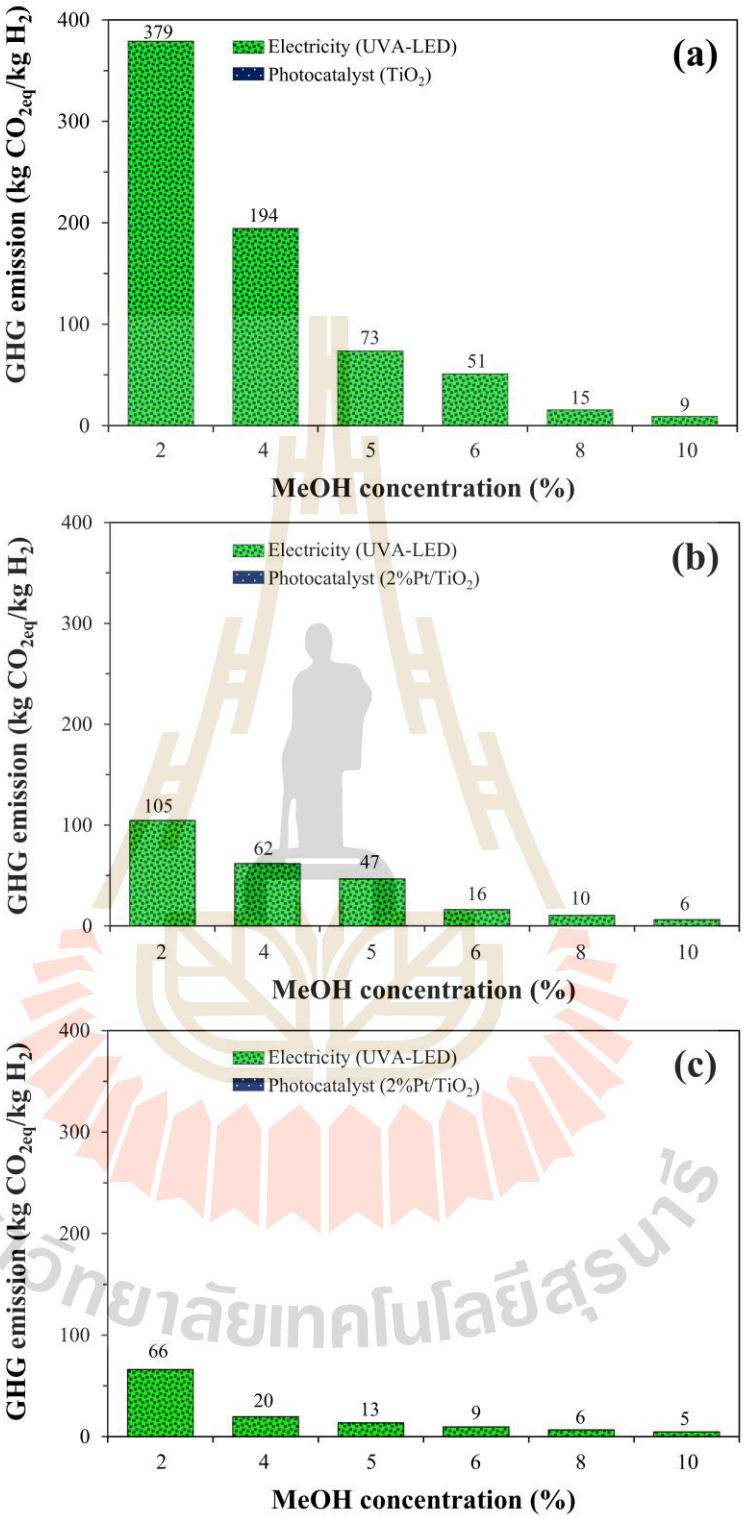

Figure 4.13 Life cycle GHG emissions from photocatalytic water splitting for H_2 production using renewable electricity sources with integrated CO_2 capture: (a) UVA-LED with TiO_2, (b) UVA-LED with 2%Pt/TiO_2, and (c) LED with 2%Pt/TiO_2.

4.4.3 Cumulative energy demand

This study evaluates the cumulative energy demand (CED) associated with H_2 production via photocatalytic water splitting, as illustrated in Fig. 4.14. The CED assessment focused on the light source (UVA-LED and LED), photocatalyst preparation, water filtration unit, CO_2 capture unit, and H_2 storage unit. As shown in Fig. 4.14, the CED was evaluated on an annual basis. An increase in CED is observed with higher H_2 production rates, since greater energy input is required for gas purification and system operation.

In Fig. 4.14(a), the primary contribution to the CED arises from the light source (UVA-LED), accounting for approximately 360,288 MJ/yr, followed by the preparation of the TiO_2 photocatalyst at 3,261 MJ/yr. The estimated CED values for the water filtration unit, CO_2 capture unit, and H_2 storage unit are 0.84 kWh/m^3, 1 MJ/kg CO_2, and 6 kWh/kg H_2, respectively (Aziz, 2021; Sim et al., 2021; Larsen, 2022). The total annual CED increases progressively with rising MeOH concentrations from 0 to 10% v/v, reaching values of 363,937, 364,286, 364,641, 365,863, 366,730, 373,272, and 379,972 MJ/yr, respectively.

In Fig. 4.14(b), under the same conditions but using 2%Pt/TiO_2 as the photocatalyst, the preparation requires 5,716 MJ/yr. Compared with pure TiO_2, this corresponds to an additional 2,455 MJ/yr, primarily due to the photodeposition and 2%Pt/TiO_2 drying processes. The total CED with increasing MeOH concentrations from 0 to 10% v/v is 367,742, 368,695, 369,454, 375,359, 380,363, and 389,549 MJ/yr, respectively.

When considering the LED light source with 2%Pt/TiO_2 photocatalyst (Fig. 4.14(c)), the CED is comparable to the UVA-LED under identical light intensities, as the energy demand is dependent on power consumption rather than light type. However, the light source influences the system cost. The total CED with increasing MeOH concentrations of 0-10% v/v is 368,547, 373,769, 377,097, 381,609, 388,624, and 397,889 MJ/yr, respectively.

For natural sunlight (SUN) combined with 2%Pt/TiO_2 photocatalyst (Fig. 4.14(d)), the CED excludes electricity consumption for the light source, resulting in substantially lower values. Nonetheless, the CED still increases slightly with higher

MeOH concentrations from 0 to 10% v/v, reaching 6,794, 7,048, 7,192, 7,337, 8,874, and 9,699 MJ/yr, respectively. Fig. 4.15 shows the CED per kilogram of H_2 produced. The lowest CED is obtained with natural sunlight and 2%Pt/TiO_2, followed by LED with 2%Pt/TiO_2, UVA-LED with 2%Pt/TiO_2, and UVA-LED with TiO_2. Across all cases, a MeOH concentration of 10% v/v yields the lowest CED due to the higher H_2 production rate compared with other concentrations.

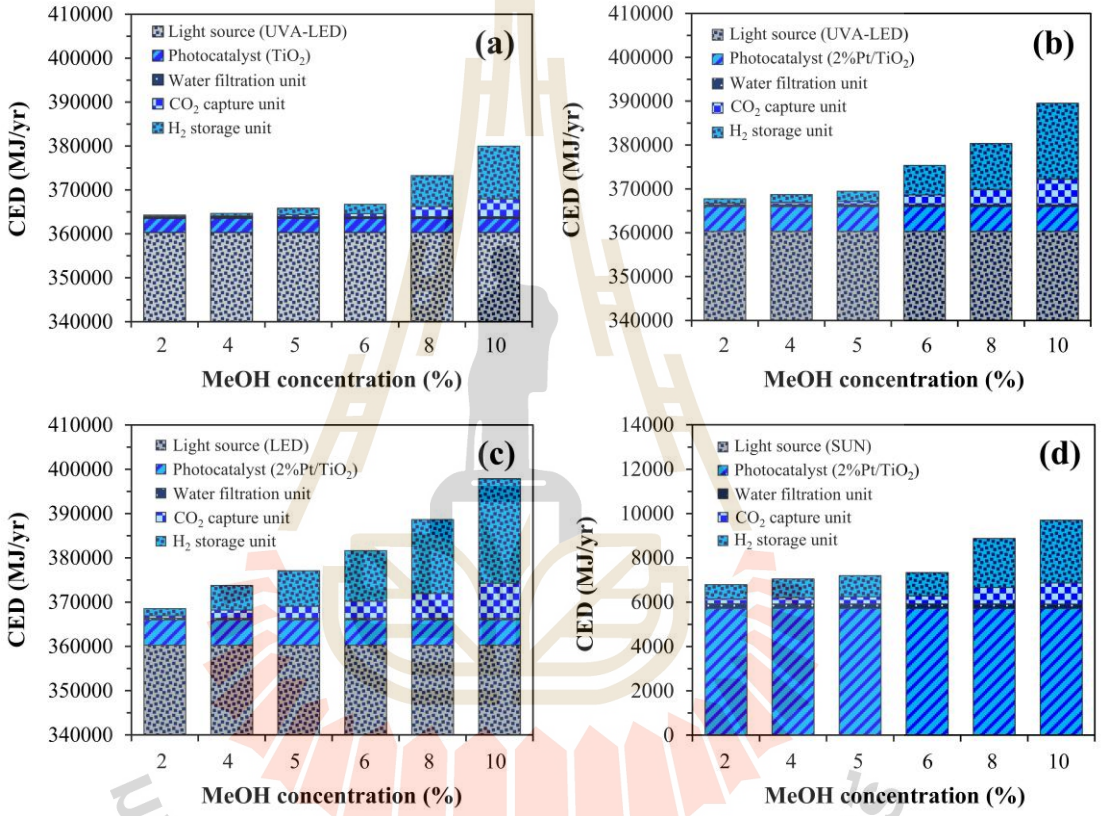

Figure 4.14 Estimated annual CED for H_2 production from photocatalytic water splitting using a panel photoreactor (100 m^2) under different operating conditions: (a) UVA-LED with TiO_2, (b) UVA-LED with 2%Pt/TiO_2, (c) LED with 2%Pt/TiO_2, and (d) natural sunlight (SUN) with 2%Pt/TiO_2.

Fig. 4.16 illustrates the energy output from the produced H_2, assuming an energy content of approximately 120 MJ/kg H_2. Thus, increased H_2 production directly enhances the system's net energy output. The energy payback time (EPBT), defined as the ratio of total cumulative energy consumption (E_{tot}) to annual energy

output (E_{out}), was calculated using EPBT = E_{tot} / E_{out}, where E_{out} is derived as H_2 mass × 120 MJ/kg (Maurya et al., 2022). Results show that systems employing 2%Pt/TiO_2 achieve EPBT values ranging from 0.003 to 1.34 years. The shortest EPBT (0.06 years) is observed in the natural sunlight with 2%Pt/TiO_2 system at a MeOH concentration of 2% v/v. In contrast, systems using UVA-LED with TiO_2, UVA-LED with 2%Pt/TiO_2, and LED with 2%Pt/TiO_2 require higher MeOH concentrations of 8%, 6%, and 4% v/v, respectively, to achieve comparable energy returns.

For comparison, reported EPBT values of other H_2 production technologies are approximately 3 years for steam methane reforming (SMR), 2.5 years for coal-based production, 0.9 years for wind-powered electrolysis, and 1.05 years for solar PV-based systems (Celik et al., 2016; Gómez-Camacho et al., 2019). These findings highlight that photocatalytic water splitting exhibits highly competitive energy payback performance relative to established renewable technologies. With further optimization of photocatalysts and light source configurations, this approach holds significant potential for scaling up to industrial H_2 production.

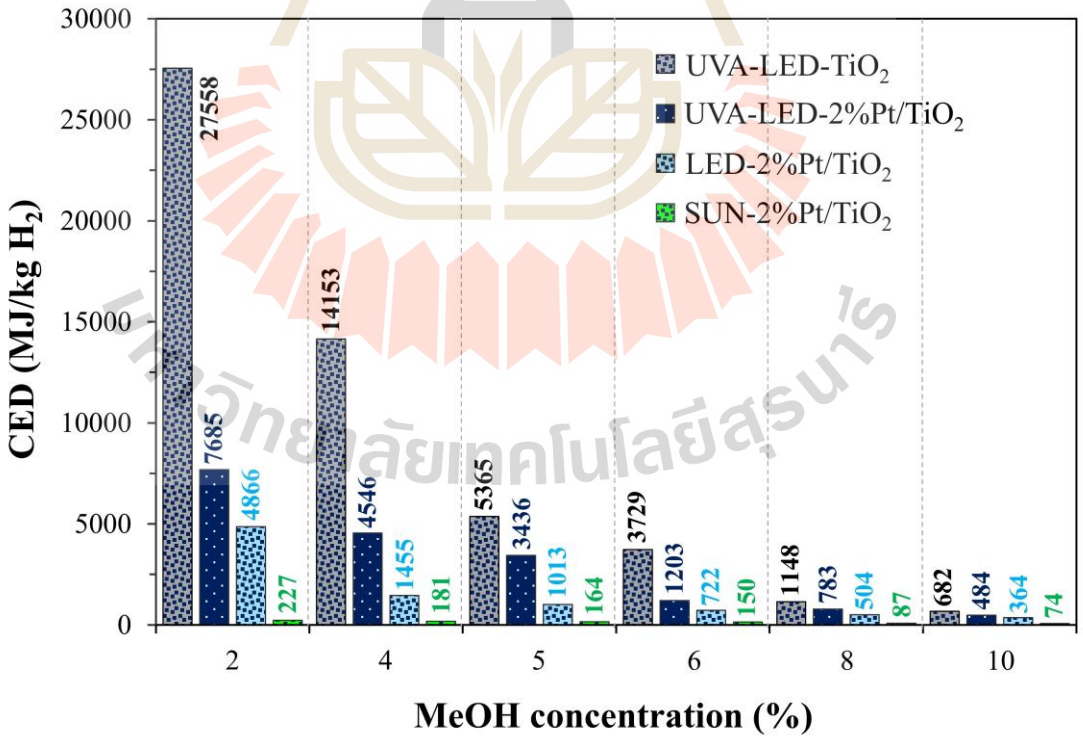

Figure 4.15 CED per kg H_2 under different operating conditions for photocatalytic water splitting.

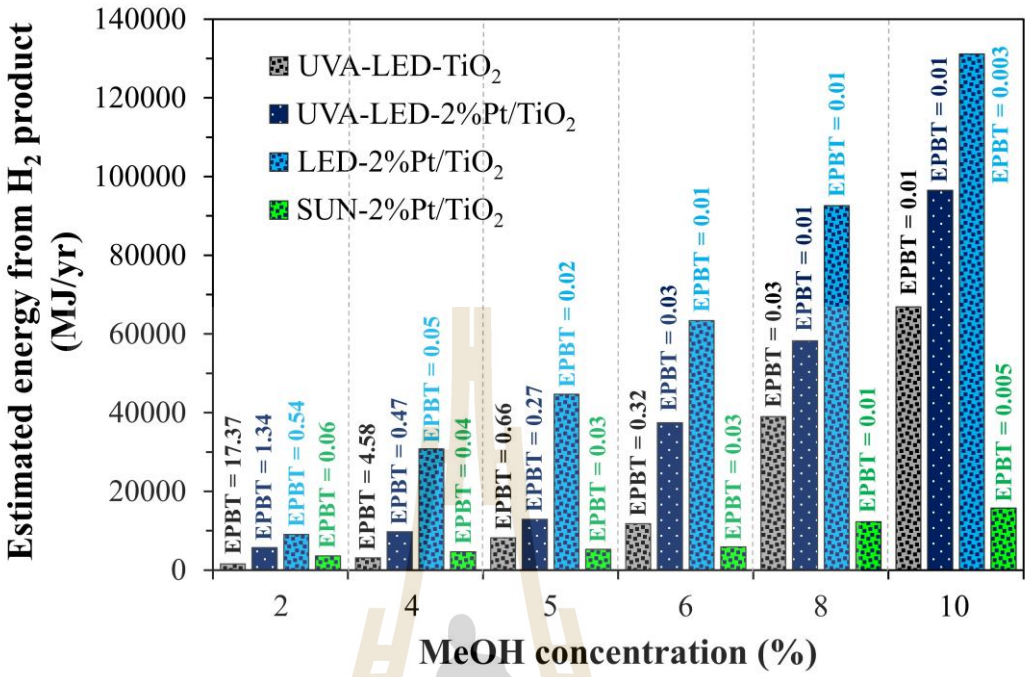

Figure 4.16 Estimated energy from H_2 production and the energy payback time (EPBT) with different light sources and photocatalysts.

4.4.4 Production cost

The assessment of the unit production cost of H_2 from a prototype photocatalytic water-splitting process is fundamental to the techno-economic evaluation of clean energy technologies. Such analyses identify cost-intensive components that constrain scale-up, reveal process inefficiencies, and guide strategies for system optimization. Achieving a substantial reduction in unit cost is pivotal for improving the competitiveness of photocatalytic H_2 production and facilitating the transition toward sustainable energy systems.

Fig. 4.17 presents a detailed breakdown of the production cost, including electricity consumption, employee salaries, space rental, photocatalyst, reactants, water filtration, CO_2 capture, and H_2 storage. When considering the unit cost of H_2 production while excluding capital equipment costs, the analysis focuses exclusively on the annual operational expenditures associated with chemical materials and energy consumption. This approach provides a direct evaluation of recurring costs necessary to sustain photocatalytic H_2 production. The estimated annual salary for three laboratory personnel (approximately 616 USD per person per month) totals

22,181 USD/yr. Electricity costs are the major contributor for UVA-LED and LED light sources, accounting for 16,756 USD/yr (Fig. 4.17(a)-(c)). Space rental for a 300 m^2 facility in Thailand is estimated at 218 USD/yr. The cost of the water filtration unit is based on a reverse osmosis (RO) system, with operational expenses of 0.54 USD/m^3 and energy demand of 0.84 kWh/m^3 (Giammar et al., 2021). For H_2 purification, CO_2 capture is considered at 0.92 USD/kg CO_2, following data from biomass-fueled H_2 plants (Makihira et al., 2003). H_2 storage costs, assuming one-week storage, range from 0.055-0.091 USD/kg H_2, with an additional 1.2 USD/kg for liquefaction in large-scale plants (Burke et al., 2024). All costs presented account for annual recurring expenses within the process.

Regarding material costs, TiO_2 photocatalyst contributes only 14.28 USD/yr, while reactant costs increase with MeOH concentration. For 2%Pt/TiO_2, the annual cost is 3,290 USD, primarily due to H_2PtCl_6-based Pt (3,133 USD/yr), followed by water (134 USD/yr), methanol (9 USD/yr), polyurethane (8 USD/yr), and TiO_2-anatase (6 USD/yr). Although only 0.05 g of H_2PtCl_6 is used per panel to achieve 2% w/w Pt loading, its high market price (~18 USD/g) substantially impacts overall costs. While Pt incorporation significantly enhances photocatalytic performance, its high cost remains a major constraint for industrial scalability. Therefore, exploring alternative catalysts with comparable efficiency but lower cost is crucial for future development. Notably, the material cost of the panel-photoreactor system is only 0.49 USD/panel, highlighting the potential economic feasibility of scaling up photocatalytic water splitting for industrial H_2 production relative to other renewable technologies.

Fig. 4.18 illustrates that H_2 production costs decrease as MeOH concentration increases due to higher H_2 yields. Among the tested conditions, LED-2%Pt/TiO_2 demonstrates the lowest total annual cost. Although natural sunlight with 2% Pt/TiO_2 appears the cheapest in energy terms (Fig. 4.17(d)), its operation is limited to 180 days per year due to seasonal variations, resulting in lower annual H_2 output. In contrast, systems using artificial lighting can operate up to 300 days per year. Consequently, the unit production cost follows the order: LED-2%Pt/TiO_2 < UVA-LED-2%Pt/TiO_2 < UVA-LED-TiO_2 < SUN-2%Pt/TiO_2 at MeOH concentrations above 2% v/v.

Nevertheless, even under optimal conditions, H_2 production costs remain relatively high, potentially limiting commercial feasibility.

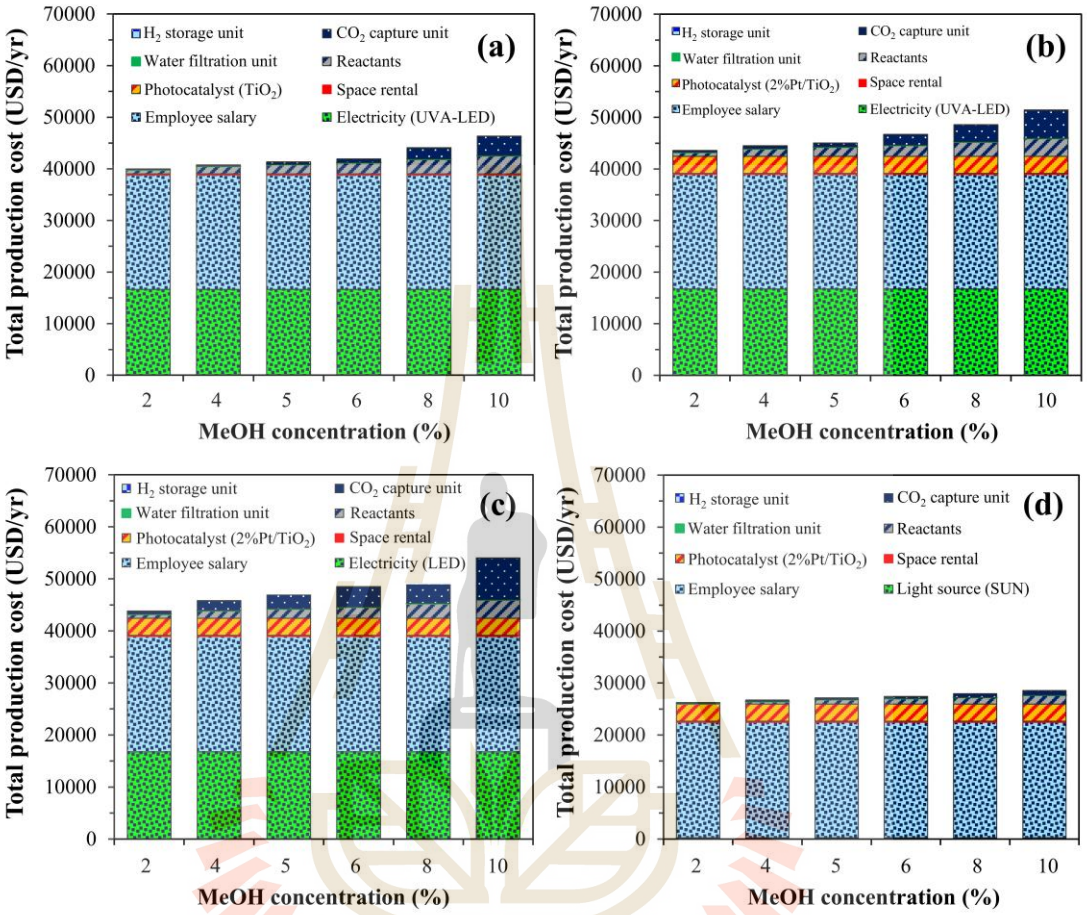

Figure 4.17 The classified production cost in the photocatalytic water-splitting process: (a) UVA-LED with TiO_2, (b) UVA-LED with 2%Pt/TiO_2, (c) LED with 2%Pt/TiO_2, and (d) natural sunlight (SUN) with 2%Pt/TiO_2.

Several strategies can improve process viability and reduce costs. First, substituting Pt-based catalysts with low-cost alternatives such as graphitic carbon nitride (g-C_3N_4) or transition-metal composites could maintain performance while reducing material expenses (Maurya et al., 2022). Second, hybrid operation combining natural sunlight during the day with artificial lighting at night or during cloudy periods can extend annual operational hours, increasing H_2 output and distributing fixed costs over higher production. In solar-rich regions like Thailand, system design should maximize solar utilization, potentially incorporating seasonal planning and modular

configurations. Although photocatalytic water splitting for H_2 production is still in the early stages of economic viability, it presents a promising pathway toward sustainable energy generation. Future research should prioritize cost reduction, performance enhancement, and environmental compatibility to enable broader adoption and integration into renewable energy portfolios.

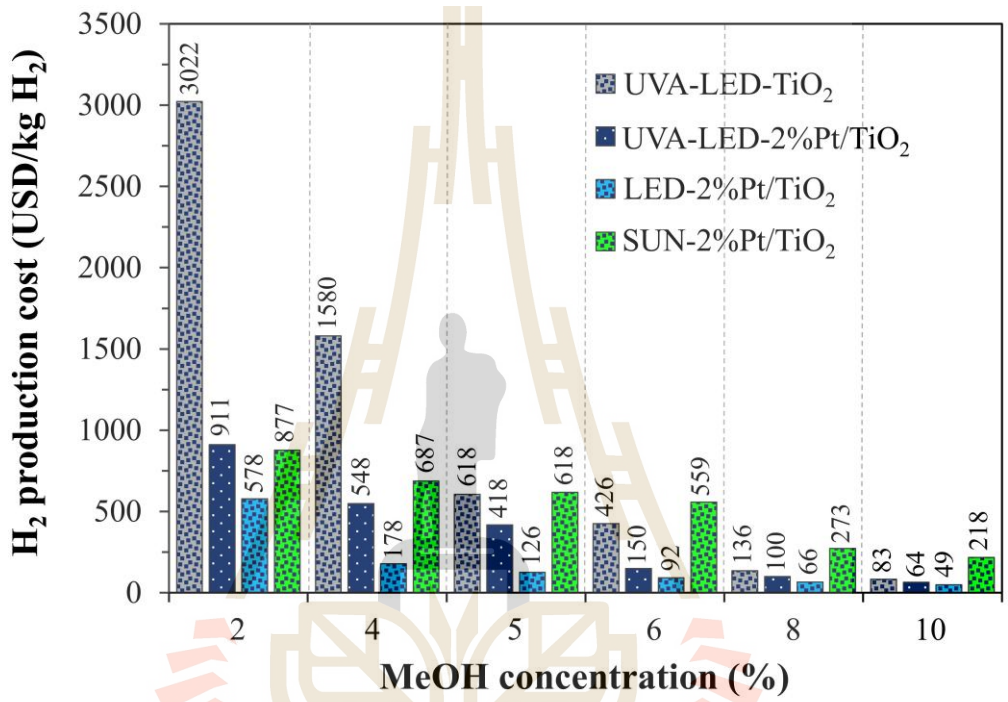

Figure 4.18 The H_2 production cost under different conditions.

CHAPTER V
CONCLUSIONS

5.1 Lab-scale panel photoreactor process

This study developed a conceptual framework to transition H_2 production from batch photoreactors, commonly used in lab-scale studies, to a continuous process system. The lab-scale prototype integrates a continuous-panel photoreactor for photocatalytic water splitting with additional units for moisture removal and gas purification via pressure swing adsorption (PSA), closely mimicking industrial operations. The system includes thermal regulation, fluid circulation, and comprehensive sensors and controls at key points. By combining H_2 production, dehumidification, and PSA purification modules, the prototype demonstrates a near-industrial representation of continuous H_2 generation, highlighting its potential for scale-up and practical application.

5.2 Photocatalyst preparation for mass production

From the preliminary screening of various photocatalysts, 2%Pt/TiO_2 demonstrated the highest photocatalytic activity for H_2 production, both in powder form and when immobilized on glass substrates. Compared to other tested catalysts such as 2%Ag/TiO_2, 2%Pt/$SrTiO_3$, and 2%RuRh/$SrTiO_3$, Pt-loaded TiO_2 consistently achieved superior H_2 evolution rates, confirming its suitability as the primary photocatalyst for scale-up. Immobilization of the photocatalyst onto glass sheets further enhanced light utilization efficiency and stability compared to powder suspensions, with TiO_2-anatase outperforming P25.

The optimized 2%Pt/TiO_2 photocatalyst was successfully prepared via photodeposition, leading to the formation of highly dispersed Pt nanoparticles on the TiO_2 surface. Structural characterization confirmed the retention of the anatase phase with only a slight reduction in crystallite size after Pt loading. Optical analysis revealed a red-shift in absorption and a narrowed band gap (from 3.2 to 3.1 eV), indicating

enhanced visible-light harvesting capability. Surface characterization by BET confirmed a mesoporous structure with adequate surface area to facilitate photocatalytic reactions.

These findings validate the effectiveness of 2%Pt/TiO_2 as a practical photocatalyst candidate for mass production. The preparation method ensures uniform Pt dispersion, strong photocatalyst-substrate adhesion, and high photocatalytic efficiency, making it suitable for integration into large-scale panel photoreactor systems for continuous H_2 production.

5.3 Panel photoreactor performance

This study investigated the photocatalytic water splitting process using TiO_2 and Pt-loaded TiO_2 photocatalysts in a panel photoreactor under different light sources, temperatures, and methanol concentrations. The results reveal several important findings that contribute to understanding both the fundamental behavior and the practical application of this system.

Firstly, the effect of temperature on pure water splitting without sacrificial reagents demonstrated that H_2 evolution decreased at elevated temperatures, despite the endothermic nature of the reaction. This phenomenon was attributed to enhanced electron–hole recombination and potential photocatalyst instability, consistent with previous literature. These observations confirm that, for continuous operation, approximately 25 ℃ represents the optimal condition for TiO_2-based systems.

Secondly, the introduction of methanol as a sacrificial reagent significantly enhanced H_2 production. H_2 evolution increased proportionally with methanol concentration up to 8-10% v/v, beyond which the rate plateaued, indicating a system limitation under fixed light intensity and catalyst dosage. This enhancement is explained by the role of methanol in scavenging photogenerated holes, thereby suppressing recombination and facilitating more efficient charge utilization.

Thirdly, modification of TiO_2 with 2% w/w Pt resulted in a substantial improvement in photocatalytic activity across all methanol concentrations and light sources. Pt deposition facilitated charge separation, extended electron lifetime, and inhibited the reverse reaction between H_2 and O_2. As a result, H_2 evolution was up to

3-4 times higher than that of bare TiO_2, demonstrating the effectiveness of Pt as a cocatalyst.

Fourthly, comparison among UVA-LED, LED, and natural sunlight revealed that LED provided the highest H_2 evolution, followed by natural sunlight and UVA-LED. This was associated with differences in spectral distribution and light penetration through the quartz window of the photoreactor. Furthermore, a moderate temperature rise (1.5-5 ℃) under each light source highlighted the importance of thermal effects in long-term operation.

Finally, the panel photoreactor design itself proved to be a key factor in enhancing performance compared to conventional batch systems. The continuous-flow configuration allowed for effective removal of products, minimized reverse reactions, and ensured stable photocatalytic activity over time. These advantages suggest that reactor engineering, alongside photocatalyst modification, is crucial for scaling up the technology toward industrial application.

This study establishes that photocatalytic water splitting in a panel photoreactor is feasible and effective when optimized for temperature, sacrificial reagent concentration, cocatalyst modification, and light source selection. While challenges remain in achieving higher H_2 yields under pure water conditions, the combined use of Pt-loaded TiO_2, sacrificial reagents, and continuous photoreactor operation demonstrates a clear pathway toward improving system efficiency. These findings provide valuable insights for future scale-up, emphasizing the need to integrate advanced catalyst design with optimized photoreactor configurations to realize practical, sustainable H_2 production.

5.4 Photocatalytic pathways for H_2 production (theoretical study)

In this study, the two- and four-electron pathways for photocatalytic water splitting were thoroughly examined using quantum chemical and TST methods. By contrast to previous theoretical studies, the current investigation focused, for the first time, on the range of irradiation wavelengths, which could drive thermodynamically and kinetically favorable pathways in high and low local dielectric environments (ε = 80 and 1 for the aqueous solution and gas phase, respectively).

The proposed elementary reactions commenced with the adsorption of water molecules onto a titanium dioxide model cluster [$(TiO_2)_2$], where multiple photoexcitation and nonradiative relaxation can induce covalent bond dissociation and isomerization, resulting in the formation of H_2, H_2O_2, and O_2 and the regeneration of the $(TiO_2)_2$ photocatalyst. Quantum chemical methods, including DFT/B3LYP/TZVP and TD-DFT/B3LYP/TZVP, were rigorously validated against both experimental and theoretical data and subsequently used to optimize the PESs in the ground state (S_0) and the excited electronic state (S_1). The kinetic and thermodynamic properties of the rate-determining elementary reactions were calculated and analyzed in detail using the TST method.

The optimized PESs revealed that via multiple photoexcitation across a broad range of irradiation wavelengths, from UVB to near-IR (λ^{abs} = 272-911 nm), along with the proposed consecutive and parallel elementary reactions, the $(TiO_2)_2$ model cluster displayed favorable pathways with no or low-energy barriers for the formation of reactive species essential for water splitting as well as for the production of H_2, O_2, and H_2O_2 and regeneration of $(TiO_2)_2$. The consecutive elementary reactions are water adsorption, dehydrogenation **(I)**, and deoxygenation, whereas the parallel elementary reactions occurring after deoxygenation are dehydrogenation **(II)**, H_2O_2 production, and $(TiO_2)_2$ regeneration.

The PESs identified two possible pathways to produce the second H_2 molecule. On the S_1 PESs [dehydrogenation **(IIa)**], the H_2 molecule can be generated without an energy barrier by irradiation with a near-IR wavelength (λ^{abs} = 911 nm), whereas on the S_0 PESs, moderate-energy barriers were observed. Based on a photo-to-thermal energy transformation model, the analysis of the thermodynamic properties suggested that in an aqueous solution, the formation of the second H_2 molecule can be highly thermodynamically favorable (spontaneous) at low temperature when all the $S_1 \rightarrow S_0$ relaxation energies released from the preceding step (deoxygenation) directly transfer to dehydrogenation **(IIb)**. Furthermore, the optimal local temperature could be at T = 1888 K to balance the thermodynamic and kinetic factors. The thermodynamic results also confirmed that the local dielectric environment (solvent effects) must be incorporated into the model calculations to obtain a realistic mechanism. The

quantum chemical and TST results presented in this study offer valuable insights into the kinetics and thermodynamics as well as the reactive intermediates involved in low-energy photochemical pathways. These findings could serve as guidelines for enhancing photocatalytic water splitting processes in experiments.

5.5 Techno-economic and environmental assessment

This work presents a comprehensive assessment of photocatalytic water splitting in a panel photoreactor (100 m^2), focusing on H_2 production, greenhouse gas (GHG) emissions, cumulative energy demand (CED), and unit production cost. The findings highlight both the promise and the challenges of this technology as a pathway to clean H_2.

From the production perspective, the experimental results demonstrate that H_2 yield strongly depends on the light source, photocatalyst, and sacrificial reagent concentration (methanol (MeOH)). The LED-2%Pt/TiO_2 system consistently achieved the highest production rates, while natural sunlight offered the lowest cost in terms of energy input but was constrained by limited annual operating hours. Increasing MeOH concentration improved H_2 yields and lowered unit production costs, indicating that reactant composition plays a crucial role in optimizing system performance.

GHG analysis reveals that electricity consumption is the dominant emission source, particularly under UVA-LED and LED irradiation powered by non-renewable energy. While renewable electricity reduces emissions by over 90%, average values (≈ 12-115 kg CO_{2eq}/kg H_2) still exceed the clean H_2 production standard of 4 kg CO_{2eq}/kg H_2. Photocatalyst preparation contributed relatively minor emissions (<2 g CO_{2eq}/g_{cat}), but the intrinsic stoichiometry of the photocatalytic reaction itself contributed about 7.28 kg CO_{2eq}/kg H_2. Incorporating carbon capture technology (CCT) demonstrated significant mitigation potential, lowering emissions to 5-9 kg CO_{2eq}/kg H_2, with LED-2%Pt/TiO_2 approaching compliance. Theoretical analysis further suggests that natural sunlight with Pt-modified TiO_2 could achieve near-zero emissions (≈0.12 kg CO_{2eq}/kg H_2), although practical implementation must account for stability, production scale, and cost.

The CED evaluation underscores the energy intensity of artificial lighting, with UVA-LED accounting for >360,000 MJ/yr compared to <10,000 MJ/yr under sunlight-driven operation. Energy payback time (EPBT) calculations revealed highly competitive values (0.003-1.34 yrs), substantially outperforming conventional fossil-based H_2 pathways (≈2.5-3 yrs) and aligning with renewable benchmarks such as wind and solar PV-based electrolysis. These findings confirm that, with optimized conditions, photocatalytic water splitting can deliver rapid energy returns, strengthening its case as a viable renewable H_2 pathway.

Economic analysis identified Pt loading and electricity costs as the primary cost-intensive components. Despite low material costs for TiO_2 and panel fabrication (<1 USD/panel), the high price of Pt-based catalysts (3,133 USD/yr) and substantial electricity demand resulted in relatively high H_2 unit costs across all scenarios. Hybrid strategies that combine natural sunlight with artificial lighting, as well as the development of low-cost, high-efficiency catalysts such as g-C_3N_4 or transition-metal composites, are essential to improving economic feasibility. The photocatalytic water splitting in a panel photoreactor demonstrates technical viability, rapid energy payback, and significant potential for carbon reduction when integrated with renewable electricity and carbon capture.

5.6 Suggestions for future research

5.1.1 Scale-up and prototype optimization

1) Develop larger-scale continuous-panel photoreactors to transition from lab-scale prototypes toward industrially relevant H_2 production.

2) Optimize photoreactor design to enhance light penetration, thermal management, and product removal efficiency.

3) Investigate the integration of multiple photoreactor modules to improve overall throughput.

5.6.2 Photocatalyst development

1) Explore alternative cocatalysts or noble-metal loadings to reduce Pt usage while maintaining high H_2 evolution efficiency.

2) Investigate other support materials or immobilization techniques to improve catalyst stability and light utilization.

3) Study long-term photocatalyst durability under continuous operation and variable environmental conditions.

5.1.2 Process optimization

1) Optimize sacrificial reagent type and concentration to maximize H_2 production while minimizing cost and environmental impact.

2) Evaluate the effects of temperature, light intensity, and wavelength distribution on photocatalytic performance under continuous operation.

3) Develop strategies to improve H_2 evolution under pure water conditions without sacrificial reagents.

5.6.4 Theoretical and mechanistic studies

1) Extend quantum chemical and TST simulations to larger TiO_2 clusters and realistic photoreactor conditions.

2) Use mechanistic insights to design catalysts and reactors that favor low-energy H_2 production pathways.

5.6.5 Energy and environmental assessment

1) Explore integration of renewable electricity sources to minimize greenhouse gas emissions.

2) Evaluate hybrid illumination strategies combining natural sunlight and artificial lighting for cost and energy efficiency.

3) Assess the potential for implementing carbon capture technologies (CCT) to reduce residual emissions.

5.6.6 Economic feasibility

1) Develop low-cost, high-efficiency photocatalysts, including g-C_3N_4 or transition-metal composites, to reduce reliance on Pt.

2) Conduct techno-economic studies considering full-scale industrial operation, electricity pricing, and material costs.

3) Investigate the trade-off between energy payback time and H_2 production efficiency for different system configurations.

5.6.7 Long-term operational stability

1) Test continuous operation over extended periods to evaluate system reliability, catalyst leaching, and product purity.

2) Monitor and mitigate reverse reactions and photocatalyst deactivation.

5.6.8 Integration with industrial applications

1) Explore coupling the panel photoreactor with downstream purification, storage, and H_2 utilization systems.

2) Assess performance under variable sunlight, ambient temperature, and humidity to mimic real-conditions.

REFERENCES

Afrin, M.F., Furukawa, M., Tateishi, I., et al. (2025). Enhanced photocatalytic hydrogen generation from methanol solutions via in situ Ni/Pt co-deposition on TiO_2. Journal of Composites Science, 9, 68.

Ahn, S., You, Y.W., Lee, D.G., et al. (2012). Layered two- and four-bed PSA processes for H_2 recovery from coal gas. Chemical Engineering Science, 68(1), 413-423.

Ahmed, S.F., Mofijur, M., Nuzhat, S., Rafa, N., Musharrat, A., Lam, S.S., et al. (2022). Sustainable hydrogen production: technological advancements and economic analysis. International Journal of Hydrogen Energy, 47, 37227-55.

Aiyun, M., Liuyang, Z., Bei, C., et al. (2019). Dual cocatalysts in TiO_2 photocatalysis. Advanced Materials, 31(30), 1807660.

Al-Azri, Z.H.N., Chen, W.T., Chan, A., et al. (2015). The roles of metal co-catalysts and reaction media in photocatalytic hydrogen production: performance evaluation of M/TiO_2 photocatalysts (M = Pd, Pt, Au) in different alcohol-water mixtures. Journal of Catalysis, 329, 355-367.

Aydin, M.I., Dincer, I. (2022). A life cycle impact analysis of various hydrogen production methods for public transportation sector. International Journal of Hydrogen Energy, 47, 39666-77.

Aziz, M. (2021). Liquid hydrogen: a review on liquefaction, storage, transportation, and safety. Energies, 14(18), 5917.

Ball, M., Weeda, M. (2015). The hydrogen economy-vision or reality?. International Journal of Hydrogen Energy, 40, 7903-19.

Bartoš, V., Vochozka, M., Šanderová, V. (2022). Copper and aluminum as economically imperfect substitutes, production and price development. Acta Montanistica Slovaca, 27(2), 462-78.

Braham, R.J., Harris, A.T. (2009). Review of major design and scale-up considerations for solar photocatalytic reactors. Industrial & Engineering Chemistry Research, 48, 8890-8905.

Burke, A., Ogden, J., Fulton, L. (2024). Hydrogen storage and transport: technologies and costs. Institute of Transportation Studies, UC Davis.

Cai, J., Wu, M., Wang, Y., et al. (2017). Synergetic enhancement of light harvesting and charge separation over surface-disorder-engineered TiO_2 photonic crystals. Chem, 2(6), 877-892.

Cao, S., Chan, T.S., Lu, Y.R., et al. (2020). Photocatalytic pure water splitting with high efficiency and value by Pt/porous brookite TiO_2 nanoflutes. Nano Energy, 67, 104287.

Cassano, A.E., Alfano, O.M. (2016). Reaction engineering of suspended solid heterogeneous photocatalytic reactors. Catalysis Today, 58(2-3), 167-197.

Celik, I., Song, Z., Cimaroli, A.J., et al. (2016). Life cycle assessment (LCA) of perovskite PV cells projected from lab to fab. Solar Energy Materials and Solar Cells, 156, 157-169.

Chase, M.W. (1998). NIST-JANAF Thermochemical Tables, 4th ed. Journal of Physical and Chemical Reference Data, Mono. 9, 1-1951.

Chen, J.J., Wu, J.C.S., Wu, P.C., et al. (2011). Plasmonic photocatalyst for H_2 evolution in photocatalytic water splitting. The Journal of Physical Chemistry C, 115(1), 210-216.

Chen, M., Straatsma, T.P., Dixon, D.A. (2015). Molecular and dissociative adsorption of water on $(TiO_2)_n$ Clusters, n = 1-4. The Journal of Physical Chemistry A, 119, 11406-11421.

Chen, X., Shi, R., Chen, Q., et al. (2019). Three-dimensional porous g-C_3N_4 for highly efficient photocatalytic overall water splitting. Nano Energy, 59, 644-650.

Chen, Y.W., Hsu, Y.H. (2021). Effects of reaction temperature on the photocatalytic activity of TiO_2 with Pd and Cu cocatalysts. Catalysts, 11(8), 966.

Chung, D., Kwon, Y., Kim, Z. (2023). Technology life cycle and commercialization readiness of hydrogen production technology using patent analysis. International Journal of Hydrogen Energy, 48, 12139-12154.

Daskalaki, V.M., Panagiotopoulou, P., Kondarides, D.I. (2011). Production of peroxide species in Pt/TiO_2 suspensions under conditions of photocatalytic water splitting and glycerol photoreforming. Chemical Engineering Journal, 170(2-3), 433-439.

Delgado, J.A., Uguina, M.A., Sotelo, J.L., et al. (2006). Fixed-bed adsorption of carbon dioxide/methane mixtures on silicalite pellets. Adsorption, 40, 11094-11111.

Dincer, I., Acar, C. (2015). Review and evaluation of hydrogen production methods for better sustainability. International Journal of Hydrogen Energy, 46, 31963-83.

Egeland-Eriksen, T., Hajizadeh, A., Sartori, S. (2021). Hydrogen-based systems for integration of renewable energy in power systems: achievements and perspectives. International Journal of Hydrogen Energy, 46, 31963-83.

Etacheri, V., Seery, M.K., Hinder, S.J., et al. (2011). Oxygen rich titania: a dopant free, high temperature stable, and visible-light active anatase photocatalyst. Advanced Functional Materials, 21(19), 3744-3752.

Fang, Z., Dixon, D.A. (2013). Computational study of H_2 and O_2 production from water splitting by small $(MO_2)_n$ Clusters (M = Ti, Zr, Hf). **The Journal of Physical Chemistry C.** 117: 3539-3555.

Fujishima, A., Honda, K. (1971). Electrochemical evidence for the mechanism of the primary stage of photosynthesis. Bulletin of the Chemical Society of Japan, 44, 1148-1150.

Fujishima, A., Honda, K. (1972). Electrochemical photolysis of water at a semiconductor electrode. Nature, 238, 37-38.

Fukuzumi, S., Lee, Y.M., Nam, W. (2017). Fuel production from seawater and fuel cells using seawater. ChemSusChem, 10, 4264-4276.

Giammar, D.E., Greene, D.M., Mishrra, A., et al. (2022). Cost and energy metrics for municipal water reuse. ACS ES&T Engineering, 2(3), 489-507.

Gómez-Camacho C.E., Ruggeri B. (2019). Energy sustainability analysis (ESA) of energy-producing processes: a case study on distributed H_2 production. Sustainability, 11(18), 4911.

González, L., Escudero, D., Serrano-Andrés, L. (2012). Progress and challenges in the calculation of electronic excited states. ChemPhysChem, 13, 28-51.

Goto, Y., Hisatomi, T., Wang, Q., et al. (2018). A particulate photocatalyst water-splitting panel for large-scale solar hydrogen generation. Joule, 2(3), 509-520.

Halgren, T.A., Lipscomb, W.N. (1977). The synchronous-transit method for determining reaction pathways and locating molecular transition states. Chemical Physics Letters, 49(2), 225-232.

Han, B., Hu, Y.H. (2016). MoS_2 as a co-catalyst for photocatalytic hydrogen production from water. Energy Science & Engineering, 4(5), 285-304.

Hänggi, P., Talkner, P., Borkovec, M. (1990). Reaction-rate theory: fifty years after Kramers. Reviews of Modern Physics, 62, 251.

Harb, M., Jeantelot, G., Basset, J.M. (2019). Insights into the most suitable TiO_2 surfaces for photocatalytic O_2 and H_2 evolution reactions from DFT calculations. The Journal of Physical Chemistry C, 123, 28210-28218.

Hisatomi, T., Domen, K. (2019). Reaction systems for solar hydrogen production via water splitting with particulate semiconductor. Nature Catalysis, 2, 387-399.

Huang, C., Yao, W., T-Raissi, A., et al. (2011). Development of efficient photoreactors for solar hydrogen production. Solar Energy, 85(1), 19-27.

House, J.E. Principles of chemical kinetics. second ed. USA: Kindle Edition, Academic Press; 2007.

Huber, K.P., Herzberg, G. Constants of diatomic molecules. In: Molecular Spectra and Molecular Structure. Springer, Boston, 1979.

Hwang, I., Mazare, A., Will, J., et al. (2022). Inhibition of H_2 and O_2 recombination: the key to a most efficient single-atom co-catalyst for photocatalytic H_2 evolution from plain water. Advanced Functional Materials, 32, 2207849.

Ichikawa, S. (1997). Photoelectrocatalytic production of hydrogen from natural seawater under sunlight. International Journal of Hydrogen Energy, 22, 675-678.

Ismael, M. (2020). A review and recent advances in solar-to-hydrogen energy conversion based on photocatalytic water splitting over doped-TiO_2 nanoparticles. Solar Energy, 211, 522-546.

Jacquemin, D., Mennucci, B., Adamo, C. (2011). Excited-state calculations with TD-DFT: from benchmarks to simulations in complex environments. Physical Chemistry Chemical Physics, 13, 16987-16998.

Jamali, A., Vanraes, R., Hanselaer, P., et al. (2013). A batch LED reactor for the photocatalytic degradation of phenol. Chemical Engineering and Processing: Process Intensification, 71, 43-50.

Jia, J., Seitz, L.C., Benck, J.D., et al. (2016). Solar water splitting by photovoltaic-electrolysis with a solar-to-hydrogen efficiency over 30%. Nature Communications, 7, 13237.

Jiang, Y.N., Zhang, M., Zhang, X., et al. (2022). Reaction pathway of photocatalytic water splitting on two-dimensional TiO_2 nanosheets. The Journal of Physical Chemistry C, 126, 3915-3922.

Jiang, Z., Zhang, Z.Y., Shangguan, W., et al. (2016). Photodeposition as a facile route to tunable Pt photocatalysts for hydrogen production: on the role of methanol. Catalysis Science & Technology, 6, 81-88.

Jieyang, J., Linsey, C.S., Jesse, D.B., et al. (2016). Solar water splitting by photovoltaic-electrolysis with a solar-to-hydrogen efficiency over 30%. Nature Communications, 7, 13237.

Jing, D., Guo, L., Zhao, L., et al. (2010). Efficient solar hydrogen production by photocatalytic water splitting: from fundamental study to pilot demonstration. International Journal of Hydrogen Energy, 35(13), 7087-7097.

Jinmeng, C., Moqing, W., Yating, W., et al. (2017). Synergetic enhancement of light harvesting and charge separation over surface-disorder-engineered TiO_2 photonic crystals. Chem, 2(6), 877-892.

Ji, S.M., Jun, H., Jang, J.S., et al. (2007). Photocatalytic hydrogen production from natural seawater. Journal of Photochemistry and Photobiology A: Chemistry, 189, 141-144.

Kalman, V., Voigt, J., Jordan, C., et al. (2022). Hydrogen purification by pressure swing adsorption: high-pressure PSA performance in recovery from seasonal storage. Sustainability, 14(21), 14037.

Kazuhiro, S. (2018). Production of high-value-added chemicals on oxide semiconductor photoanodes under visible light for solar chemical-conversion processes. ACS Energy Letters, 3(5), 1093-1101.

Khrootkaew, T., Wangngae, S., Chansaenpak, K., et al. (2023). Heavy atom effect on the intersystem crossing of a boron difluoride formazanate complex-based photosensitizer: experimental and theoretical studies. Chemistry - An Asian Journal, 19(1), e202300808.

Kikuchi, E., Saito, N., Yamaguchi, Y., et al. (2025). Temperature dependence of photocatalytic water splitting under visible light irradiation over Ir- and Sb-codoped $SrTiO_3$:Al. The Journal of Physical Chemistry C, 129, 2381-2390.

Kim, C., Cho, S.H., Cho, S.M., et al. (2022). Review of hydrogen infrastructure: the current status and roll-out strategy. International Journal of Hydrogen Energy, 48, 1701-16.

Kim, J.H., Hansora, D., Sharma, P., et al. (2019). Toward practical solar hydrogen production-an artificial photosynthetic leaf-to-farm challenge. Chemical Society Reviews, 48, 1908-1971.

Kim, M.B., Jee, J.G., Bae, Y.S., et al. (2005). Parametric study of pressure swing adsorption process to purify oxygen using carbon molecular sieve. Industrial & Engineering Chemistry Research, 44(18), 7208-7217.

Kim, Y., Yang, H. (2025). Hydrogen purity: influence of production methods, purification techniques, and analytical approaches. Energies, 18(3), 741.

Król, A., Gajec, M., Holewa-Rataj, J., et al. (2024). Hydrogen purification technologies in the context of its utilization. Energies, 17(15), 3794.

Klamt, A., Jonas, V., Bürger, T., et al. (1998). Refinement and parametrization of COSMO-RS. The Journal of Physical Chemistry A, 102(26), 5074-5085.

Klamt, A., Schüürmann, G. (1993). COSMO: a new approach to dielectric screening in solvents with explicit expressions for the screening energy and its gradient. Journal of the Chemical Society, Perkin Transactions 2, 2, 799-805.

Kowalska, E., Rau, S. (2010). Photoreactors for wastewater treatment: a review. Recent Patent on Engineering, 4(3).

Kubiak, A., Dozzi, M.V., Montalbano, M., et al. (2024). LED-driven photodeposition of Pt nanoparticles on TiO_2: combined effects of titania crystallinity and adopted wavelength on photoactivity. Arabian Journal of Chemistry, 17, 105846.

Kumaravel, V., Abdel, W.A. (2018). A short review on hydrogen, biofuel, and electricity production using seawater as a medium. Energy Fuels, 32, 6423-6437.

Larsen, D. (2022). An evaluation of energy consumption comparing conventional water treatment plants to microfiltration and ultrafiltration water treatment plants. Clemson University.

Liao, C.H., Huang, C.W., Wu, J.C.S. (2012). Hydrogen production from semiconductor-based photocatalysis via water splitting. Catalysts, 2(4), 490-516.

Liao, L., Zhang, Q., Su, Z., et al. (2014). Efficient solar water-splitting using a nanocrystalline CoO photocatalyst. Nature Nanotechnology, 9, 69-73.

Lin, W.C., Yang, W.D., Huang, I.L., et al. (2009). Hydrogen production from methanol/water photocatalytic decomposition using Pt/TiO_2-xN_x catalyst. Energy Fuels, 23(4), 2192-2196.

Li, L.Y., Zhou, Z.M., Li, L.Y., et al. (2019). Thioether-functionalized 2D covalent organic framework featuring specific affinity to Au for photocatalytic hydrogen production from seawater. ACS Sustainable Chemistry & Engineering, 7, 18574-18581.

Li, Y., Yin, Z., Liang, Z., et al. (2019). 2D/2D/2D heterojunction of Ti_3C_2 MXene/MoS_2 nanosheets/TiO_2 nanosheets with exposed (001) facets toward enhanced photocatalytic hydrogen production activity. Applied Catalysis B: Environmental, 246, 12-20.

Liu, E., Lin, X., Hong, Y., et al. (2021). Rational copolymerization strategy engineered C self-doped g-C_3N_4 for efficient and robust solar photocatalytic H_2 evolution. Renewable Energy, 178, 757-765.

Liu, J., Zhang, Y., Lu, L., et al. (2012). Self-regenerated solar-driven photocatalytic water-splitting by urea derived graphitic carbon nitride with platinum nanoparticles. Chemical Communications, 70.

Lively, R.P., Bessho, N., Bhandari, D.A., et al. (2012). Thermally moderated hollow fiber sorbent modules in rapidly cycled pressure swing adsorption mode for hydrogen purification. International Journal of Hydrogen Energy, 37(20), 15227-15240.

Li, W., Duan, W., Liao, G., et al. (2024). 0.68% of solar-to-hydrogen efficiency and super-high photostability: panel H_2O-to-H_2 conversion based on a novel organic-inorganic membrane catalyst. Research Square.

Loh, J.Y.Y., Wang, A., Mohan, A., et al. (2024). Leave no photon behind: artificial intelligence in multiscale physics of photocatalyst and photoreactor design. Advanced Science, 11(18), 2306604.

Makihira, A., Barreto, L., Riahi, K. (2003). Assessment of alternative hydrogen pathways: natural gas and biomass. IIASA Interim Report, IR-03-037, Laxenburg, Austria.

Makula, P., Pacia, M., Macyk, W. (2018). How to correctly determine the band gap energy of modified semiconductor photocatalysts based on UV-Vis spectra. The Journal of Physical Chemistry Letters, 9(23), 6814-6817.

Malik, A.S., Liu, T., Dupuis, M., et al. (2020). Water oxidation on TiO_2: a comparative DFT study of $1e^-$, $2e^-$, and $4e^-$ processes on rutile, anatase, and brookite. The Journal of Physical Chemistry C, 124(15), 8094-8100.

Maurya, J.O. (2022). Life cycle and techno-economic assessments of photocatalytic hydrogen production. University of Alberta.

Mehmeti, A., Angelis-Dimakis, A., Arampatzis, G., et al. (2018). Life cycle assessment and water footprint of hydrogen production methods: from conventional to emerging technologies. Environments, 5, 24.

Melvin, A.A., Illath, K., Das, T., et al. (2015). M-Au/TiO_2 (M = Ag, Pd, and Pt) nanophotocatalyst for overall solar water splitting: role of interfaces. Nanoscale, 7, 13477-13488.

Meng, A., Zhang, L., Cheng, B., et al. (2019). Dual cocatalysts in TiO_2 Photocatalysis. Advanced Materials, 31(30), 1807660.

Mercea, P.V., Hwang, S.T. (1994). Oxygen separation from air by a combined pressure swing adsorption and continuous membrane column process. Journal of Membrane Science, 88(2-3), 131-144.

Michelle, N.Y., Mikaela, J.L., Sudeep, C.P., et al. (2016). Tailoring microbial electrochemical cells for production of hydrogen peroxide at high concentrations and efficiencies. ChemSusChem, 2(23), 3345-3352.

Middlemas, S., Fang, Z.Z., Fan, P. (2015). Life cycle assessment comparison of emerging and traditional titanium dioxide manufacturing processes. Journal of Cleaner Production, 89, 137-147.

Morales, J.Y.R., Ortiz-Torres, G., García, R.O.D., et al. (2022). Review of the pressure swing adsorption process for the production of biofuels and medical oxygen: separation and purification technology. Adsorption Science & Technology, 2022.

Neese, F. (2022). Software update: the ORCA program system-version 5.0. WIREs Computational Molecular Science, 12(5), e1606.

Neese, F. (2012). The ORCA program system. WIREs Computational Molecular Science, 2(1), 73-78.

Nickels, P., Zhou, H., Basahel, S.N., et al. (2012). Laboratory scale water circuit Including a photocatalytic reactor and a portable In-stream sensor to monitor pollutant degradation. Industrial & Engineering Chemistry Research, 51(8), 3301-3308.

Nishiyama, H., Yamada, T., Nakabayashi, M., et al. (2021). Photocatalytic solar hydrogen production from water on a 100-m^2 scale. Nature, 598, 304-307.

Nováková, L., Novotná, L., Prochazková, M. (2022). Predicted future development of imperfect complementary goods-copper and zinc until 2030. Acta Montanistica Slovaca, 27(1), 135-51.

Pala, L.P.R., Peela, N.R. (2021). Green hydrogen production in an optofluidic planar microreactor via photocatalytic water splitting under visible/simulated sunlight irradiation. Energy Fuels, 35, 19737-19747.

Pandey L.B., Aikens, C.M. (2012). Theoretical investigation of the electrochemical mechanism of water splitting on a titanium oxide cluster model. The Journal of Physical Chemistry A, 116, 526-535.

Panajapo, P., Promma, P., Sagarik, K. (2024). Mechanisms of photoisomerization of the prenylated flavin mononucleotide cofactor: a theoretical study. Royal Society Open Science, 14, 20061-20072.

Panajapo, P., Suwannakham, P., Promma, P., et al. (2024). Mechanisms of glycine formation in cold interstellar media: a theoretical study. Royal Society Open Science, 11, 231957.

Paolo, A.D., Cufalo, G., Addamo, M. et al. (2008). Photocatalytic activity of nanocrystalline TiO_2 (brookite, rutile and brookite-based) powders prepared by thermohydrolysis of $TiCl_4$ in aqueous chloride solutions. Colloids and Surfaces A: Physicochemical and Engineering Aspects, 317(1-3), 366-376.

Patel, M. (2003). Cumulative energy demand (CED) and cumulative CO_2 emissions for products of the organic chemical industry. Energy, 28, 721-740.

Plessow, P. (2013). Reaction path optimization without NEB springs or interpolation algorithms. Journal of Chemical Theory and Computation, 9(3), 1305-1310.

Pollak, E., Talkner, P. (2005). Reaction rate theory: what it was, where is it today, and where is it going?. Chaos, 15, 026116.

Prasad, C., Tang, H., Liu, Q., et al. (2020). A latest overview on photocatalytic application of g-C_3N_4 based nanostructured materials for hydrogen production. International Journal of Hydrogen Energy, 45, 337-379.

Rathod, P.B., Waghuley, S.A. (2015). Synthesis and UV-Vis spectroscopic study of TiO_2 nanoparticles. International Journal of Nanomanufacturing, 11, 185-193.

Rayes-Gasga, J., Koudriavtseva, O., Herrera-Becerra, R., et al. (2015). XRD characterization of crystallinity of human tooth enamel under influence of mechanical grinding. Materials Sciences and Applications, 6, 464-472.

Redington, R.L., Olson, W.B., Cross, P.C. (1962). Studies of hydrogen peroxide: the infrared spectrum and the internal rotation problem. The Journal of Chemical Physics, 36, 1311-1326.

Rowland, Z., Blahova, A, Gao, P. (2021). Silver as a value keeper and wealth distributor during an economic recession. Acta Montanistica Slovaca, 26(4), 796-809.

Shuang, C., Ting, S.C., Ying, R.L., et al. (2020). Photocatalytic pure water splitting with high efficiency and value by Pt/porous brookite TiO_2 nanoflutes. Nano Energy, 67, 104287.

Sim, A., Mauter, A.S. (2021). Cost and energy intensity of U.S. potable water reuse systems. Environmental Science: Water Research & Technology, 7, 748-761.

Sircar, S., Golden, T.C. (2000). Purification of hydrogen by pressure swing adsorption. Separation Science and Technology, 35(5), 667-687.

Sircar, S., Golden, T.C. (2009). Pressure swing adsorption technology for hydrogen production. Hydrogen and Syngas Production and Purification Technologies, John Wiley & Sons, Inc., Hoboken, New Jersey, 414-450.

Siriwibool, S., Kaekratoke, N., Chansaenpak, K., et al. (2020). Near-infrared fluorescent pH responsive probe for targeted photodynamic cancer therapy. Scientific Reports, 10, 1283.

Sukkasem, T., Nuchitprasittichai, A., Junpirom, S., et al. (2022). TiO_2/SiO_2 coated 310S stainless steel for hydrogen peroxide generation via photocatalytic reaction. Current Applied Science and Technology, 22(3), 2586-9396.

Sukkasem, T., Nuchitprasittichai, A., Junpirom, S., et al. (2023). Role of SiO_2 in TiO_2/SiO_2 photocatalyst for hydrogen peroxide gas generation from air humidity via photocatalysis. Journal of Inclusion Phenomena and Macrocyclic Chemistry.

Sun, K., Yang, T., Ma, S., et al. (2022). Hydrogen purification performance of pressure swing adsorption based on Cu-BTC/zeolite 5A layered bed. Journal of Wuhan University of Technology-Mater, Sci. Ed. 37(5), 815-822.

Sundar, K.P., Kanmani, S. (2020). Progression of photocatalytic reactors and it's comparison: a review. Chemical Engineering Research and Design, 154, 135-150.

Suwannakham, P., Panajapo, P., Promma, P., et al. (2024). Photoluminescence mechanisms of BF_2-formazanate dye sensitizers: a theoretical study. RSC Advances, 14, 20081.

Thai National LCI Database, TIIS-MTEC-NSTDA.

Tabrizi, M.K., Famiglietti, J., Bonalumi, D., et al. (2023). The carbon footprint of hydrogen produced with state-of-the-art photovoltaic electricity using life-cycle assessment methodology. Energies, 16, 5190.

Tapavicza, E., Tavernelli, I., Rothlisberger, U., et al. (2008). Mixed time-dependent density-functional theory/classical trajectory surface hopping study of oxirane photochemistry. The Journal of chemical Physics, 129, 124108.

Thibault, L.H., Gahlot, P., Debarre, R. (2020). Hydrogen applications and business models - Going blue and green?. Kearney, Energy Transition Institute.

TURBOMOLE V7.8 2023. A development of university of karlsruhe and forschungszentrum karlsruhe GmbH, 1989-2007, TURBOMOLE GmbH, since 2007. http://www.turbomole.org.

U.S. Department of Energy. (2021). U.S. Department of energy clean hydrogen production standard (CHPS) guidance.

Vochozka, M., Kalinova, E., Gao, P., et al. (2021). Development of copper price from July 1959 and predicted development till the end of year 2022. Acta Montanistica Slovaca, 26(2), 262-280.

Wang, Y.L., Wu, G.S. (2008). Improving the TDDFT calculation of low-lying excited states for polycyclic aromatic hydrocarbons using the Tamm-Dancoff approximation. International Journal of Quantum Chemistry, 108(3), 430-439.

Wang, T.H., Fang, Z., Gist, N.W., et al. (2011). Computational study of the hydrolysis reactions of the ground and first excited triplet states of small TiO_2 nanoclusters. The Journal of Physical Chemistry, 115, 9344-9360.

Wang, Z., Wu, W., Xu, Q., et al. (2017). Type-II hetero-junction dual shell hollow spheres loaded with spatially separated cocatalyst for enhancing visible light hydrogen evolution. Nano Energy, 38, 518-525.

Wenderich, K., Mul, G. (2016). Methods, mechanism, and applications of photodeposition in photocatalysis: a review. Chemical Reviews, 116, 14587-14619.

Wigner, E. (1932). Crossing of potential thresholds in chemical reactions. The Journal of Physical Chemistry B, 19B, 203-216.

Wigner, E. (1938). The transition state method. Transactions of the Faraday Society, 34, 29-41.

World Resources Institute & World Business Council for Sustainable Development. (2004). The greenhouse gas protocol: a corporate accounting and reporting standard. Washington, DC: World Resources Institute.

Xianjie, C., Run, S., Qian, C., et al. (2019). Three-dimensional porous g-C_3N_4 for highly efficient photocatalytic overall water splitting. Nano Energy, 59, 644-650.

Xing, Z., Zong, X., Pan, J., et al. (2013). On the engineering part of solar hydrogen production from water splitting: photoreactor design. Chemical Engineering Journal, 104, 125-146.

Xue, F., Si, Y., Wang, M., et al. (2019). Toward efficient photocatalytic pure water splitting for simultaneous H_2 and H_2O_2 production. Nano Energy, 62, 823-831.

Yáñez, M., Relvas, F., Ortiz, A., Gorri, D., et al. (2020). PSA purification of waste hydrogen from ammonia plants to fuel cell grade. Separation and Purification Technology, 240, 116334.

Yoshida, T., Minoura, Y., Nakano, Y., et al. (2016). XAFS study on a photodeposition process of Pt nanoparticles on TiO_2 photocatalyst. Journal of Physics: Conference Series, 712, 012076.

Yu, J., Qi, L., Joroniec, M. (2010). Hydrogen production by photocatalytic water splitting over Pt/TiO_2 nanosheets with exposed (001) facets. The Journal of Physical Chemistry C, 114(30), 13118-13125.

Zhang, Z., Dong, B., Zhang, M., et al. (2014). Electrospun Pt/TiO_2 hybrid nanofibers for visible-light-driven H_2 evolution. International Journal of Hydrogen Energy, 39(34), 19434-19443.

Zheng, W., Weiwei, W., Qi, X., et al. (2017). Type-II hetero-junction dual shell hollow spheres loaded with spatially separated cocatalyst for enhancing visible light hydrogen evolution. Nano Energy, 38, 518-525.

Zhou, P., Navid, I.A., Ma, Y., et al. (2023). Solar-to-hydrogen efficiency of more than 9% in photocatalytic water splitting. Nature, 613, 66-70.

APPENDIX A

EXPLORING PHOTOCATALYTIC WATER SPLITTING PATHWAYS FOR EFFICIENT HYDROGEN PRODUCTION: A THEORETICAL INVESTIGATION

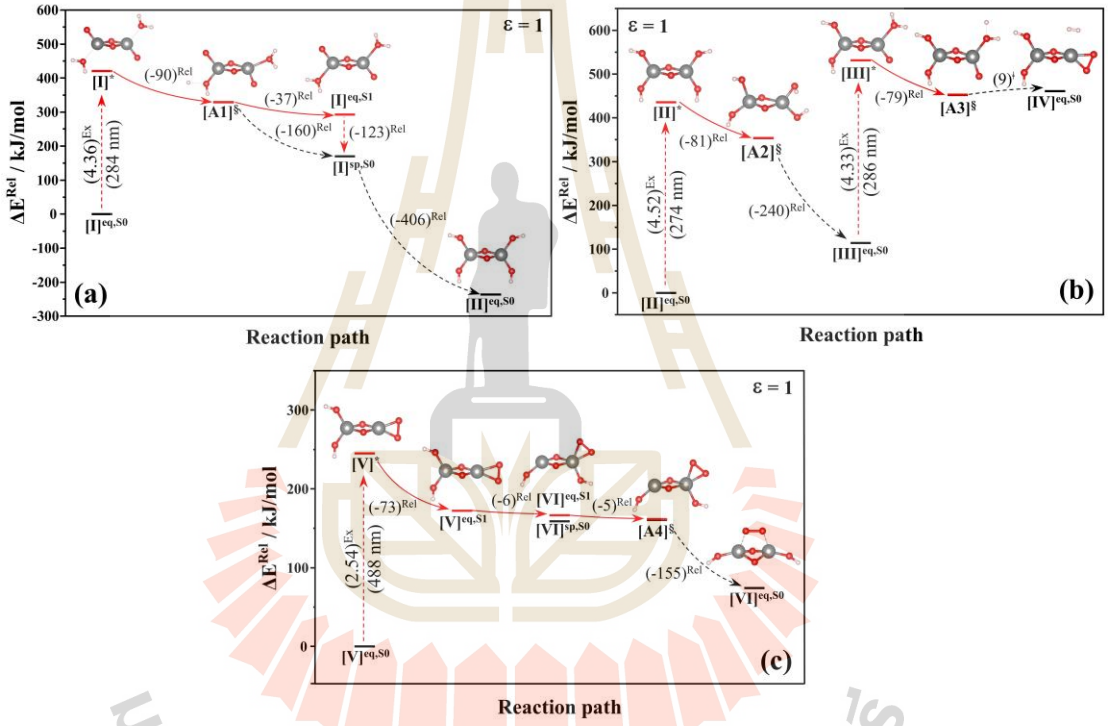

Figure A1 Consecutive elementary reactions involving multiple $S_0 \rightarrow S_1$ photoexcitations, $S_1 \rightarrow S_0$ internal conversion at the S_0/S_1 intersection and relaxation in the S_0 state (ε = 1). (a) Photodissociation of the adsorbed $(H_2O)_2$ on $(TiO_2)_2$. (b) Dehydrogenation **(I)**. (c) Deoxygenation. The symbols are explained in the text. $(...)^{Ex}$ = vertical excitation energy in eV; $(...)^{Rel}$ = relaxation energy in kJ/mol; $(...)^{‡}$ = energy barrier in kJ/mol.

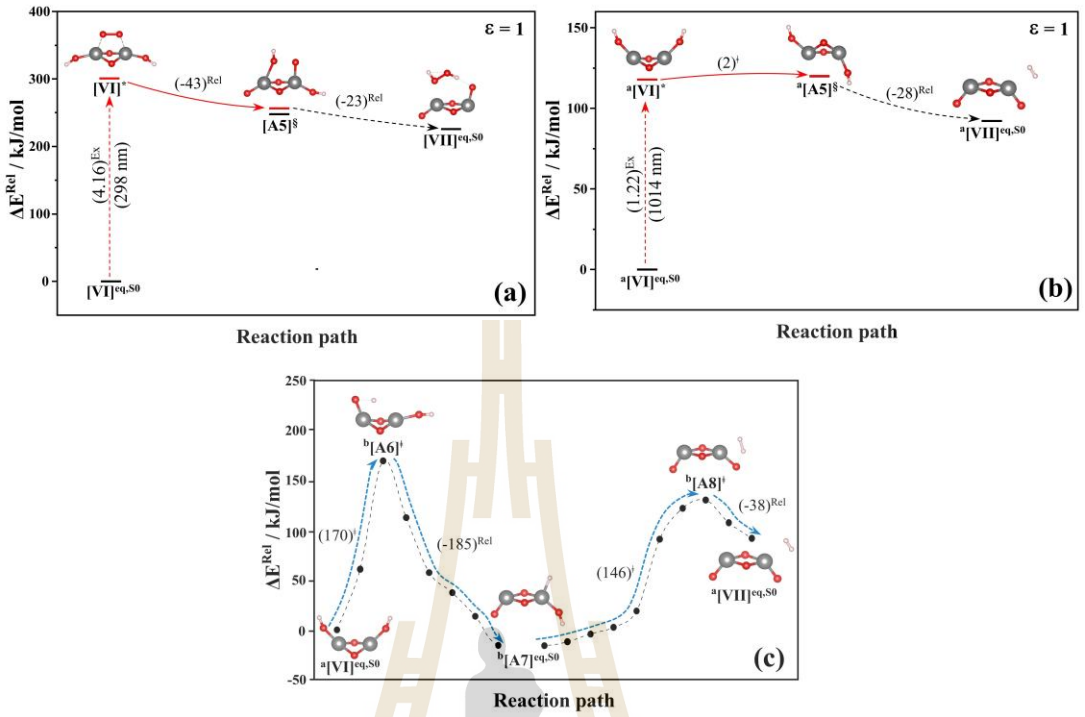

Figure A2 Parallel elementary reactions to regenerate the $(TiO_2)_2$ photocatalyst and H_2O_2, O_2 and H_2 productions (**ε** = 1). a) H_2O_2 formation from the photoexcitation of the O_2 absorbed on $(TiO_2)_2$. b) Dehydrogenation (**IIa**) in the S_1 state, proceeding after the O_2 molecule removed from the surface. c) Dehydrogenation (**IIb**) in the S_0 state, proceeding after the O_2 molecule removed from the surface.

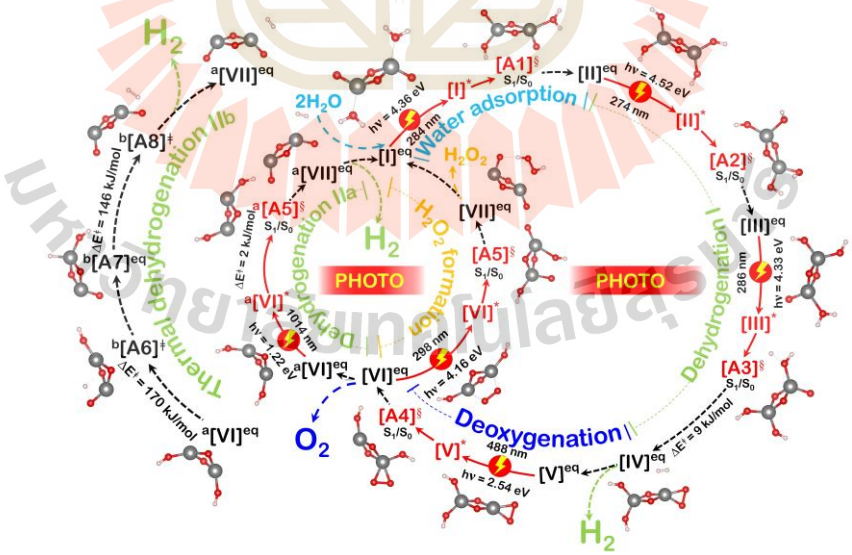

Figure A3 Holistic elementary reaction networks for the photocatalytic water splitting and H_2, O_2 and H_2O_2 productions using $(TiO_2)_2$ photocatalyst in **ε** = 1, obtained from the analysis of the potential energy profiles in Figs. S1 and S2. The symbols are explained in the text.

Table A1 Equilibrium structures of the $(TiO_2)_2(H_2O)_2$ precursor and characteristic structures of the chemical species on the S_0 and S_1 PESs, obtained from the DFT, TD-DFT/B3LYP/TZVP and NEB methods in aqueous solution (ε = 1). The symbols used are explained in the text. E^{Tot} = total energy in au; ΔE^{Ex} = $S_0 \rightarrow S_1$ vertical excitation energy in eV; (...) = excitation wavelength in nm; $\Delta E^{\S}$ = energy difference at the S_0/S_1 intersection (§) in kJ/mol.

Labels	Structures	E^{Tot}	ΔE^{Ex}	ΔE^{VdW} [$\Delta E^{H\text{-}bond}$]	Labels	Structures	E^{Tot}	$\Delta E^{\S}$
$[I]^{eq,S0}$	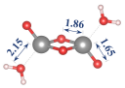	-2152.8703	4.36 (284)	-252.80	$[I]^{eq,S1}$	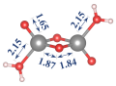	-2152.7099	–
$[II]^{eq,S0}$	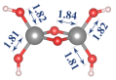	-2152.9604	4.52 (274)	–	$[V]^{eq,S1}$	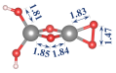	-2151.5118	–
$[III]^{eq,S0}$	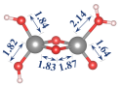	-2152.9169	4.33 (286)	–	$[VI]^{eq,S1}$	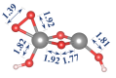	-2151.5417	–
$[IV]^{eq,S0}$	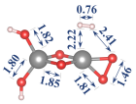	-2152.7846	–	-16.50	$[A1]^{\S}$	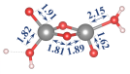	-2152.6888	0.97
$[V]^{eq,S0}$	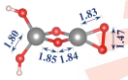	-2151.6052	2.54 (488)	–	$[A2]^{\S}$	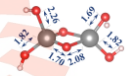	-2152.7355	0.36
$[VI]^{eq,S0}$	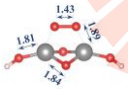	-2151.6030	3.11 (398)	-546.80	$[A3]^{\S}$	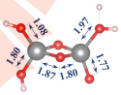	-2152.7878	0.26
$[VII]^{eq,S0}$	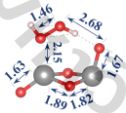	-2151.5174	–	[-124.85]	$[A4]^{\S}$	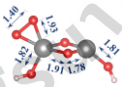	-2151.5437	0.88
$^{a}[VI]^{eq,S0}$	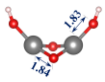	-2001.1348	1.22 (1014)	–	$[A5]^{\S}$	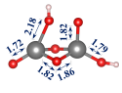	-2151.5049	9.40
$^{a}[VII]^{eq,S0}$	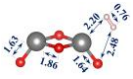	-2001.0998	–	-30.27	$^{a}[A5]^{\S}$		-2001.0890	0.09

Table A2 Thermodynamic properties of the exothermic and endothermic elementary reactions in ε = 1. (a) The O_2 production [deoxygenation in [Eq. (4.4)]. (b)-(c) Formation of the ^{b}**[A7]**^{eq,S0} intermediate and second H_2 production and $(TiO_2)_2$ regeneration [dehydrogenation **(IIb)** in Eq. (4.7)]. (d) Formation of ^{b}**[A6]**‡ and ^{a}**[VII]**^{eq,S0} from **[V]*** in Model **(b)** in Fig. 4.8(b).

(a)

T	$^{a}[VI]^{eq,S0} \longrightarrow {}^{b}[A6]^{‡}$			$^{b}[A6]^{‡} \longrightarrow {}^{b}[A7]^{eq,S0}$			$^{a}[VI]^{eq,S0} \longrightarrow {}^{b}[A7]^{eq,S0}$		
	$\Delta H^{o,‡}$	$\Delta S^{o,‡}$	$\Delta G^{o,‡}$	ΔH^{o}	ΔS^{o}	ΔG^{o}	$\Delta H^{o,Tot}$	$\Delta S^{o,Tot}$	$\Delta G^{o,Tot}$
280	153.5	-6.4	160.0	-169.0	8.8	-177.8	-15.5	2.3	-17.8
296	153.2	-7.1	160.3	-168.5	9.7	-178.2	-15.3	2.6	-17.9
333	152.5	-8.8	161.2	-167.3	12.2	-179.4	-14.8	3.4	-18.2
380	151.5	-11.0	162.5	-165.7	15.4	-181.2	-14.2	4.5	-18.7
609	147.4	-22.6	170.0	-157.3	34.6	-191.9	-9.9	12.0	-21.9
900	143.2	-38.3	181.5	-146.0	64.0	-210.0	-2.8	25.7	-28.5
1066	141.0	-47.6	188.6	-139.4	82.6	-222.0	1.6	35.0	-33.4
1472	135.7	-71.5	207.3	-122.9	132.3	-255.1	12.8	60.7	-47.8
1688	132.9	-84.9	217.8	-114.1	160.5	-274.6	18.8	75.6	-56.8
2382	123.2	-130.7	253.9	-85.5	258.4	-344.0	37.7	127.8	-90.0

(b)

T	$^{b}[A7]^{eq,S0} \longrightarrow {}^{b}[A8]^{‡}$			$^{b}[A8]^{‡} \longrightarrow {}^{a}[VII]^{eq,S0}$			$^{b}[A7]^{eq,S0} \longrightarrow {}^{a}[VII]^{eq,S0}$		
	$\Delta H^{o,‡}$	$\Delta S^{o,‡}$	$\Delta G^{o,‡}$	ΔH^{o}	ΔS^{o}	ΔG^{o}	$\Delta H^{o,Tot}$	$\Delta S^{o,Tot}$	$\Delta G^{o,Tot}$
280	131.7	-5.1	136.8	-33.7	3.7	-37.5	98.0	-1.3	99.3
296	131.3	-5.8	137.1	-33.5	4.3	-37.7	97.8	-1.5	99.4
333	130.3	-7.7	138.0	-32.8	5.5	-38.3	97.4	-2.2	99.7
380	129.0	-10.3	139.3	-32.0	7.2	-39.2	96.9	-3.1	100.1
609	122.6	-25.1	147.8	-28.3	16.5	-44.8	94.3	-8.7	103.0
900	115.3	-46.9	162.2	-24.8	29.0	-53.8	90.5	-17.9	108.4
1066	111.4	-60.2	171.6	-23.3	36.1	-59.4	88.1	-24.1	112.1
1472	102.2	-94.9	197.1	-20.3	53.9	-74.2	82.0	-41.0	122.9
1688	97.4	-114.5	211.9	-18.8	63.6	-82.4	78.6	-50.9	129.5
2382	81.5	-182.2	263.7	-14.1	96.1	-110.2	67.4	-86.1	153.5

Table A2 Thermodynamic properties of the exothermic and endothermic elementary reactions in ε = 1. (a) The O_2 production [deoxygenation in [Eq. (4.4)]. (b)-(c) Formation of the ^{b}**[A7]**^{eq,S0} intermediate and second H_2 production and $(TiO_2)_2$ regeneration [dehydrogenation **(IIb)** in Eq. (4.7)]. (d) Formation of ^{b}**[A6]**‡ and ^{a}**[VII]**^{eq,S0} from **[V]*** in Model **(b)** in Fig. 4.8(b) (continue).

(c)

T	[V]* ⟶ [A4]§			[A4]§ ⟶ [VI]eq,S0			[V]* ⟶ [VI]eq,S0		
	ΔH°	ΔS°	ΔG°	ΔH°	ΔS°	ΔG°	ΔH°,Tot	ΔS°,Tot	ΔG°,Tot
280	-83.6	-0.6	-82.9	-153.3	3.8	-157.1	-236.8	3.2	-240.0
296	-83.6	-0.6	-82.9	-153.2	4.1	-157.2	-236.7	3.5	-240.2
333	-83.5	-0.7	-82.9	-152.9	4.8	-157.7	-236.4	4.1	-240.5
380	-83.5	-0.7	-82.8	-152.5	5.7	-158.2	-236.0	5.0	-241.0
609	-83.6	-1.0	-82.5	-150.5	10.8	-161.3	-234.1	9.8	-243.9
900	-83.6	-1.3	-82.3	-148.0	17.9	-166.0	-231.6	16.6	-248.2
1066	-83.6	-1.5	-82.2	-146.6	22.3	-168.8	-230.2	20.8	-251.0
1472	-83.7	-1.8	-81.9	-143.1	33.4	-176.5	-226.9	31.5	-258.4
1688	-83.8	-2.0	-81.8	-141.3	39.5	-180.9	-225.1	37.6	-262.6
2382	-83.9	-2.4	-81.5	-135.5	60.3	-195.8	-219.3	57.9	-277.2

(d)

T	[V]* ⟶ b[A6]‡			[V]* ⟶ a[VII]eq,S0		
	ΔH°,‡	ΔS°,‡	ΔG°,‡	ΔH°,Tot	ΔS°,Tot	ΔG°,Tot
280	-83.3	-3.2	-80.0	-154.3	4.2	-158.5
296	-83.5	-3.6	-79.9	-154.2	4.6	-158.7
333	-83.9	-4.7	-79.3	-153.8	5.3	-159
380	-84.5	-6.0	-78.5	-153.3	6.4	-159.6
609	-86.7	-12.8	-73.9	-149.7	13.1	-162.8
900	-88.4	-21.7	-66.7	-143.9	24.4	-168.3
1066	-89.2	-26.8	-62.4	-140.5	31.7	-172.3
1472	-91.2	-40.0	-51.1	-132.1	51.2	-183.3
1688	-92.2	-47.3	-44.8	-127.7	62.3	-189.9
2382	-96.1	-72.8	-23.3	-114.2	99.6	-213.7

Table A3 Kinetics and thermodynamic properties of the rate-determining elementary reactions in the S_0 state (ε = 1). Rate constants, temperatures and energies are in s^{-1}, K and kJ/mol, respectively. The symbols used are explained in the text.

Reaction path	$\Delta E^{\ddagger}$	$\Delta E^{\ddagger,ZPC}$	T_c	T	$k_f^{Q\text{-}vib}$	$k_f^{S\text{-}Wig}$	$\Delta G_f^{\ddagger}$
				280	1.01×10^{-17}	3.45×10^{-17}	159.5
				296	3.76×10^{-16}	1.18×10^{-15}	159.7
				313	1.39×10^{-14}	4.05×10^{-14}	159.8
				333	5.12×10^{-13}	1.38×10^{-12}	160.0
				355	1.88×10^{-11}	4.69×10^{-11}	160.2
				380	6.90×10^{-10}	1.59×10^{-9}	160.5
				400	8.58×10^{-9}	1.87×10^{-8}	160.7
				438	5.18×10^{-7}	1.03×10^{-6}	161.2
				483	3.12×10^{-5}	5.63×10^{-5}	161.8
				538	1.87×10^{-3}	3.08×10^{-3}	162.7
				609	1.12×10^{-1}	1.69×10^{-1}	163.8
$^{a}[VI]^{eq,S0} \xrightarrow{k_r} {}^{b}[A6]^{\ddagger}$	170	160	338	700	6.68×10^{0}	9.25×10^{0}	165.4
				900	2.88×10^{3}	3.55×10^{3}	169.1
				986	1.85×10^{4}	2.21×10^{4}	170.8
				1091	1.20×10^{5}	1.38×10^{5}	172.9
				1220	7.75×10^{5}	8.72×10^{5}	175.6
				1385	5.05×10^{6}	5.55×10^{6}	179.1
				1600	3.32×10^{7}	3.56×10^{7}	183.9
				1888	2.16×10^{8}	2.26×10^{8}	190.4
				1895	2.20×10^{8}	2.31×10^{8}	190.6
				2323	1.47×10^{9}	1.53×10^{9}	200.8
				3000	1.00×10^{10}	1.02×10^{10}	218.0

$\Delta E^{\ddagger}$ = energy barrier in kJ/mol; $\Delta E^{\ddagger,ZPC}$ = energy barrier with the zero-point vibrational energy correction; T_c = crossover temperature; T = temperature; $k_f^{Q\text{-}vib}$ = rate constant obtained with quantized vibration correction; $k_f^{S\text{-}Wig}$ = $k_f^{Q\text{-}vib}$ with the second-order Wigner correction; $\Delta G_f^{\ddagger}$ = activation Gibbs free energy; f = forward direction.

Table A3 Kinetics and thermodynamic properties of the rate-determining elementary reactions in the S_0 state (ε = 1). Rate constants, temperatures and energies are in s^{-1}, K and kJ/mol, respectively. The symbols used are explained in the text (continue).

Reaction path	$\Delta E^{\ddagger}$	$\Delta E^{\ddagger,ZPC}$	T_c	T	$k_f^{Q\text{-}vib}$	$k_f^{S\text{-}Wig}$	$\Delta G_f^{\ddagger}$
$^b[A7]^{eq,S0} \xrightarrow{k_r} {}^b[A8]^{\ddagger}$	146	140	281	280	2.53×10^{-14}	6.71×10^{-14}	141.3
				296	6.07×10^{-13}	1.51×10^{-12}	141.5
				313	1.45×10^{-11}	3.37×10^{-11}	141.7
				333	3.46×10^{-10}	7.51×10^{-10}	142.0
				355	8.23×10^{-9}	1.67×10^{-8}	142.3
				380	1.95×10^{-7}	3.70×10^{-7}	142.7
				400	1.78×10^{-6}	3.23×10^{-6}	143.0
				438	6.54×10^{-5}	1.10×10^{-4}	143.6
				483	2.38×10^{-3}	3.70×10^{-3}	144.4
				538	8.61×10^{-2}	1.24×10^{-1}	145.5
				609	3.09×10^{0}	4.17×10^{0}	147.0
				700	1.10×10^{2}	1.40×10^{2}	149.0
				900	2.19×10^{4}	2.54×10^{4}	153.9
				986	1.11×10^{5}	1.25×10^{5}	156.1
				1091	5.60×10^{5}	6.21×10^{5}	158.9
				1220	2.84×10^{6}	3.08×10^{6}	162.4
				1385	1.44×10^{7}	1.54×10^{7}	167.0
				1600	7.38×10^{7}	7.75×10^{7}	173.2
				1888	3.73×10^{8}	3.86×10^{8}	181.8
				1895	3.80×10^{8}	3.93×10^{8}	182.0
				2323	1.97×10^{9}	2.02×10^{9}	195.2
				3000	1.03×10^{10}	1.05×10^{10}	217.2

$\Delta E^{\ddagger}$ = energy barrier in kJ/mol; $\Delta E^{\ddagger,ZPC}$ = energy barrier with the zero-point vibrational energy correction; T_c = crossover temperature; T = temperature; $k_f^{Q\text{-}vib}$ = rate constant obtained with quantized vibration correction; $k_f^{S\text{-}Wig}$ = $k_f^{Q\text{-}vib}$ with the second-order Wigner correction; $\Delta G_f^{\ddagger}$ = activation Gibbs free energy; f = forward direction.

APPENDIX B

TECHNO-ECONOMIC AND ENVIRONMENTAL ASSESSMENT OF PILOT-SCALE PHOTOCATALYTIC WATER SPLITTING

Table B1 The H_2 evolution rate from experimental data (one-panel = 0.0308 m^2).

MeOH conc. (%)	H_2 evolution rate (μmol g^{-1} min^{-1})			
	UVA-LED TiO_2	UVA-LED 2%Pt/TiO_2	LED 2%Pt/TiO_2	Natural sunlight 2%Pt/TiO_2
0	0.51	-	-	-
2	5.89	21.32	33.75	76.12
4	11.48	36.14	114.44	98.89
5	30.39[cal]	47.91	165.85[cal]	125.10[cal]
6	43.82	139.08	235.52	124.77
8	144.88	216.40	343.87	260.71
10	248.37[cal]	358.25[cal]	486.94	333.82[cal]

[cal] This H_2 evolution rate was calculated from the fitted graph based on all experimental trends.

Table B2 Experimental H_2 evolution rate (g/day).

MeOH conc. (%)	H_2 evolution rate (g day^{-1})							
	UVA-LED TiO_2		UVA-LED 2%Pt/TiO_2		LED 2%Pt/TiO_2		Natural sunlight 2%Pt/TiO_2	
Panel	1	3247	1	3247	1	3247	1	3247
0	0.0012	3.82	-	-	-	-	-	-
2	0.0136	44.06	0.0491	159.50	0.0778	252.49	0.0512	166.09
4	0.0265	85.88	0.0833	270.37	0.2637	856.14	0.0665	215.78
5	0.0700	227.32	0.1104	358.42	0.3821	1,240.70	0.0841	272.97
6	0.1010	327.82	0.3204	1,040.47	0.5426	1,761.95	0.0838	272.25
8	0.3338	1,083.86	0.4986	1,618.91	0.7923	2,572.52	0.1752	568.87
10	0.5722	1,858.08	0.8254	2,680.12	1.1219	3,642.84	0.2243	728.40
Area* (m^2)	0.0308	100	0.0308	100	0.0308	100	0.0308	100

* The area of one panel is 0.0308 m^2, and an estimated 3,247-panel photoreactor is required to achieve 100 m^2.

Table B3 The H_2 evolution rate for a 100 m^2 panel-photoreactor.

MeOH conc. (%)	H_2 evolution rate							
	UVA-LED		UVA-LED		LED		Natural sunlight	
	TiO_2		2%Pt/TiO_2		2%Pt/TiO_2		2%Pt/TiO_2	
	kg/day	kg/yr	kg/day	kg/yr	kg/day	kg/yr	kg/day	kg/yr
0	0.004	1.14	-	-	-	-	-	-
2	0.044	13.22	0.159	47.85	0.252	75.75	0.166	29.90
4	0.086	25.76	0.270	81.11	0.856	256.84	0.216	38.84
5	0.227	68.20	0.358	107.53	1.241	372.21	0.273	49.13
6	0.328	98.35	1.040	312.14	1.762	528.58	0.272	49.00
8	1.084	325.16	1.619	485.67	2.573	771.76	0.569	102.40
10	1.858	557.42	2.680	804.04	3.643	1,092.85	0.728	131.11

The estimated CO_2 emissions from the photocatalytic water splitting reaction using MeOH as a sacrificial reagent were calculated for different concentrations (2-10% v/v). The reaction equation is as follows eq. (B1):

$$CH_3OH + H_2O \longrightarrow CO_2 + 3H_2 \quad \text{(B1)}$$

Although the H_2 evolution rate increases with MeOH concentration, the reaction stoichiometry remains unchanged. **Assuming no side reactions**, the GHG emissions were estimated based on the amount of H_2 produced, with the corresponding CO_2 calculated by back-referencing the reaction stoichiometry. Consequently, the GHG emissions are theoretically identical under all MeOH concentrations. For example, at 2%v/v MeOH with a TiO_2 photocatalyst under a UVA-LED light source, the annual H_2 production is 13.22 kg.

$$n_{H_2} = \frac{13.22\ \text{kg/yr}}{2.016\ \text{kg/kmol}} = 6.5575\ \text{kmol/yr}$$

$$n_{CO_2} = \frac{n_{H_2}}{3} = \frac{6.5575\ \text{kmol/yr}}{3} = 2.1858\ \text{kmol/yr}$$

$$m_{CO_2} = 2.1858\ \text{kmol/yr} \times \frac{44.01\ \text{kg}}{\text{kmol}} = 96.1985\ \text{kg/yr}$$

$$\text{GHG emission} = \frac{96.1985\ \text{kg}\ CO_2\text{/yr}}{13.22\ \text{kg}\ H_2\text{/yr}} = 7.28\ \text{kg}\ CO_2\ /\ \text{kg}\ H_2$$

Thus, the GHG emission from the photocatalytic water splitting reaction is 7.28 kg CO_2/kg H_2. The variations in CO_2 emissions under different reaction conditions are presented in Table B4.

Table B4 The H_2 and CO_2 evolution rate for a 100 m^2 panel-photoreactor.

MeOH conc. (%)	Estimation of product production (kg/yr)							
	UVA-LED		UVA-LED		LED		Natural sunlight	
	TiO_2		2%Pt/TiO_2		2%Pt/TiO_2		2%Pt/TiO_2	
	H_2	CO_2	H_2	CO_2	H_2	CO_2	H_2	CO_2
2	13.22	96.19	47.85	348.19	75.75	551.19	29.90	217.55
4	25.76	187.49	81.11	590.22	256.84	1,868.97	38.84	282.63
5	68.20	496.24	107.53	782.44	372.21	2,708.49	49.13	319.61
6	98.35	715.65	312.14	2,271.38	528.58	3,846.39	49.00	356.59
8	325.16	2,366.11	485.67	3,534.13	771.76	5,615.91	102.40	745.11
10	557.42	4,056.26	804.04	5,850.80	1,092.85	7,952.45	131.11	954.07

Table B5 GHG emissions from light sources.

MeOH conc. (%)	GHG emission (kg CO_{2eq}/kg H_2)							
	UVA-LED		UVA-LED		LED		Natural sunlight	
	TiO_2		2%Pt/TiO_2		2%Pt/TiO_2		2%Pt/TiO_2	
	Non-renewable	Renewable	Non-renewable	Renewable	Non-renewable	Renewable	Non-renewable	Renewable
0	52,461.70	4,371.81	-	-	-	-	-	-
2	4,542.52	378.54	1,254.95	104.58	792.75	66.06	-	-
4	2,330.62	194.22	740.33	61.69	233.79	19.48	-	-
5	880.53	73.38	558.45	46.54	161.33	13.44	-	-
6	610.58	50.88	192.37	16.03	113.60	9.47	-	-
8	184.67	15.39	123.64	10.30	77.81	6.48	-	-
10	107.72	8.98	74.68	6.22	54.95	4.58	-	-

$$\text{Electricity cost (\$)} = \left[\left(\text{Electricity use (kWh)} \times \frac{5\ \text{THB}}{\text{kWh}}\right) + \left(\text{Electricity use (kWh)} \times \frac{5\ \text{THB}}{\text{kWh}} \times \frac{7}{100}\right)\right] \times \frac{1\ \text{USD}}{32.46\ \text{THB}}$$

$$\text{CED (MJ)} = \text{Electricity use (kWh)} \times \frac{3.6\ \text{MJ}}{1\ \text{kWh}}$$

Table B6 The CED associated with the preparation of the photocatalyst material.

Equipment	No.	Power (W)	Operating time	Electricity use (kWh)	Equipment cost ($)	Electricity cost ($)	CED (MJ)
Mixing tank with agitators	1	680	1 min	0.01	1,000	0.002	0.04
Doctor blade coater	1	200	135 min	0.45	1,590	0.07	1.62
	2	200	135 min	0.45	1,590	0.07	1.62
	3	200	135 min	0.45	1,590	0.07	1.62
Ultrasonic cleaner	1	10,800	30 min	5.40	13,600	0.89	19.44
Convection oven - Cleaning surface	1	20,000	3 days	432.00	70,000	71.20	1,555.20
- Drying of TiO_2		20,000	3 days	432.00		71.20	1,555.20
- Drying of 2%Pt/TiO_2		20,000	3 days	432.00		71.20	1,555.20
Furnace	1	39,000	3 hours	35.10	48,000	5.79	126.36
Photodeposition	1	2,500	50 hours	125.00	34,000	20.60	450.00
	2	2,500	50 hours	125.00	34,000	20.60	450.00
			Total (TiO_2)	**905.86**	**137,370.00**	**149.30**	**3,261.10**
			Total (2%Pt/TiO_2)	**1,587.86**	**205,370.00**	**261.71**	**5,716.30**

Table B7 The CED associated with UVA-LED and LED light sources.

Light sources	Power (W)	Pieces	Cost per piece ($)	Cost of light source ($)	Electricity use (kWh)	Electricity cost ($/yr)	CED (MJ/yr)
UVA-LED	50	278	10	2,780.00	100,080.00	**16,495.01**	**360,288.00**
LED	50	278	2.5	685.00	100,080.00	**16,495.01**	**360,288.00**

Table B8 Material cost of TiO_2 and 2% Pt/TiO_2 photocatalyst for the preparation of 3,247 panels.

Materials	1-panel		3247-panels		Cost/unit		Total cost
	Amount	Unit	Amount	Unit	Cost	Unit	($/yr)
TiO_2-anatase	1.00	g	3,247.00	g	1.95	$/kg	6.33
Polyurethane	0.96	g	3,117.12	g	2.55	$/kg	7.95
H_2PtCl_6	0.0536	g	174.04	g	18	$/g	3,132.71
Methanol	7.91	g	25,683.77	g	0.36	$/kg	9.25
Water	90.00	ml	292,230.00	ml	0.46	$/m^3	134.43
Total (TiO_2)							**14.28**
Total (2%Pt/TiO_2)							**3,290.66**

Table B9 Quantity of reactant feed required for H_2 production using 3,247 panels (UVA-LED and LED light sources).

Feed (L/day)	MeOH conc. (%)	Total per year (L)		Reactant cost ($)/yr		**Total cost ($/yr)**
		Water	MeOH	Water	MeOH	
400	0	120,000	-	55.20	-	**55.20**
400	2	117,600	2,400	54.10	683.42	**737.52**
400	4	115,200	4,800	52.99	1,366.85	**1,419.84**
400	5	114,000	6,000	52.44	1,708.56	**1,761.00**
400	6	112,800	7,200	51.89	2,050.27	**2,102.16**
400	8	110,400	9,600	50.78	2,733.70	**2,784.48**
400	10	108,000	12,000	49.68	3,417.12	**3,466.80**

Table B10 Quantity of reactant feed required for H_2 production using 3,247 panels (Natural sunlight).

Feed (L/day)	MeOH conc. (%)	Total per year (L)		Reactant cost ($)/yr		**Total cost ($/yr)**
		Water	MeOH	Water	MeOH	
400	0	72,000	-	33.12	-	**33.12**
400	2	70,560	2,400	32.46	410.05	**442.51**
400	4	69,120	4,800	31.80	820.11	**851.90**
400	5	68,400	6,000	31.46	1,025.14	**1,056.60**
400	6	67,680	7,200	31.13	1,230.16	**1,261.30**
400	8	66,240	9,600	30.47	1,640.22	**1,670.69**
400	10	64,800	12,000	29.81	2,050.27	**2,080.08**

Table B11 Material cost of the panel photoreactor.

Material	Area (m^2)	Total area (m^2) for 3,247 panels	Cost	unit	**Total cost ($)**
Stainless plate (0.2738 kg/panel)	0.0345	112.02	1.18	$/kg	**1,050.83**
Glass sheet (cover plate)	0.0345	112.02	2.60	$/$m^2$	**291.26**
Glass sheet (Used as a substrate for catalyst coating)	0.0308	100.01	2.60	$/$m^2$	**260.02**

APPENDIX C

PUBLICATION

Sukkasem, T., Junpirom, S., Panajapo, P., Sagarik, K. (2025). Exploring photocatalytic water splitting pathways for efficient hydrogen production: A theoretical investigation. International Journal of Hydrogen Energy, 145, 1096-1107.

BIOGRAPHY

Name: Tanongsak Sukkasem

Education

2023-2025 Docter of Engineering, Mechanical and Process System Engineering (Chemical Engineering), Suranaree University of Technology, Thailand.
Dissertation: Green hydrogen production by photocatalysis.

2020-2022 Master of Engineering, Mechanical and Process System Engineering (Chemical Engineering), Suranaree University of Technology, Thailand.
Dissertation: Production of hydrogen peroxide gas from photocatalysis for surface desinfection.

2015-2020 Bachelor of Engineering, Chemical Engineering, Suranaree University of Technology, Thailand.

Scholarship

2020-2025 OROG scholarship, Suranaree University of Technology, Thailand.

Publications

Sukkasem, T., et al., Converting polystyrene waste into valuable oils: High performance of SUZ-4 zeolite for selective oil component conversion in catalytic pyrolysis. Fuel 405 (2025) 136456. (Q1/Tier 1; IF = 7.5)

Sukkasem, T., et al., Exploring photocatalytic water splitting pathways for efficient hydrogen production: A theoretical investigation. Inter. J. Hydrogen Energy 145 (2025) 1096-1107. (Q1/Tier 1; IF = 8.3)

Sukkasem, T., et al., Performance of catalytic dehydration of ethanol to ethylene using SUZ-4 zeolite synthesized from rice husk ash in a packed-bed reactor. Micro. Meso. Mater. 384 (2025) 11346. (Q1/Tier 1; IF = 4.8)

Sukkasem, T., et al., Role of SiO_2 in TiO_2/SiO_2 photocatalyst for hydrogen peroxide gas generation from air humidity via photocatalysis. J. Incl. Phenom. Macrocycl. Chem. 104 (2024) 289-305. (Q3; IF = 1.7)

Sukkasem, T., et al., TiO_2/SiO_2 coated 310S stainless steel for hydrogen peroxide generation via photocatalytic reaction. Curr. Appl. Sci. Tech. 22 (2022). (Q4; IF = 0.72)